CENTRO DE INVESTIGACIÓN Y DE ESTUDIOS AVANZADOS
DEL INSTITUTO POLITÉCNICO NACIONAL

UNIDAD ZACATENCO
DEPARTAMENTO DE FÍSICA

"Teorías efectivas para describir interacciones materia oscura-modelo estándar y procesos con violación de sabor leptónico en el sector cargado"

Tesis que presenta

Fabiola Elena Fortuna Montecillo

para obtener el Grado de

Doctora en Ciencias

en la Especialidad de

Física

Director de tesis: Dr. Pablo Roig Garcés

Ciudad de México Mayo, 2023

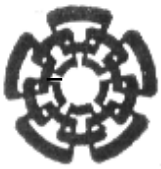

CENTER FOR RESEARCH AND ADVANCED STUDIES OF THE NATIONAL POLYTECHNIC INSTITUTE

PHYSICS DEPARTMENT

"Effective field theories for dark matter-standard model and charged lepton flavor violating interactions"

by

Fabiola Elena Fortuna Montecillo

In order to obtain the

Doctor of Science

degree, speciality in

Physics

Advisor: Ph. D. Pablo Roig Garcés

Mexico City May, 2023

Acknowledgments

A las autoridades y personal del Departamento de Física del Cinvestav, pues en gran parte fue gracias a su trabajo que disfruté mucho mi estadía en las instalaciones, me sentí apoyada y en un ambiente fructífero y adecuado para desempeñar mi trabajo.

A mi asesor, el Dr. Pablo Roig Garcés, le agradezco mucho la oportunidad de desarrollar este trabajo bajo su mentoría. Para mí Pablo es un ejemplo a seguir, como asesor y como investigador. Le agradezco también su disponibilidad para resolver mis dudas y su actitud amable siempre para conmigo.

A mis sinodales, los doctores Eduardo Peinado, Abdel Pérez, Gabriel López, Eduard de la Cruz y Josué de Santiago, les agradezco su tiempo y sus valiosos comentarios sobre mi trabajo.

A mi esposo, Agustín Rodríguez, por ser mi compañero de vida, por su cariño, por lo feliz que soy a su lado.

A mis a papás, Rafael y Elena, que siempre me han apoyado y motivado a lograr lo que me proponga, porque sé que siempre puedo contar con ellos.

A mis hemanos, Dany, Wendy y Jonathan, por tantas experiencias que hemos compartido, por que son personas muy importantes en mi vida.

A mi abuelita, primos, tíos, suegros, cuñados y demás, porque son una gran familia.

A mis amigos Arantza, Alex, Rosy, Marce, Osvaldo, Emily, Lu, Karen y otros más que haya olvidado mencionar, les agradezco mucho su valiosa amistad.

Al Consejo Nacional de Ciencia y Tecnologia (CONACYT) le agradezco el apoyo económico brindado durante estos cuatro años para la obtención del grado de Doctora en Ciencias en la especialidad de Física.

Contents

Resumen

El modelo estándar es una teoría cuántica de campos que ha sido probada con una precisión enorme por múltiples experimentos. Sin embargo, existe evidencia experimental/observacional que nos indica la existencia de física más allá del modelo estándar. En esta tesis nos enfocamos particularmente en dos de estos temas, la materia oscura y la violación de sabor leptónico en el sector cargado. Para ello, utilizamos teorías efectivas, que son herramientas que nos permiten hacer análisis independientes de modelo, para buscar una guía hacia nueva física utilizando los límite experimentales disponibles.

Esta tesis está conformada por cuatro partes, en la primera hicimos fenomenología de materia oscura utilizando una teoría efectiva que describe interacciones entre partículas del modelo estándar y partículas de materia oscura, considerando mediadores de espín 1. La segunda parte del trabajo es un complemento de la primera, donde extendimos el rango de masa para la materia oscura y agregamos nuevos límites experimentales para el análisis. En la tercera parte utilizamos una teoría efectiva que genera la interacción $\ell_i \ell_j \gamma\gamma$ y derivamos límites indirectos para los decaimientos $\ell_i \to \ell_j \gamma\gamma$ a través del cálculo a un lazo de los decaimientos $\ell_i \to \ell_j \gamma$. Nuestros límites indirectos son más restrictivos que los límites experimentales actuales. En la última parte continuamos analizando procesos con violación de sabor leptónico en el sector cargado, particularmente procesos de conversión en núcleos.

Abstract

The standard model is a quantum field theory that has been tested by multiple experiments with enormous precision. However, there is experimental/observational evidence of physics beyond the standard model. In this thesis we focus particularly in two of these issues, dark matter and charged lepton flavor violation. For this, we use effective field theories, which are tools that allow us to look for new physics in a model-independent way using the available experimental limits.

This thesis consists of four parts, in the first one we did a phenomenological analysis of dark matter using an effective field theory that describes interactions between standard model and dark matter particles with spin-1 mediators. The second part is the sequel to the first, where we broaden the allowed mass range for the dark matter and add new experimental limits for the analysis. In the third part, we use an effective field theory that generates the $\ell_i \ell_j \gamma\gamma$ interaction and derived indirect limits for the $\ell_i \to \ell_j \gamma\gamma$ decays by computing the $\ell_i \to \ell_j \gamma$ decays at one loop level. Our indirect limits are more restrictive than current experimental limits. In the last part we continue analyzing charged lepton flavor violating processes, in particular processes of conversion in nuclei.

Chapter 1

Introduction

The Standard Model (SM) is a quantum field theory [1–3] that describes the strong, weak, and electromagnetic interaction, and it has been tested with unprecedented accuracy. Despite its amazing success, the SM is unable to explain several issues so we know it is not a complete theory. Some of these unexplained questions are related with the dark matter content in our universe, the neutrino mass, the matter-antimatter asymmetry, the accelerated expansion of the universe, and the fact that it doesn't include gravity.

We know about the existence of dark matter (DM) from several observations at very different scales in our universe, among others: the rotation curves of galaxies, weak lensing, the cosmic microwave background (CMB). According with the information extracted from the CMB, the matter that we see and describe with the SM accounts for only 5% of the total energy content in the universe. The DM remains a mystery and is one of the topics that we address in this thesis.

On the other hand, in the SM massless neutrinos are assumed and lepton flavor is conserved. However, the discovery of neutrino oscillations implies lepton flavor violation (LFV) in the charged sector, but it is yet to be observed.

Since the rates for those processes cannot be estimated in a model-independent way, they would be related with the nature of physics beyond the standard model and should provide non-trivial information about it. In this thesis we analyze some LFV process.

Many different theories have been proposed to address the different issues beyond the SM and plenty of them predict new particles at scales far beyond any current and planned experiment. A very useful way to look for possible departures from the SM in a model-independent way is provided by the effective field theory (EFT) framework.

One example is the SMEFT [4, 5], the EFT of the SM, where one assume that the SM is correct but also allows for higher-order interactions between the known particles and where the heavy new physics is decoupled [6]. The Wilson coefficients contain all the information about the fundamental theory. Currently constraints on the mass scale of

new particles has been set above a few TeV by direct searches at colliders.

In this thesis we begin by giving an overview of the Standard Model particle content and the interactions between them in chapter 2; in section 2.2, we mention some examples of the amazing agreement between the SM predictions and the experimental measurements of a large number of observables.

Then in chapter 3, we present a brief review of dark matter, going through the first experimental indications of its existence and how the evidence was accumulating and convincing the scientific community. We also mention the main characteristics of a DM particle, then focus on WIMPs as DM candidates and the experimental efforts to detect them.

We continue in chapter 4 with an introduction to the topic of charged Lepton Flavor Violation (cLFV), we explain why would be so interesting to detect such a process and discuss leptonic experimental searches.

In chapter 5, we describe the tool that we use to address the topics introduced in the previous two chapters: the effective field theory. We briefly discuss the advantages of using an EFT to describe any particular phenomenon, as an example we mention the Fermi theory of weak interactions.

We use an the EFT framework to describe interactions between standard model and dark matter particles with spin 1 mediators in chapters 6 and 7. We work in the WIMP paradigm and, to constraint the effective couplings in the Lagrangian, we use several experimental constraints: the relic abundance of DM, the Z invisible decay width, limits from direct and indirect detection and collider constraints.

Then we pursue an EFT approach to study cLFV processes. In chapter 8 we compute indirect upper limits on the $\ell_i \to \ell_j\gamma\gamma$ decays using the more stringent experimental constraints on the $\ell_i \to \ell_j\gamma$ decays. Within our EFT, the decays $\ell_i \to \ell_j\gamma$ are generated at one loop level. Our indirect limits on the process $\ell_i \to \ell_j\gamma\gamma$ will turn out to be more stringent than the current direct bounds. We study the cLFV processes $\ell \to \tau$ and $\mu \to e$ conversion in nuclei in chapter 9. Finally, we give our general conclusions of this thesis in chapter 10.

Chapter 2

Standard Model

The Standard Model [1–3] is a gauge theory, based on the symmetry group $SU(3)_C \otimes SU(2)_L \otimes U(1)_Y$. It describes the strong interaction via the exchange of eight massless gluons, the weak interaction by the exchange of three massive bosons, $W^{\pm}$ and Z^0, and the electromagnetic interaction via the exchange of one massless photon. These mediators are the spin-1 gauge fields. Leptons and quarks constitute the fermionic matter content, and are organized in a structure of three families (prime denotes down-type quarks in the mass basis):

$$\begin{bmatrix} \nu_e & u \\ e^- & d' \end{bmatrix}, \qquad \begin{bmatrix} \nu_\mu & c \\ \mu^- & s' \end{bmatrix}, \qquad \begin{bmatrix} \nu_\tau & t \\ \tau^- & b' \end{bmatrix}, \tag{2.1}$$

where (each quark appears in three different colours)

$$\begin{bmatrix} \nu_\ell & u_i \\ \ell^- & d_i \end{bmatrix} \equiv \begin{pmatrix} \nu_\ell \\ \ell^- \end{pmatrix}_L, \quad \begin{pmatrix} u_i \\ d_i \end{pmatrix}_L, \quad \ell^-_R, \quad u_{iR}, \quad d_{iR}, \tag{2.2}$$

plus the corresponding antiparticles. The right-handed fields are singlets under $SU(2)_L$, while their left-handed partners are $SU(2)_L$ doublets.

The three fermionic families in eq. (2.1) differ in their masses and flavour quantum number while they appear to have identical gauge interactions.

The Spontaneous Symmetry Breaking (SSB) of the electroweak group to the electromagnetic subgroup is triggered when the gauge symmetry is broken by the vacuum:

$$SU(3)_C \otimes SU(2)_L \otimes U(1)_Y \quad \xrightarrow{\text{SSB}} \quad SU(3)_C \otimes U(1)_{\text{QED}}\,. \tag{2.3}$$

The masses of the weak gauge bosons, , $W^{\pm}$ and Z^0, are generated by the SSB mechanism [7, 8], and it also gives rise to the appearance of the so-called Higgs boson, the physical scalar particle in the model. This mechanism also gives masses to the fermions

and generates the mixings between them.

The SM provides a very elegant theoretical framework, which is able to describe, with very high precision —in section 2.2 some examples are given—, the known experimental phenomena in particle physics . In this way the SM constitutes one of the most successful achievements in modern physics.

In the SM the elementary fields are the gauge fields, the fermionic fields and a $SU(2)_L$ doublet Higgs field. In table 2.1 they are listed along with their quantum numbers. G_μ, A_μ and B_μ denote the $SU(3)_C$, $SU(2)_L$ and $U(1)_Y$ gauge fields, respectively. The left-handed and right-handed chirality projections ($P_L \equiv (1-\gamma_5)/2$ and $P_R \equiv (1+\gamma_5)/2$) are represented by the subscripts of L and R, respectively. The Higgs doublet field is represented by H.

	G_μ	A_μ	B_μ	q_{iL}	u_{iR}	d_{iL}	ℓ_{iL}	e_{iR}	H
$SU(3)_C$	8	1	1	3	3	3	1	1	1
$SU(2)_L$	1	3	1	2	1	1	2	1	2
$U(1)_Y$	0	0	0	$\frac{1}{6}$	$\frac{2}{3}$	$-\frac{1}{3}$	$-\frac{1}{2}$	-1	$\frac{1}{2}$

Table 2.1: Elementary fields and their quantum numbers in the Standard Model. $U(1)_Y$ charges and $SU(3)_C$, $SU(2)_L$ representations are given.

As outlined before, the gauge interaction, the Yukawa interaction and the Higgs potential are the three parts that integrate the SM Lagrangian, $\mathcal{L}_{\rm SM}$.

$$\mathcal{L}_{\rm SM} = \mathcal{L}_{\rm gauge} + \mathcal{L}_{\rm Yukawa} + \mathcal{L}_{\rm Higgs}\,. \tag{2.4}$$

The Lagrangian $\mathcal{L}_{\rm gauge}$, for the gauge interaction, is presented by (gauge-fixing and ghosts terms are ignored)

$$\mathcal{L}_{\rm gauge} = \sum_{SU(3)_c,\,SU(2)_L,\,U(1)_Y} F^{(a)}_{\mu\nu} F^{(a)\mu\nu} + \sum_{\rm fermions} i\bar{\psi}_{i_{L(R)}} \gamma^\mu \mathcal{D}_\mu \psi_{i_{L(R)}} + |\mathcal{D}_\mu H|^2\,, \tag{2.5}$$

where $F_{\mu\nu}$ represents the gauge-field strength, and the covariant derivative $\mathcal{D}_\mu$ is defined as

$$\mathcal{D}_\mu = \partial_\mu + i g_s \frac{\lambda^a}{2} G^a_\mu + i g \frac{\tau^a}{2} A^a_\mu + i g' Q_Y B_\mu\,, \tag{2.6}$$

for the representations of a triplet of $SU(3)_C$, a doublet of $SU(2)_L$ and $Q_Y - U(1)_Y$ charge quantum numbers. The gauge coupling constants for $SU(3)_C, SU(2)_L$, and $U(1)_Y$ are g_s, g, and g', respectively. The Gell-Mann matrices denoted by λ^a (a = 1-8) are the

generators of the $SU(3)$ group, and the Pauli matrices τ^a (a = 1-3) are the generators of the $SU(2)$ group.

For the Higgs potential, the Lagrangian $\mathcal{L}_{\text{Higgs}}$ is given by

$$\mathcal{L}_{\text{Higgs}} = -(-\mu^2|H|^2 + \lambda|H|^4)\,. \tag{2.7}$$

If $\mu^2 > 0$, the Higgs field acquires the following vacuum expectation value (vev):

$$\langle H \rangle = \begin{pmatrix} 0 \\ v/\sqrt{2} \end{pmatrix}\,, \tag{2.8}$$

where $v = \mu/\sqrt{\lambda}$ ($\backsimeq$ 246 GeV). $m_H = \sqrt{2\lambda}v$ is the physical Higgs mass. As mentioned before, after electroweak symmetry breaking the $W^{\pm}$ and Z^0 gauge bosons acquire mass and the photon remains massless. These fields are formed by the $SU(2)_L$ and $U(1)_Y$ gauge fields. In terms of the parameters described above, the masses of the massive gauge bosons are $m_W = \frac{1}{2}gv$ and $m_Z = \frac{1}{2}\sqrt{g^2 + g'^2}\,v$ at tree level. Gluons, the $SU(3)$ gauge bosons, remain massless.

2.1 Yukawa sector

In the Standard Model, the gauge interactions are universal among the three families, while the interactions that distinguish between them are the Yukawa interactions of fermions, quarks and leptons, with the Higgs doublet:

$$-\mathcal{L}_{\text{Yukawa}} = [Y_e]_{ij}\bar{\ell}_i H e_j + [Y_u]_{nm}\bar{q}_n \tilde{H} u_m + [Y_d]_{nm}\bar{q}_n H d_m + \text{h.c.} \tag{2.9}$$

where $q_i = (u_{iL}\ d_{iL})^T$, $\ell_i = (\nu_{iL}\ e_{iL})^T$ are SU(2) left-handed doublets of quarks and leptons, respectively. u_m, d_m, e_j denote right-handed singlets, up or down quark and lepton, respectively. $H = (H^+\ H_0)^T$ is the Higgs doublet and $\tilde{H}$ is defined as $\tilde{H} \equiv \epsilon H^\dagger$, where $\epsilon_{12} = -\epsilon_{21} = 1$ is the SU(2) antisymmetric tensor. The electric charge is defined as $Q = T_3 + Y$, where T_3 is the diagonal generator of SU(2) and Y the hypercharge. Y_e, Y_u, Y_d are the Yukawa matrices, 3×3 complex matrices in flavor space and the subscripts i, j, n, m denote generation indices.

From linear algebra we know that we can diagonalized a complex matrix via a bi-unitary transformation

$$Y_u = V_{q_u}\hat{Y}_u V_u^\dagger \qquad Y_d = V_{q_d}\hat{Y}_d V_d^\dagger \qquad Y_e = V_l \hat{Y}_e V_e^\dagger \tag{2.10}$$

where $\hat{Y}_f$ denote diagonal matrices with non-negative entries. Given that $V_{q_d} \neq V_{q_u}$, in

the unbroken theory the quark up and down Yukawa matrices cannot be simultaneously diagonalized. Taking the basis where the up Yukawa matrix is diagonal, the down Yukawa matrix can be written in the following way:

$$Y_d = V_{q_u}^\dagger V_{q_d} D_d \equiv V D_d \,, \tag{2.11}$$

where V is known as the Cabibbo-Kobayashi-Maskawa (CKM) unitary matrix [11, 12], which in the quark sector parameterizes the flavor violation. Analogously to the weak gauge bosons, quarks and leptons acquire masses when the electroweak gauge symmetry is broken by the vev of the Higgs doublet. The Yukawa interactions allow this to happen

$$m_f = \frac{v}{\sqrt{2}} Y_f \qquad \text{where} \quad f = e, u, d \,, \tag{2.12}$$

so for the left-handed quarks, the CKM is a basis rotation that relates the gauge interaction basis with the mass eigenstate basis d'_L

$$d_{iL} = V_{ij} d'_{jL} \,. \tag{2.13}$$

The neutral currents are not affected by a unitary rotation on d quarks, this rotation only affects the charge currents. Then the CKM matrix governs the flavor-changing interactions of quarks with the W bosons

$$\mathcal{L}_W = -\frac{g}{\sqrt{2}} W_\alpha^+ V_{ij} \bar{u}_{iL} \gamma^\alpha d'_{jL} + \text{h.c.} \tag{2.14}$$

where g is the SU(2) gauge coupling, $g = e(\sin\theta_W)^{-1}$. In the lepton sector something different occurs because neutrinos are massless in the SM, and the mass and gauge eigenstate basis coincide. Then the lepton flavour $U(1)_{L_e} \otimes U(1)_{L_\mu} \otimes U(1)_{L_\tau}$ is conserved. (At non-perturbative level, the symmetry is not exact and anomalous. However, an anomaly-free symmetry is $B/3 - L_{e,\mu,\tau}$, therefore in the SM non-baryonic processes like $\mu \to e\gamma$ are strictly forbidden). If neutrinos had mass, they would provide additional flavor defining interactions and the aforementioned would not hold.

In the 1960s experiments measured a deficit in the number of electron neutrinos coming form the Sun to Earth expected, in comparison with the SM prediction, the so-called "solar neutrino problem". The solution came from neutrino oscillations that have been confirmed by many observations [13–17], which explains the discrepancy between expected and measured electron neutrinos, due to their oscillation to muon and tau neutrinos that were not observed at that time. The observation of neutrino oscillations firmly established non-zero (but for perhaps one of them) and non-degenerate neutrino masses. Then weak eigenstates are mixings of mass eigenstates

$$\nu_{iL} = \mathcal{U}_{i1}\nu_{iL} + \mathcal{U}_{i2}\nu_{2L} + \mathcal{U}_{i3}\nu_{3L} \qquad \text{with} \quad i = e, \mu, \tau \tag{2.15}$$

where $\mathcal{U}$ is known as Pontecorvo-Maki-Nakagawa-Sakata (PMNS) [18,19] matrix, which is the lepton analogue of the CKM in the quark sector. The PMNS is a unitary matrix, and it is parameterized by nine real parameters, six phases and three angles. However, not all phases are physical, and with field phase redefinitions some of them can be absorbed. The PMNS is canonically written as follows:

$$\mathcal{U} = \begin{pmatrix} c_{12}c_{13} & s_{12}c_{13} & s_{13}e^{-i\delta} \\ -s_{12}c_{23} - c_{12}s_{23}s_{13}e^{i\delta} & c_{12}c_{23} - s_{12}s_{23}s_{13}e^{i\delta} & s_{23}c_{13} \\ s_{12}s_{23} - c_{12}c_{23}s_{13}e^{i\delta} & -c_{12}s_{23} - s_{12}c_{23}s_{13}e^{i\delta} & c_{23}c_{13} \end{pmatrix} \times P \tag{2.16}$$

where we have defined $s_{ij} = \sin\theta_{ij}, c_{ij} = \cos\theta_{ij}$ and the matrix P contains two extra phases for Majorana neutrinos $P = \text{diag}(1 \quad e^{i\alpha_{12}} \quad e^{i\alpha_{31}})$, while for Dirac masses P is the identity matrix. The additional phases in P for Majorana neutrinos appear because, with self-conjugate left-handed neutrinos, fewer matrix phases can be absorbed because there are fewer relative field re-definitions to do so.

there are less relative field re-definitions that can absorb the matrix phases. Neutrino oscillations depend quadratically on neutrino masses, while Majorana phases contribute to processes that offer extra sources of CP violation, which depend linearly on neutrino masses. Therefore these Majorana phases are very difficult to observe because we cannot see them in oscillations. Using neutrino oscillation data, a recent global fit [20] obtained the following values for mixing angles and squared differences:

$$\begin{aligned} m_2^2 - m_1^2 = [6.94 - 8.14] \times 10^{-5} eV^2 \qquad |m_3^2 - m_1^2| = [2.47 - 2.63] \times 10^{-3} eV^2 \\ \sin^2\theta_{12} = [2.71 - 3.69] \times 10^{-1} \qquad \sin^2\theta_{23} = [4.34 - 6.1] \times 10^{-1} \\ \sin^2\theta_{13} = [2.000 - 2.405] \times 10^{-2} \qquad \delta = [0.71 - 1.99] \times \pi \end{aligned} \tag{2.17}$$

where normal ordering $m_1 < m_2 < m_3$ is assumed and 3σ range is displayed. Relevant matter effects depend on the sign of Δm_{21}^2 and is determined by solar neutrino observation. The absolute value of mass squared difference Δm_{31}^2 is measured with atmospheric neutrino data, and it can be consistent with inverted ordering $m_3 < m_1 < m_2$, which leads to mild differences in the best-fit values for the PMNS parameters.

2.2 How successful is the standard model?

By any reasonable measure, the Standard Model has been a staggering success. The discovery of the Higgs boson in 2012 was the culmination of the search for the particle first incorporated into the SM in 1967 and first predicted to exist in 1965. Glashow, Weinberg, and Salam's unification of the weak and electromagnetic interactions succesfully incorporated the Higgs doublet.

The precision accomplished in both theory and experiments is formidable, one the most famous examples is related to the muon magnetic dipole moment, where the experimental measurement and the SM prediction agree to within 1 part per 100 billion. There has been tremendous effort in both the experimental and theoretical communities to be able to achieve this extremely accurate comparison.

Table 2.2 shows some of the huge amount of precision observables in the Standard Model, their theory predictions and the values measured in different experiments. As we can see, both prediction and measurement have small uncertainties and there is an excellent agreement between them.

Quantity	**Value**	**Standard Model**	**Pull**
M_Z (GeV)	91.1876 ± 0.0021	91.1882 ± 0.0020	-0.3
Γ_Z (GeV)	2.4955 ± 0.0023	2.4941 ± 0.0009	0.6
σ_{had}	41.481 ± 0.033	41.482 ± 0.008	0.0
R_e	20.8040.050	20.736 ± 0.010	1.4
R_μ	20.784 ± 0.034	20.736 ± 0.010	1.4
R_τ	20.764 ± 0.045	20.781 ± 0.010	-0.4
R_b	0.21629 ± 0.00066	0.21582 ± 0.00002	0.7
R_c	0.17210.0030	0.17221 ± 0.00003	0.0
$\bar{s}^2_\ell$	0.2324 ± 0.0012	0.23155 ± 0.00004	0.7
	0.23148 ± 0.00033		-0.2
	0.23129 ± 0.00033		-0.8
A_e	0.15138 ± 0.00216	0.1468 ± 0.0003	2.1
	0.1544 ± 0.0060		1.3
	0.1498 ± 0.0049		0.6
A_b	0.923 ± 0.020	0.9347	-0.6
A_c	0.670 ± 0.027	0.6677 ± 0.0001	0.1
A_s	0.895 ± 0.091	0.9356	-0.4

Table 2.2: Z pole observables and their SM predictions. The observables with more than one value correspond to measurements from different experiments, see table 10.5 of ref. [21] for more detail.

Chapter 3

Dark Matter

The aim of this section is to give an overview of dark matter, describing in a general manner how scientist became convinced of its important role in understanding the universe (for a detailed review see ref. [22]). We will also mention the main characteristics attributable to DM; then we will focus in the so called WIMP particles (because we work under this paradigm) and in the detection strategies to find them.

Although the Swiss-American astronomer Fritz Zwicky is one of the most known and cited trailblazers in the field of dark matter, Kapteyn, Jeans, Lindblad, Öpik and Oort (see ref. [22]) were pioneers in this matter. Their studies paved the way for modern determinations of the local dark matter density, which is relevant today related with what we know as direct detection experiments, that seek to detect the scattering of dark matter particles with nuclei.

In 1933 Zwicky was studying various galaxy clusters by their redshifts. In the Coma Cluster he found a large velocity dispersion, in particular eight galaxies whose apparent velocities differed by more than 2000 km/s [23]. Hubble and Humason had already observed this large velocity dispersion in the Coma cluster unlike other galaxy clusters, but Zwicky was able to go further and estimate the mass of the Coma cluster by using the virial theorem.

In order to determine the potential energy in the Coma cluster, he first estimated the total mass of the Coma and then its size. He took 10^9 solar masses as the average mass of a galaxy (suggested by Hubble) and multiplied this number by the number of observed galaxies, 800. Then he took the physical size of the cluster to be around 10^6 light-years. Once he had the potential energy, he computed the average kinetic energy and the quantity that he would compare with his measurements, a velocity dispersion. In a sphere of 10^6 light-years containing 800 galaxies of 10^9 solar masses in average, the velocity dispersion should be 80 km/s; while the average velocity dispersion observed along the line-of-sight was about 1000 km/s.

Objects	Distance (in kpc)	Luminosity (in sol. lum.)	Mass (in sol. mass)	Mass/Lum. f
Solar Neighborhood	—	—	—	4
Triangulum Nebula, M33	480	1.4×10^9	5×10^9	4
Large Magellanic Cloud	44	1.2×10^9	2×10^9	2
Andromeda Nebula	460	9×10^9	1.4×10^{11}	16
Globular Cluster, M92	11	1.7×10^5	$<8 \times 10^5$	<5
Elliptical Galaxy, NGC 3115	2100	9×10^8	9×10^{10}	100
Elliptical Galaxy, M32	460	1.1×10^8	2.5×10^{10}	200
Average S in Double Gal.	—	1.3×10^9	7×10^{10}	50
Average E in Double Gal.	—	8×10^8	2.6×10^{11}	300
Average in Coma Cluster	25000	5×10^8	4×10^{11}	800

Figure 3.1: A snapshot of the dark matter problem in the 1950s: the distance, mass, luminosity, and mass-to-light ratio of several galaxies and clusters of galaxies, as compiled by M. Schwarzschild in 1954 [24].

From this discrepancy, he concluded:

> *"If this would be confirmed, we would get the surprising result that dark matter is present in much greater amount than luminous matter".*

Shortly after, in 1936 Sinclair Smith use a different method to estimate the mass of a cluster of galaxies, in particular he studied the Virgo cluster. Smith assumed that the outer galaxies moved in circular orbits around Virgo and calculated 10^{14} $M_\odot$ as the total mass for the cluster. Then to infer an average mass per galaxy, he divided the total mass by the number of observed galaxies, 500. In contrast with Hubble's estimate of $10^9 M_\odot$, Smith found a much higher value for the average mass per galaxy, of $2 \times 10^{11} M_\odot$.

Smith considered this discrepancy between his own calculation for the mass-per-galaxy and Hubble's estimate to be a problem, as well as Zwicky in his 1933 work, that was cited by Smith. Hubble, in his famous book *The Realm of Nebulae*, states that he consider "real and important" the discrepancy in the masses of galaxies obtained from the rotation of galaxies unlike those from the dynamics of clusters, citing the Smith's work (and not Zwicky's)

In 1954, Martin Schwarzschild [24] —son of the famous Karl Schwarzchild— taking $5 \times 10^8 L_\odot$ as an average luminosity-per-galaxy and using the updated Hubble parameter, inferred a the mass-to-light ratio of 800 that he considered "bewildering high". Fig. 3.1 shows the Schwarzschild's compilation of distance, luminosity, mass and mass-to-light ratio of the galaxies and clusters of galaxies.

By the late 1950s there was no consensus about the dark matter hypothesis in the community, they were struggling with a number of problems and could not find a unique solution. By then, it had been published several other articles on the mass-to-light ratios

of galaxy clusters. What everyone agreed on, was that in order to understand these systems more information was needed.

Around this time astronomers started to be increasingly willing to question what could this dark matter might be made of, additionally to the possibility that dark matter was required to explain the dynamics of galaxy clusters.

Herbert Rood argued that the mass responsible for the large mass-to-light ratios of galaxy clusters had to be within the intergalactic space, and not in the galaxies themselves. Rood [25] (later confirmed by Simon White [26]) came to this reasoning by studying the relaxation process of galaxy clusters.

In 1971 Meekins et al. [27] observed X-ray emission and obtained evidence that the hot intracluster gas was less than 2% of the amount required for gravitational binding.

Exotic possibilities started to be explored when gas was discarded as the explanation for the "missing mass" in galaxy clusters. However, the measurements of the primordial light element abundances also ruled out those exotic possibilities eventually. A non-baryonic nature of the dark matter was favored by these measurements.

3.1 Galactic rotation curves

Rotation curves of galaxies refer to the circular velocity profile of the gas and stars in a galaxy, depending on their distance to the center of the galaxy. The rotation curves were particularly important to establish the need of dark matter. From their rotation curves the mass distribution of galaxies can be infer, making some reasonable simplifying assumptions.

The scientific community became convinced of the need for large amounts of dark matter —in the outer regions of galaxies— to explain the observations of nearly "flat" rotation curves at large distances from the galactic center.

In 1951, the 21 cm line was detected by Edward Purcell and Harold Ewen, from Harvard. Soon enough the detection was confirmed by Australian and Dutch groups. This success had a significant impact of cosmology and astrophysics, and gave a boots to the young field of radio astronomy.

In 1959, Franz Kahn and Lodewijk Woltjer derived a lower bound on the reduced mass of the Milky Way-M31 system, since 21 cm observations of M31 —also known as Andromeda galaxy— indicated that it was moving towards the Milky Way at a speed of 125 km/s. To obtain the lower bound, they assumed that both galaxies are part of a bound system and that the age of the universe is larger than its orbital period. However, the currently accepted value of the reduced mass of the system [28] is around six times smaller than the bound derived by Kahn and Woltjer. Then they did a simple argument

that can be considered as one of the first clear hints of dark matter halos surrounding galaxies, the authors argued that this provided evidence of the local group being stabilized by intergalactic material in the form of gas.

In the 1960s, Vera Rubin and Kent Ford perform spectroscopic observations of the M31 using an image tube spectrograph developed by him. In 1970, they published their observations of the Andromeda Galaxy rotation curve [29] that were a step ahead in terms of quality.

Ken Freeman found that, for M33, rotation curves peaked at larger radii than predicted. In his 1970's paper [30], he did this comparison between the observed and predicted values at which the rotation curves would peak. For the prediction of the radius, he assumed an exponential disk with a scale length fit to photometric observations, and compared it with the observation of the 21 cm rotation curve. This combination of radio observations extending beyond the optical disk and theoretical modelling, allowed Freeman to come to a surprising conclusion:

> *"if [the data] are correct, then there must be in these galaxies additional matter which is undetected, either optically or at* 21 *cm. Its mass must be at least as large as the mass of the detected galaxy, and its distribution must be quite different from the exponential distribution which holds for the optical galaxy".*

In 1972, a similar analysis was performed by G. Shostak and D. Rogstad [31]. Using the radio telescope at the Owens Valley Radio Observatory, they obtained the rotation curves of five galaxies —M33, NGC 6946, M101, IC 342 and NGC 2403—. When analyzing these rotation curves, Rogstad and Shostak found that they remained flat out to the largest radii observed. Then, following Freeman's method, they derived mass-to-light ratios and obtained values as big as 20 at large radii. Rogstad and Shostak explicitly say in their paper that they:

> *"confirm[ed] the requirement of low-luminosity material in the outer regions of these galaxies".*

One of the first to acknowledge the importance of the observed flatness of galactic rotation curves was Morton Roberts. In 1973, he and Arnold Rots, extended the analysis to M101 and M81, and argued that in their outer parts, these spiral galaxies each exhibited flat rotation curves, as shown in fig. 3.2 [32]. The interpretation of these data by the authors was unambiguous:

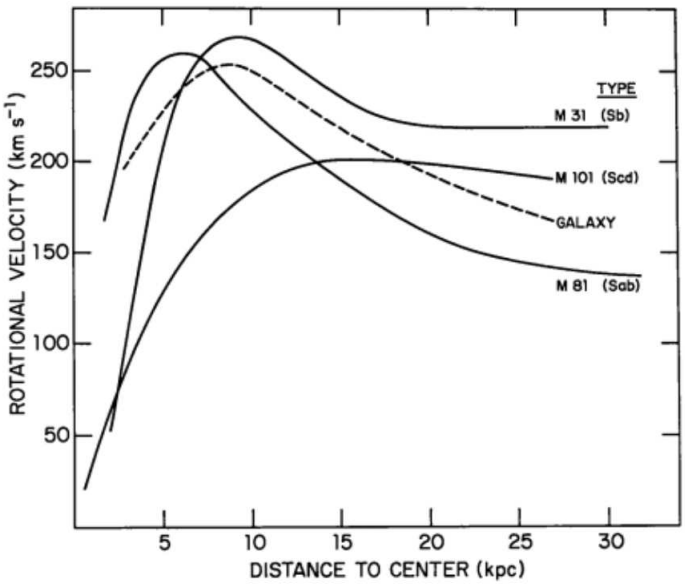

Figure 3.2: The rotation curves obtained by Roberts and Rots in 1973 for the galaxies M81, M31 and M101 (solid lines) . For comparison, the authors include the rotation curve of the Milky Way Galaxy. From ref. [32].

> *"The three galaxies rotation curves decline slowly, if at all, at large radii, implying a significant mass density at these large distances. It is unreasonable to expect the last measured point to refer to the 'edge' of the galaxy, and we must conclude that spiral galaxies must be larger than indicated by the usual photometric measurements [...]. The present data also require that the mass to luminosity ratio vary with radius increasing in distance from the center".*

The existence of large amounts of mass in the outer parts of galaxies had almost be completely established through the flatness of the rotation curves obtained by radio astronomers in 1974. However, not the entire the astronomical community was convinced of this idea [33].

Albert Bosma published the results of his PhD thesis [34] in 1978, including the velocity fields by radio observation of 25 galaxies and their corresponding rotation curves. His work confirmed that most of these galaxies had flat rotation curves out to the largest observed radius, exceeding again their optical size. Bosma's observations showed that the mass of these galaxies continued to grow beyond the region occupied by gas and stars. A few months later, Rubin, Norbert Thonnard and Ford published their observations of ten high-luminosity spiral galaxies [35]. To the outermost measured radius, the optical rotation curves were flat.

In 1979, Sandra Faber and John Gallagher made a timely and complete review of the status of mass-to-light-ratios and galaxy masses [36]. The abstract of that paper gives a

transparent indication of its content:

> *"The current status of the 'missing mass' problem is reviewed on the basis of standardized mass-to-light (M/L) ratios of galaxies. The stellar mass density in the immediate vicinity of the sun is examined, along with the mass of the Milky Way and the M/L ratios of spiral galaxies, E and S0 galaxies, and binary galaxies. The dynamics of small groups of galaxies is investigated, and mass derivations for cluster galaxies are discussed. It is concluded that the case for invisible mass in the universe is very strong and becoming stronger".*

3.2 Dark Matter Particles

The very meaning of the phrase "dark matter" has evolved significantly over the past few years. Nowadays there is a consensus on what we mean when we talk about it, we refer to whichever particle species accounts for most of the matter density of our Universe. In the early usage of this phrase, it could refer to several astrophysical material, including white dwarfs, cold clouds of gas, neutron stars and anything that was too tenuous to be detected with available telescopes.

By the middle of the 1980s, emerged the possibility to test neutrino dark matter, by using a new tool, numerical simulations. This tool allowed to assess the impact and cosmological role of dark matter particles on the formation of large scale structure, by predicting how would evolved the number of dark matter particles in an expanding universe under the force of gravity. In some cases, these test could help discriminate between different dark matter candidates.

By numerical simulations it can be probed whether a given particle dark matter candidate was non-relativistic (cold) or relativistic (hot) during the structure formation epoch. Simulations have that cold dark matter particles follow a "bottom-up" sequence of structure formation, starting with small halos, going later through a succession of mergers to form larger halos. Hot dark matter would follow the opposite sequence, "top-down", they would tend to form very large structure first upon collapsing and going on later through fragmentation of larger halos to form smaller (i.e. galaxy-sized) ones. One example of hot dark matter are the SM neutrinos, that are are expected to emerge with a highly relativistic velocity distribution from the early Universe since they are very light thermal relics [37, 38].

It quickly became clear, from these early simulations, that cold and hot dark matter lead to very different scenarios of large scale structure. By comparing the observations of galaxy surveys (in particular the first extensive 3D survey of galaxies in the local Universe [39], the CfA survey,) with the results of these simulations, it was determined

that hot dark matter, and specifically SM neutrinos, could not be responsible for most of the dark matter in the Universe [40].

3.2.1 The WIMP paradigm

By the end of the 1980s, cold and non-baryonic particles had become the leading paradigm, although another alternatives continued to be discussed. At the epoch, the idea that the bulk of the mass in the Universe consisted of cold dark matter —in the form of some unknown species of elementary particle—, had become widely accepted by many particle physicists and astrophysicists.

A particle species must not be too light (roughly heavier than $\sim 1-100$ keV) in order to become a cold relic, that is, to freeze-out of thermal equilibrium in the early Universe. The relevant quantity is the self-annihilation cross section, which must be of the order of $\sigma\, v \sim 10^{-26}\mathrm{cm}^3/\mathrm{s}$ (where v is the relative velocity between the annihilating particles), such that the predicted relic density of this species matches the observed dark matter abundance. This number of σv is remarkably similar to the cross section that emerges from the weak interaction.

For example, a stable particle with a mass of the order of GeV, annihilating through Z-boson exchange, would freeze-out with a relic density that is approximately equal to the measured abundance of dark matter. Such conclusions apply to a wide range of dark matter candidates near the electroweak-scale, including any number of stable particles with electroweak-scale interactions and MeV-TeV masses.

3.2.2 The Universe's Baryon Budget

Baryonic abundance determinations were initially based on light element abundance measurements, until the satellite-based WMAP experiment enabled competitive (and better) determinations.

The Planck Collaboration, in its most recent analysis, reaches the constraint $\Omega_b h^2 = 0.0224 \pm 0.0001$, corresponding to less than 0.05% fractional uncertainty [41], while a measurement of $\Omega_b h^2 = 0.02264 \pm 0.00050\,(68\%\mathrm{CL})$ was ultimately achieved by WMAP [42]. Comparing there numbers to the total matter density in the Universe, obtained by these and other experiments, inevitably one concludes that baryonic matter is less than 20% of the total matter density.

3.2.3 Discrepancies At All Scales

Over the decades after the 1930s, the need for dark matter in galaxies was mainly considered independently of its presence in clusters. These mass discrepancies at multiple scales began to be discussed again within a common context until the 1960s.

In his pioneering paper of 1963, Arrigo Finzi cited several previous articles, and argued in favor of a common interpretation of these phenomena [43]: the more recent determinations of the Milky Way's mass, the observation of M31's rotation curve from van de Hulst *et al.* in 1957 as well as Zwicky's work on galaxy clusters in 1933.

The aforementioned review "Masses and mass-to-light ratios of galaxies" [36] published by Sandra Faber and John Gallagher in 1979, played an outstanding role in crystallizing the opinion among astronomers and cosmologists that in the Universe dark matter was indeed abundant.

Jim Peebles pointed out in 1982 that a Universe that was composed of only baryonic matter was incompatible with the absence of fluctuations at a level of $\sim 10^{-4}$ in the cosmic microwave background. He also argued that, if the Universe was instead dominated by weakly interacting, massive particles, whose density fluctuations could start to grow prior to decoupling, this problem would be alleviated [44].

Cold dark matter as the leading paradigm to explain the evolution and structure of the Universe at all scales, was established from the great attention that these and other papers received from the scientific community.

3.3 Features of DM

The following observationally-motivated constraints must be fulfilled by any dark matter particle candidate:

(i) The dark matter relic density needs to account for the observed cold dark matter abundance;

(ii) In order to agree with the observation of structure formation in the early Universe, the DM particle should be non-relativistic at matter-radiation equality. Therefore, the mass of the dark particle cannot be arbitrarily light if the DM was produced in the early universe as a thermal relic. Specifically, DM masses below a few keV are ruled out by cosmological simulations [45–47].

(iii) From direct detection experiments, as well as a result of null searches for stable charged particles [48,49], the DM should be effectively neutral under electromagnetic interaction;

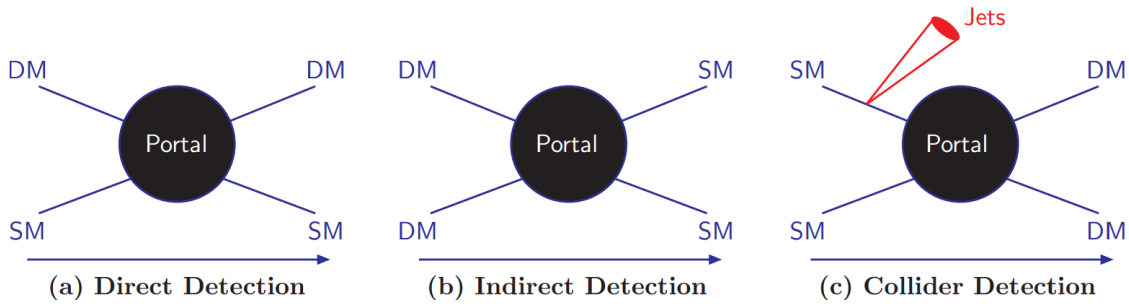

Figure 3.3: Illustration of dark matter-standard model interactions. At present, we do not know how or if such interaction occurs.

(iv) Since its presence is observed today, the dark matter particle must be stable in cosmological scale, that is, its lifetime has to be greater than the age of the Universe;

(v) The level of self-interactions that DM particles can have is limited by cluster collisions, such as the Bullet Cluster [50].

3.4 Detection Strategies

This section focuses on WIMPs detection strategies.

3.4.1 Direct Detection

Direct DM detection looks for the scattering of the WIMP particle with the nuclei through the measurement of the nuclear recoil, see fig. 3.3. Considering WIMP velocities around $v \sim 10^{-3}$ and a typical mass of $m_\chi \sim 100$ GeV, at most the deposited recoil energy is ~ 100 keV, therefore these experiments require low-background, highly-sensitive detectors placed deep underground. There are different experimental techniques to measure the nuclear recoil produced by the WIMP scattering, which are currently used in direct detection experiments.

3.4.2 Indirect Detection

Indirect detection strategies seek to measure signals related to fluxes of particles originated in astrophysical structures from WIMP decays or annihilations, see fig. 3.3. The search has been focused on photons, antimatter, and neutrinos, using satellites such as Fermi-LAT [51,52] and AMS [53], or Earth based telescopes such as CTA [54] and H.E.S.S. [55].

When probing WIMP models by means of indirect DM detection, there is an interesting fact, bounds on the annihilation cross section, σv today are directly connected

to the DM relic abundance, as long as σv is not velocity dependent. For example, the observation of positron fluxes by AMS-02, resulted in stringent limits on the *annihilation cross section vs WIMP mass* plane.

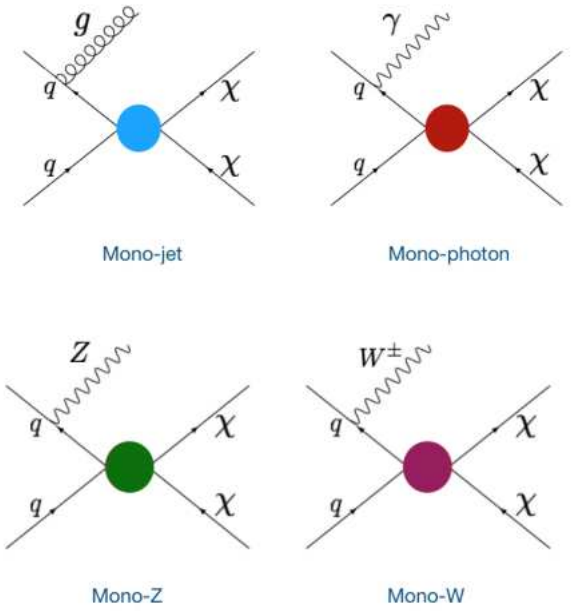

Figure 3.4: Possible mono-X signatures from dark matter production in association with a gluon jet, photon, Z or $W^{\pm}$.

3.4.3 Collider Searches

The production of WIMPS in association with one or more SM particles might occur as a result of proton-proton collisions in the LHC. At colliders, WIMPs would manifest as missing energy since they are cosmologically stable and electrically neutral. For this reason, these kind of DM searches are referred to as mono-X searches, based on the observation of the visible side of the event such as a photon, jets or charged leptons, see figs. 3.3 and 3.4. To reduce the standard model background and potentially disentangle a dark matter signal, events with large missing energy are selected.

However, collider experiments can simply confirm the presence of a stable, neutral particle, but they cannot uniquely determine the presence of DM in a signal event, since they can only identify missing energy. The particle measured might have even decayed outside the detector.

Anyway, WIMPs searches in colliders are exciting and complementary strategies.

Chapter 4

Charged Lepton Flavor Violation

In the Standard Model, lepton flavor is a conserved quantity since there are not right-handed neutrinos and neutrinos are massless. The observation of neutrino oscillations proved that lepton flavor is not a symmetry of nature as it provided clear evidence about massive neutrinos and non-zero mixing angles. Therefore charged Lepton Flavor Violation (cLFV) is expected to occur although it has not been observed yet; cLFV means short-range interaction among the charged leptons.

If neutrinos get their masses similarly than the other fermions in the SM, through Yukawa interactions with the Higgs boson, the expected rates for cLFV processes are practically unobservable, as they are typically suppressed through the GIM mechanism [60], $G_F^2 m_\nu^4 \sim 10^{-50}$. Thus the experimental observation of charged lepton flavor violation would be a clear signature of new physics, and could shed light on the origin of neutrino masses. Consequently, over the last 75 years, there has been a strong experimental program searching for different cLFV processes, some of them shown in fig. 4.1. From these different observables, we can obtain non-trivial and complementary information regarding the nature of new physics, because their rates cannot be estimated in a model independent way, thus testing possible scenarios of physics beyond the standard model (BSM).

Additionally, in the SM lepton flavor is an accidental symmetry, which means that it is a symmetry of the more general Lagrangian with renormalizable, gauge invariant interactions. Therefore, regardless of neutrino masses, extra sources of charged lepton flavor violation can be easily introduced by minimal departures from the standard model and lead to sizeable cLFV rates.

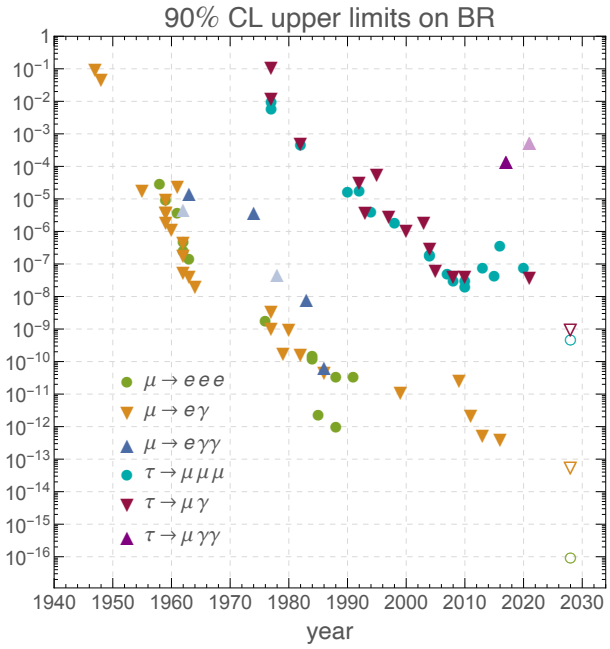

Figure 4.1: Upper limits at the 90%CL on several cLFV leptonic decays and their evolution over time. Published direct experimental searches are shown with solid markers. Future expected sensitivities at Mu3e [62], MEG II [63] and Belle II [64] (arbitrary year) are indicated with empty markers. By recasting the available searches for $\mu e \to \gamma\gamma$ [65] or $\ell_i \to \ell_j \gamma$ [66, 67], limits for $\ell_i \to \ell_j \gamma\gamma$ were obtained and are shown with lighter markers. The evolution of the $\tau \to e$ and $\tau \to \mu$ sectors is similar, except that there is no direct search for $\tau \to e\gamma\gamma$.

4.1 cLFV in a simple model that generates neutrino masses at tree level

If we add three right-handed neutrinos ν_{Ri} to the content of the SM, singlets under the SM gauge group, we would have Yukawa couplings between the Higgs doublet and the leptons. After SSB, these terms would generate Dirac masses for the neutrinos

$$-\mathcal{L}_\nu = [Y_\nu]_{ij}\, \bar{\ell}_i \tilde{H}\, \nu_{Rj} + \text{h.c.} \tag{4.1}$$

Analogously to quark sector, where the CKM arises, there is a misalignment between the neutrinos and charged leptons in the mass basis, which gives rise to the PMNS matrix, as the charged lepton and neutrino Yukawas cannot be diagonalized at the same time respecting the electroweak gauge symmetry. Thus, in the lepton sector, in the charged lepton currents, the presence of the PMNS matrix parameterizes the flavor violation

$$\mathcal{L}_W = -\frac{g}{\sqrt{2}} W^-_\alpha \sum_{\substack{i=e,\mu,\tau \\ j=1,2,3}} \mathcal{U}_{ij} \bar{e}_{iL} \gamma^\alpha \nu_{jL} + \text{h.c.} \tag{4.2}$$

Neutrino mixing would mediate the charged lepton flavor violation. A consequence of the flavor-changing interactions in eq. (4.2) is shown in figure 4.2, as a representative diagram for the $\mu \to e\gamma$ decay. The only relevant piece in the amplitude of this process is a dipole transition

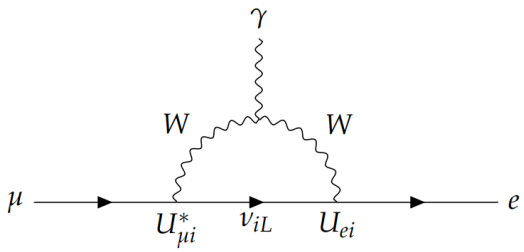

Figure 4.2: $\mu \to e\gamma$ decay generated by massive neutrinos ν_{iL}.

$$\mathcal{M}(\mu \to e\gamma) = \bar{u}_e(p_e) \Big[i\sigma_{\alpha\beta} q^\beta m_\mu (A_R P_R + A_L P_L) \Big] u_\mu(p_e + q) \epsilon^{*\alpha}(q) \,, \tag{4.3}$$

which is proportional to the muon mass due to a chirality flip (neglecting the electron mass). Using the Yukawa term in eq. (4.1) the following decay rate is obtained [10]

$$\Gamma(\mu \to e\gamma) = \frac{m_\mu^5}{16\pi} (|A_L|^2 + |A_R|^2). \tag{4.4}$$

The outgoing electron in the diagram of figure 4.2 is left-handed and only A_R is different from zero. The amplitude is proportional to the propagator of the internal neutrino, and for small neutrino masses it can be expanded as

$$\sum_i \frac{\mathcal{U}^*_{ei} \mathcal{U}_{\mu i}}{k^2 - m_i^2} = \sum_i \frac{\mathcal{U}^*_{ei} \mathcal{U}_{\mu i}}{k^2} + \sum_i \frac{\mathcal{U}^*_{ei} \mathcal{U}_{\mu i}}{k^2} \left(\frac{m_i^2}{k^2} \right) + \mathcal{O}\left(\frac{m_i^4}{k^4} \right). \tag{4.5}$$

We can see that due to the unitarity of the PMNS matrix, the leading term vanishes, and there is GIM suppression in the amplitude by the square of neutrino masses. In fact, this process is GIM suppressed in a manner analogous to what happens in the quark sector with flavor changing neutral currents by CKM unitarity [60]. The computation is done in the R_ξ gauge in [68], incorporating diagrams where W bosons are replaced by charged Goldstones. The resulting decay rate for $\mu \to e\gamma$, divided by the rate of the dominant lepton flavor conserving three-body decay $\Gamma(\mu \to e\nu\bar{\nu}) = G_F^2 m_\mu^5/(192\pi^3)$, is

$$BR(\mu \to e\gamma) = \frac{3\alpha_e}{32\pi} \left| \sum_i \mathcal{U}^*_{ei} \mathcal{U}_{\mu i} \frac{m_i^2}{m_W^2} \right|^2 . \tag{4.6}$$

Substituting the best-fit values in eq. (2.17) for the mixing parameters and mass differences, the prediction $BR(\mu \to e\gamma) = 10^{-54} - 10^{-55}$ is obtained, which is too much suppressed to ever be observed. Other LFV processes are similarly GIM suppressed in models with Dirac neutrino masses, thus beyond any foreseeable experimental reach [69–75]. Indeed rates in traditional seesaws are also unobservably small [76–78], so their discovery would point unambiguously to new physics, e.g. some other mechanism for neutrino mass generation, like low-scale seesaws [79–81] (see e. g. refs. [82–84] for recent analyses).

4.2 cLFV searches using Muons

Experiments involving muons have been, so far, the most popular in the history of cLFV searches. Hinks and Pontecorvo performed the first experiment looking for cLFV, using atmospheric muons [85]. Huge progress have been done since then at different facilities (TRIUMPH, LANL, PSI, etc.), high-intensity muon beams at the level of $10^8(10^7)\mu^+(\mu^-)/s$ [61, 86] have been developed thanks to advancements in the muon beam production and acceleration technologies, thus allowing the possibility of seeking for rare cLFV processes.

Dedicated searches for muon-cLFV processes performed by experiments have provided the current best limits for the following processes: $\mu^\pm \to e^\pm e^- e^+$, $\mu^+ \to e^+\gamma$, $\mu^-\mathrm{N} \to e^+\mathrm{N}'$ and $\mu^-\mathrm{N} \to e^-\mathrm{N}$. One interesting thing to notice, is that most of the searches were performed using μ^+ rather than μ^-, except for experiments involving nuclei. Several advantages motive this choice: (i) how the muon beam is obtained; proton-target interactions produce a larger number of π^+ than of π^-, that then decay into μ^+, resulting in a μ^+ beam of higher intensity, (ii) μ^- can undergo nuclear capture events, then producing photons, neutrons and protons, and consequently deteriorating the performance of the detectors by increasing their activity, while μ^+ cannot get captured in nuclei.

4.3 $\mu^+ \to e^+\gamma$

The Crystal Box experiment at Los Alamos Meson Physics Facility (LAMPF) [87] was one of the first experiments to adopt a calorimetric solution for the photon detection. They established an upper limit of 4.9×10^{-11} at 90% C.L. with a maximum likelihood analysis. MEGA [88] was the next generation experiment, and was also performed at LAMPF. As an example of how challenging it is to make progress in this type of search,

MEGA reached a final sensitivity that was ~ 35 times worse than the designed value, they obtained 1.2×10^{-11}@ 90% C.L. The MEG experiment [89] established the current best limit, 4.2×10^{-13}@ 90% C.L., for the $\mu^+ \to e^+\gamma$ branching ratio.

4.4 cLFV searches using Taus

Due to the large tau mass, $m_\tau \approx 1.777$ GeV, the tau lepton is a very promising source of cLFV decays, and many cLFV channels can be searched for: $\tau^\pm \to e^\pm\gamma, tau^\pm \to \mu^\pm\gamma, \tau \to 3\ell, \tau \to \ell + h, \ldots$ (where h denotes a light hadron and $\ell = e, \mu$).

However, a difficulty immediately arises from the experimental point of view: The tau lepton has a very short lifetime, $\tau = 2.91 \times 10^{-13}$ s, it is unstable. Consequently, tau beams cannot be realized, and large tau samples may only be obtained in intense proton or electron accelerators, and the tau production cross section must be large at the operating energies of the accelerators. Besides, most of the tau leptons are not produced at rest in the pp and e^+e^- collider machines, which means that experiments need to deal with decays-in-flight. Therefore, detectors are challenged to offer wide-range calibrations (from a few hundred MeV to several GeV), because due to the boost, the decay products could reach energy values of up to various GeV. For these kind of searches, events contain a pair of taus; the so-called tag side is the one where the tau undergoes SM decay, while on the signal side, cLFV candidates are selected depending on the adequate topology of each individual channel. The tagging side accepts 1-prong hadronic and leptonic ($\tau \to \ell\nu\bar{\nu}$) decays.

Chapter 5

Effective Field Theory

One amazing thing about our world is that it seems that we can find new physical phenomena at all scales, when exploring new regimes in energy, time or distance. We can identify physical phenomena worthy of study in almost every regime, from the lifetime of a weak gauge boson, a few times 10^{-25} s, to the age of the universe, about 10^{18} s.

To be able to study and describe physics amidst this extraordinary richness, it is convenient to isolate the phenomena of interest from all the rest, so we can focus on them without without being forced to understand everything.

Fortunately, this is often possible. We can take different regions in the parameter space of the world, and found a proper description of the relevant physical phenomena. An "effective theory" is precisely what we mean by this proper description of the relevant physical phenomena. There is no unique description of physics that is valid everywhere in parameter space.

The common idea is the following: we focus on the physical quantities of interest and check if there are parameters (with the same dimension) that are very small or very large in comparison, then by taking the very large parameters to infinity and the very small to zero, we may arrive to a simpler approximate description of the relevant physics. We can then include the neglected effects as small perturbations about this simpler rough starting point.

These is a trick that has been commonly used without even thinking about it and which is responsible of much of our current understanding of physics, that would not have been possible other way. An example of how we use this trick all the time is the fact that we do not study Newtonian physics as the limit, for small velocities, of relativistic mechanics, but as a separate discipline. Basically we ignore relativity in the (familiar) parameter space region in which the speed of light is much larger than all the velocities. And we do this simply because is easier to neglect relativity, but in any case, it is completely fine to treat mechanics in a fully relativistic way.

Being smart enough, in principle one can always do any calculation in the full theory. However, using an effective field theory is very convenient. The advantage of the effective theories is that one is forced to focus on the important physics and thus they make calculations easier.

When applying effective theories in particle physics, distance scale is the relevant parameter. The strategy in particle physics is to take the distance scale of interest, and then any features of the physics that are small in comparison are reduced to zero size. In this way we arrive to the simple and useful picture of the relevant physics. We can later include the small, ignored finite size effects as perturbations.

An effective quantum field theory is particularly helpful because the particles that are too heavy to be produced, are amongst the short-distance features that can be neglected in an effective theory. A huge simplification occurs when removing the heavy particles from the effective theory. A particularly interesting feature of EFTs is their necessity of ultraviolet regularization. The limit at which the short-distance scales are reduced to zero size must be handled carefully, making the effective theory building process non-trivial. The renormalization group running of effective constants with the renormalization scale, μ, is an implication of the ultraviolet behavior. The running of coupling constants is changed in effective theories by trading for scale dependence the logarithmic dependence on heavy particle masses.

In the effective theory the nontrivial effects of the eliminated heavy particles appear in interactions generated by operators with dimension higher than four, and the theory is non-renormalizable. Those effects are included in the nonlocal interactions from virtual heavy-particle exchange in the full theory. In the effective theory, a set of local interactions, constructed to give the same physics at low energies, replace nonlocal interactions. In this process, the high energy behavior of the theory is modified, so that the description of the physics by the effective theory is valid only for energies below the masses of the heavy particles. Thus in energy scales, the utility region of an effective theory is necessarily limited from above.

In the same way, the utility domain of the effective theory is bounded from below if it describes light particles with nonzero mass. Within the effective theory, at small enough energy scales, below the masses of the heaviest particles, it is useful and possible to change theories once again, eliminating the heaviest particles and arriving at a new effective theory. This lower bound is simply a convenience, while the upper bound is an absolute.

Renormalizability is not a problem in effective theories even when they contain an infinite number of terms. At a given order in energy expansion, a finite number of couplings specifies the low-energy theory, and this allows for an order-by-order renormalization.

The theoretical foundation of effective field theory can be stated as a theorem [91]:
"For a given set of asymptotic states, perturbation theory with the most general Lagrangian containing all terms allowed by the assumed symmetries will yield the most general S-matrix elements consistent with analyticity, perturbative unitarity, cluster decomposition and the assumed symmetries".

5.1 The principles of Effective Field Theory

The basic ingredients needed to build an effective field theory can be summarized as a set of general principles:

(i) The details of the dynamics at high energies (short distances) are not indispensable for the description of the dynamics at low energies (large distances).

(ii) At a considered scale, choose the adequate description of the relevant physics. Put to infinity (zero) the heavy (light) scales, if there are large energy gaps, i.e.

$$0 \leftarrow m \ll E \ll M \rightarrow \infty.$$

We can incorporate the finite corrections induced by these scales as perturbations.

(iii) A set of local, nonrenormalizable interactions among the light particles, replace the non-local heavy–particle exchanges.

(iv) The effective field theory describes, in terms of a finite set of parameters, the low–energy physics, to a given precision ϵ:

$$(E/M)^{d_i-4} \gtrsim \epsilon \quad \longleftrightarrow \quad d_i \lesssim 4 + \frac{\log(1/\epsilon)}{\log(M/E)}\,. \tag{5.1}$$

(v) The underlying fundamental theory and the EFT have the same infra-red behaviour and different ultraviolet behaviour.

(vi) The symmetries of the EFT and its low–energy couplings are the only remnants of the high–energy dynamics.

5.2 The Fermi Theory of Weak Interactions

In this section I present a brief explanation of the Fermi theory that describes the weak interaction at energy scales below the mass of the W boson. This will serve to illustrate

with a simple and physically relevant example the general principles introduced in the previous section.

In the Standard Model, at lowest order, the weak decays are generated between two fermionic left–handed currents by the exchange of a $W^{\pm}$ (except for the heavy quark top whose mass allows it to decay into a real W^{+}). In these decays, in comparison with its mass, m_W, the momentum transfer carried by the W boson is very small. For this reason, the vector–boson propagator can be reduced to a contact interaction:

$$\frac{-g_{\mu\nu} + q_\mu q_\nu / m_W^2}{q^2 - m_W^2} \quad \xrightarrow{q^2 \ll m_W^2} \quad \frac{g_{\mu\nu}}{m_W^2} \,. \tag{5.2}$$

Thus, an effective local 4-fermion Hamiltonian can describe these flavour–changing interactions,

$$\mathcal{H}_{\text{eff}} = \frac{G_F}{\sqrt{2}} \mathcal{J}_\mu \mathcal{J}^{\mu\dagger} \,, \tag{5.3}$$

where $\mathcal{J}_\mu$ denotes a fermion current

$$\mathcal{J}_\mu = \sum_{ij} \bar{u}_i \gamma_\mu (1 - \gamma_5) V_{ij} d_j + \sum_{\ell} \bar{\nu}_\ell \gamma_\mu (1 - \gamma_5) \ell \,, \tag{5.4}$$

V_{ij} is the Cabibbo–Kobayashi–Maskawa mixing matrix, and

$$\frac{G_F}{\sqrt{2}} = \frac{g^2}{8 m_W^2} \,, \tag{5.5}$$

where G_F is the so-called Fermi coupling constant.

At low energies (meaning $E \ll m_W$), it is not possible to produce a physical W boson, because the energy is not enough, and then we can safely ignore the W field in the theory. The effective Hamiltonian in (5.3) contains dimension-6 operators and, accordingly, the effective coupling has dimension -2. In fact, eq. (5.5) shows was is technically called a *matching condition*, the relation between the parameters of the underlying electroweak theory, g, m_W, and the effective coupling constant, G_F. The effective 4–fermion Hamiltonian describe well the transition amplitudes corresponding to the different quark and lepton weak decays.

Fermionic operators of higher dimensions generate corrections to (5.3), and can be derived by further expanding the W propagator in powers of q^2/m_W^2. With the operators in eq. (5.3) we would obtain an accuracy of order of m_f^2/m_W^2, where m_f denotes the mass of the decaying fermion; as long as we are satisfied with this precision, we can neglect contributions of the higher dimensional operators.

The decay width of the leptonic decay $\ell \to \nu_\ell \ell' \bar{\nu}_{\ell'}$ can be easily calculated, obtaining:

$$\Gamma(\ell \to \nu_\ell \ell' \bar{\nu}_{\ell'}) = \frac{G_F m_\ell^5}{192\pi^3} f(m_\ell/m_{\ell'})\,, \tag{5.6}$$

where $f(x) = 1 - 8x + 8x^3 - x^4 - 12x^2 \ln x$.

The global mass dependence, $\Gamma \sim G_F^2 m_\ell^5$, is expected from dimensional analysis, since Γ must have dimension 1 and the Fermi constant has dimension -2. Thus, except for the top decay, this mass dependence is universal of the weak decays of fermions.

The factor $1/(4\pi)^3$ is generated by the three–body phase space; therefore the explicit calculation is only needed to derive the dependence on the daughter particle mass, contained in the function $f(m_\ell/m_{\ell'})$, and the remaining numerical factor of $1/3$.

If we include the additional 4–fermion operators generated by Z exchange, the low–energy neutrino scattering with either leptons or quarks can also be described by the effective Hamiltonian.

Chapter 6

Dark Matter: Spin-one mediators with SM fields

6.1 Overview

In absence of any direct DM signal, the generality of the EFT approach may be advantageous (see e.g. refs. [93–97] in this context). Here we will continue exploring the phenomenological consequences of the EFT scenario developed in ref. [98] for the interactions between SM and DM particles with heavy mediators. In particular, we will focus on the case of spin-one mediators (either in the Proca or antisymmetric tensor representations), that has received considerably less attention in the literature (see however [99]) than the Higgs portal (see ref. [100] and references therein) and neutrino portal [101–117] cases. According to the WIMP freeze-out scenario, DM masses naturally lie in the GeV-TeV range. We will focus in this chapter in the low-energy region that is the one most restricted by observations, with DM masses under m_Z (we take this upper bound instead of m_H because in our EFT, considering only interactions with spin-one mediators, the invisible Higgs decay width is not modified at leading order). In this case, even the heavy mediators could eventually be found at the LHC.

For DM particle mass in this region the main observational/experimental constraints are: the invisible Z decay width [118] [1], the observed relic density [118] and direct detection limits from Xenon1T [119], PandaX [120], LUX [121], DarkSide-50 [122] and CRESST-III [123]. We also employed recent indirect detection bounds (searching for excess gamma ray emissions) derived from dwarf spheroidal galaxy observations released by the Fermi-LAT and DES Collaborations [124]. We also used the results of indirect DM searches based on antimatter detection, specifically, the limits on the annihilation cross

[1] Other W, Z boson decays give less restrictive constraints.

section derived in ref. [125] using the AMS-02 data on the positron flux [126].

This chapter is organized as follows: in section 6.2 we introduce the effective field theory that we are using [98] and highlight the part interesting for our study and our conventions. Then, in section 6.3 we compute the bounds that the invisible Z decay width puts on our several possible DM candidates. After that, in section 6.4 we verify that the observed relic density can be reproduced in the different cases. Next, in section 6.5 we analyze some observational limits: in subsection 6.5.1 we check that direct detection bounds are respected; and in subsections 6.5.2 and 6.5.3 we consider the indirect bounds given by dwarf spheroidal galaxies and the positron flux, respectively. We discuss our results and conclude in section 6.6.

6.2 Effective field theory

We ensure the stability of a dark sector particle by assuming [127, 128] that all dark fields transform non-trivially under a symmetry group $\mathcal{G}_{\rm DM}$ (that will remain unspecified), while all SM particles are supposed to be $\mathcal{G}_{\rm DM}$ singlets. We will also assume that all dark fields are singlets under the SM gauge group $\mathcal{G}_{\rm SM} = SU(3) \otimes SU(2) \otimes U(1)$.

The generality of EFT formulations, described in chapter 5, is also adequate for dark matter interactions [94, 97, 129–135]. We will follow this approach in the particular case where the SM-DM interactions are generated by heavy mediators exchange of singlets under $\mathcal{G}_{\rm DM} \times \mathcal{G}_{\rm SM}$. Thus interactions between the dark and Standard-Model sectors will be of the form

$$\mathcal{O} = \mathcal{O}_{\rm SM}\mathcal{O}_{\rm dark}\,, \tag{6.1}$$

where $\mathcal{O}_{\rm SM,dark}$ stands for local operators made of standard model and dark matter fields, respectively (singlets under $\mathcal{G}_{\rm SM,DM}$, in turn).

For building $\mathcal{O}_{\rm dark}$ we will assume [98] the following possible dark sector particles: scalars Φ, Dirac fermions Ψ and Proca vectors X (only one or a couple of them may be realized in Nature).

The assumption that all dark fields transform non-trivially under $\mathcal{G}_{\rm DM}$, implies that $\mathcal{O}_{\rm dark}$ will contain at least two fields. The list of the operators $\mathcal{O}$ of dimension ≤ 6 satisfying the above conditions is given in table 6.1 [98].

In category VII, $\mathcal{J}^{\mu}_{\rm SM,\ dark}$ represents a dimension 3 vector current, either dark or standard:

$$\begin{aligned} \mathcal{J}^{(\psi)\mu}_{\rm SM} &= \bar{\psi}\gamma^{\mu}\psi, \qquad & \mathcal{J}^{(\varphi)\mu}_{\rm SM} &= \tfrac{1}{2i}\varphi^{\dagger}\overleftrightarrow{D}^{\mu}\varphi, \\ \mathcal{J}^{(L,R)\mu}_{\rm dark} &= \bar{\Psi}\gamma^{\mu}P_{L,R}\Psi, & \mathcal{J}^{(\Phi)\mu}_{\rm dark} &= \tfrac{1}{2i}\Phi^{\dagger}\overleftrightarrow{D}^{\mu}\Phi, \end{aligned} \tag{6.2}$$

dim.	category	operator(s)
4	I	$\lvert\varphi\rvert^2(\Phi^\dagger\Phi)$
	II	$\lvert\varphi\rvert^2\bar{\Psi}\Psi$ $\quad$ $\lvert\varphi\rvert^2\Phi^3$
5	III	$(\bar{\Psi}\Phi)(\varphi^T\epsilon\ell)$
	IV	$B_{\mu\nu}X^{\mu\nu}\Phi$ $\quad$ $B_{\mu\nu}\bar{\Psi}\sigma^{\mu\nu}\Psi$
	V	$\lvert\varphi\rvert^2\mathcal{O}^{(4)}_{\rm dark}$ $\quad$ $\Phi^2\mathcal{O}^{(4)}_{\rm SM}$
6	VI	$(\bar{\Psi}\Phi^2)(\varphi^T\epsilon\ell)$ $\quad$ $(\bar{\Psi}\Phi)\not{\partial}(\varphi^T\epsilon\ell)$
	VII	$\mathcal{J}^\mu_{\rm SM}\mathcal{J}_{{\rm dark}\,\mu}$
	VIII	$B_{\mu\nu}\mathcal{O}^{(4)\mu\nu}_{\rm dark}$

Table 6.1: Effective operator list up to dimension 6 involving dark and SM fields; where: φ is for the SM scalar isodoublet, B the hypercharge gauge field, and ℓ a left-handed lepton isodoublet; also, $\epsilon = i\sigma_2$, where σ_2 is the corresponding Pauli matrix. Dark scalars, Dirac dark fermions and vectors are by Φ, Ψ and X, respectively. Vector currents operators in category VII are defined in eq. (6.2), and operators $\mathcal{O}^{(4)}_{{\rm dark}\,\mu\nu}$ in category VIII are given in eq. (6.3).

where ψ denotes any SM fermion, D the covariant derivative in the standard sector, and $\mathcal{D}$ the covariant derivative in the dark sector (replaced by an ordinary derivative if this sector is not gauged).

The $\mathcal{O}^{(4)}$ of categories V and VIII represent dimension 4 local operator combinations of the corresponding sector; the relevant ones for this work are:

$$\mathcal{O}^{(4)}_{{\rm dark}\,\mu\nu} \in \{\Phi^\dagger X_{\mu\nu}\Phi, \Phi\bar{\Psi}\sigma_{\mu\nu}P_{L,R}\Psi, \bar{\Psi}(\gamma_\mu \overleftrightarrow{\mathcal{D}}_\nu - \gamma_\nu \overleftrightarrow{\mathcal{D}}_\mu)P_{L,R}\Psi\}. \tag{6.3}$$

Renormalizability of the full theory – composed of mediators, dark and standard sectors – will be assumed. Within the neutral-mediator paradigm, the operators in table 6.1 are generated at tree level [2] by scalar mediators (categories II an V), fermion mediators (categories III and VI), vector mediators (category VII), or antisymmetric tensors representing spin-one mediators (categories IV and VIII) [98]. Here we will focus on operators with vector and antisymmetric tensor mediators because the models with scalar and fermion mediators have already been studied extensively [94, 97, 110, 129–137]. Our vector mediators do not correspond to dark photons [138, 139], which in the current scheme are members of the dark sector transforming non-trivially under $\mathcal{G}_{\rm DM}$, while the vector

[2] In category I, there is the Higgs-portal, $D = 4$ operator.

mediators considered here are singlets under this group.

The detailed UV completion of this effective field theory is beyond the scope of this thesis.

Our Lagrangian is conveniently split in two parts:

- Terms with dark fermions (Ψ):

$$\mathcal{L}_{\rm eff}^{\Psi} = \frac{\Upsilon_{\rm eff}}{\Lambda} B_{\mu\nu}\bar{\Psi}\sigma^{\mu\nu}\Psi + \frac{A_{\rm eff}^{L,R}}{\Lambda^2}\bar{\psi}\gamma_\mu\psi\bar{\Psi}\gamma^\mu P_{L,R}\Psi + \frac{\kappa_{\rm eff}^{L,R}}{\Lambda^2} B_{\mu\nu}\bar{\Psi}(\gamma^\mu \overleftrightarrow{\mathcal{D}}^\nu - \gamma^\nu \overleftrightarrow{\mathcal{D}}^\mu)P_{L,R}\Psi. \tag{6.4}$$

- Terms with dark bosons (X, Φ):

$$\mathcal{L}_{\rm eff}^{\Phi,X} = \frac{\zeta_{\rm eff}}{\Lambda} B_{\mu\nu}X^{\mu\nu}\Phi + \frac{\epsilon_{\rm eff}}{\Lambda^2}\bar{\psi}\gamma_\mu\psi\frac{1}{2i}\Phi^\dagger \overleftrightarrow{\mathcal{D}}^\mu\Phi. \tag{6.5}$$

In our calculations, the single operator dominance hypothesis is generally adopted, for example when computing $\Gamma_{Z\to\bar{\Psi}\Psi}$, we first take $\Upsilon_{\rm eff} \neq 0$ and $\kappa_{\rm eff}^{L,R} = 0$ and then the opposite. We comment on the combined effects of some operators in Sect. 6.6.

6.3 Invisible Z decay width

We focus on DM masses below m_Z, so the invisible Z decay width places important constraints on our EFT parameter space, related to operators in categories IV and VIII of table 6.1.

Ref. [140] improved the prediction of Bhabha scattering $e^+e^- \to e^+e^-$, resulting in a mild change of the number of light neutrino species – coming from LEP measurement of the hadronic cross section at the Z peak; the new value is $N_\nu = (2.9975 \pm 0.0074)$. Using these results, the experimental value of the invisible Z width becomes $\Gamma_Z^{\rm inv} = (501.03 \pm 1.27)$ MeV, including the standard decays to neutrino-antineutrino pairs and, possibly, decays to any other invisible final state. In the SM, the partial decay rate to a neutrino pair is $\Gamma(Z \to \bar{\nu}\nu) = (167.15 \pm 0.01)$ MeV [118]. With three light active neutrinos, this reads $\Gamma_Z^{\rm inv} - \Gamma_Z^{\bar{\nu}\nu} = (-0.42 \pm 1.30)$ MeV. Therefore, we will use [3]

$$\Gamma_Z^{\rm inv} - \Gamma_Z^{\bar{\nu}\nu} = 2.13 \text{ MeV at } 95\%\text{CL}. \tag{6.6}$$

[3] Using instead the value $\Gamma_Z^{\rm inv} = (499.0 \pm 1.5)$ MeV, from the PDG [118], we obtain $\Gamma_Z^{\rm inv} - \Gamma_Z^{\bar{\nu}\nu} = 0.49$ MeV at 95%CL.

6.3.1 Dark fermions

Using the operator $B_{\mu\nu}\bar{\Psi}\sigma^{\mu\nu}\Psi$ in eq. (6.4) to compute the $Z \to \bar{\Psi}\Psi$ matrix element, we get

$$\overline{|\mathcal{M}|^2} = \frac{8\Upsilon_{\text{eff}}^2 \sin^2\theta_W}{3\Lambda^2} m_Z^2(8m_\Psi^2 + m_Z^2), \tag{6.7}$$

that allows us to solve for the effective coupling over the NP scale Λ, as a function of the partial decay width:

$$\frac{\Upsilon_{\text{eff}}}{\Lambda} = \left\{ \frac{6\pi\Gamma_{Z\to\bar{\Psi}\Psi}}{\sin^2\theta_W(8m_\Psi^2 + m_Z^2)\sqrt{m_Z^2 - 4m_\Psi^2}} \right\}^{\frac{1}{2}}. \tag{6.8}$$

Using eq. (6.6) for $\Gamma_{Z\to\bar{\Psi}\Psi}$ and $m_Z = 91.1876(21)$ GeV [118], we plot in fig. 6.1 the region allowed by this constraint in the $m_\Psi - \Upsilon_{\text{eff}}/\Lambda$ plane (shaded blue area).

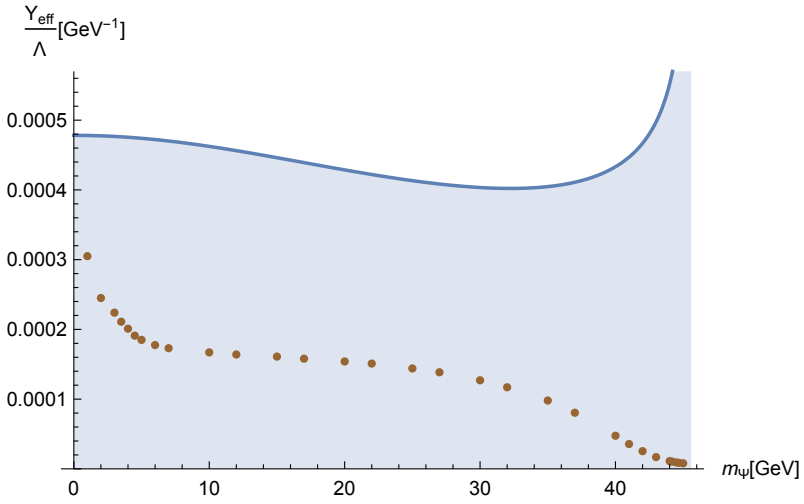

Figure 6.1: Effective coupling $\Upsilon_{\text{eff}}/\Lambda$ as a function of the dark fermion mass, compatible with the invisible decay width of the Z boson (blue area) and the observed relic density (brown dots)—see section 6.4 for further detail—.

Using the operator $B^{\mu\nu}\bar{\Psi}(\gamma_\mu \overleftrightarrow{\mathcal{D}}_\nu - \gamma_\nu \overleftrightarrow{\mathcal{D}}_\mu)P_{L,R}\Psi$ we obtain

$$\Gamma_{Z\to\bar{\Psi}\Psi} = \frac{\sin^2\theta_W m_Z^2\sqrt{m_Z^2 - 4m_\Psi^2}}{6\pi\Lambda^4}\left[m_Z^2\left\{(\kappa_{\text{eff}}^L)^2 + (\kappa_{\text{eff}}^R)^2\right\} - m_\Psi^2\left\{\left(\kappa_{\text{eff}}^L\right)^2 - 6\kappa_{\text{eff}}^L\kappa_{\text{eff}}^R + \left(\kappa_{\text{eff}}^R\right)^2\right\}\right]. \tag{6.9}$$

Taking $\kappa_{\text{eff}}^L = \kappa_{\text{eff}}^R$ to reduce the number of free parameters, yields

$$\frac{\kappa_{\text{eff}}^{L,R}}{\Lambda^2} = \left\{ \frac{3\pi\Gamma_{Z\to\bar{\Psi}\Psi}}{\sin^2\theta_W m_Z^2\sqrt{m_Z^2 - 4m_\Psi^2}(2m_\Psi^2 + m_Z^2)} \right\}^{\frac{1}{2}}, \tag{6.10}$$

from which we obtain the allowed shaded (pink) region in fig. 6.2.

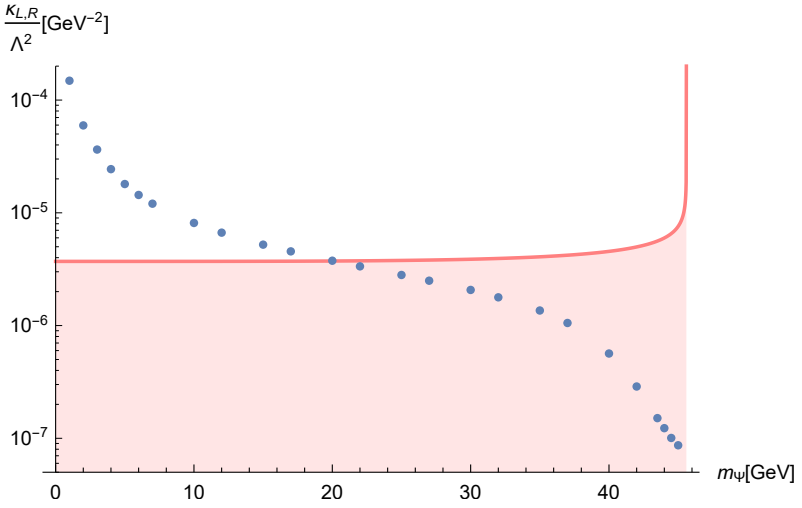

Figure 6.2: $\kappa_{\text{eff}}^{L,R}/\Lambda^2$ as a function of the dark fermion mass, compatible with the invisible decay width of the Z boson (pink area) and the observed relic density (blue dots)—see section 6.4 for further detail—.

Next we choose benchmark points for the effective operator coefficients and values of Λ. To motivate our choices consider, for example, the first term in eq. (6.4), generated at tree-level by the exchange of a heavy antisymmetric tensor field, and for which we estimate the scale Λ using fig. 6.1:

$$\frac{\Upsilon_{\text{eff}}}{\Lambda} \sim 4.4 \times 10^{-4}\text{GeV}^{-1}, \tag{6.11}$$

that in the fundamental theory would have the form [4]

$$\frac{\Upsilon_{\text{eff}}}{\Lambda} = \frac{g_1 g_2}{\Lambda} \tag{6.12}$$

where g_1, g_2 are the couplings in each vertex. We take the values of g_1, g_2 in the interval between that of the electron charge $g_{1,2} \sim 0.3$ and the weak coupling $g_{1,2} \sim 2/3$, as our educated guess. Using eq. (6.11) we then find[5]

$$230 \text{ GeV} < \Lambda < 1 \text{ TeV}. \tag{6.13}$$

We will be using these numbers as reference values, also when combining contributions of different operators, and checking if it is enough to work with the dimension 5 operators or if those of dimension 6 need to be included as well. The estimated values of Λ represent

[4] A $1/\Lambda^2$ dependence is expected from the propagator of the heavy mediator, with mass of order Λ. The coupling of the mediator to the B has a coefficient with dimensions of mass, which we assume to be $g_2\Lambda$.

[5] Using the numbers in footnote 3 we get instead $\Lambda \in [0.5, 2.2]$ TeV.

the largest energy scale up to which our EFT can possibly be used. Since the relevant scale for the processes that we consider is $E \lesssim m_Z$, the ratio E/Λ is small enough to neglect operators of dimension ≥ 7.

6.3.2 Dark Vector and Dark Scalar

Using the operator $B_{\mu\nu}X^{\mu\nu}\Phi$ (category IV) in eq. (6.5), we compute $Z \to X\Phi$, and obtain

$$|\mathcal{M}|^2 = \frac{4\zeta_{\text{eff}}^2 \sin^2\theta_W}{3M_\Omega^2}\left\{\frac{1}{2}(m_Z^2 - m_\Phi^2 + m_X^2)^2 + m_X^2 m_Z^2\right\}, \tag{6.14}$$

and the decay rate

$$\Gamma = \frac{\zeta_{\text{eff}}^2 \sin^2\theta_W}{12\pi m_Z^3 \Lambda^2}\lambda^{\frac{1}{2}}(m_Z^2, m_\Phi^2, m_X^2)\left\{\frac{1}{2}(m_Z^2 - m_\Phi^2 + m_X^2)^2 + m_X^2 m_Z^2\right\}, \tag{6.15}$$

where $\lambda(a,b,c) = a^2 + b^2 + c^2 - 2ab - 2bc - 2ca$. Whence

$$\frac{\zeta_{\text{eff}}}{\Lambda} = \left\{\frac{12\pi m_Z^3 \Gamma_{Z\to X\Phi}}{\sin^2\theta_W \lambda^{\frac{1}{2}}(m_Z^2, m_\Phi^2, m_X^2)\left[\frac{1}{2}(m_Z^2 - m_\Phi^2 + m_X^2) + m_X^2 m_Z^2\right]}\right\}^{\frac{1}{2}}. \tag{6.16}$$

As we did before, we use eq. (6.6) to constrain the ratio $\zeta_{\text{eff}}/\Lambda$.

The above expression is a function of the masses of the vector and the scalar dark particles, but we will explain later that the only interesting values are those when $m_\Phi \sim m_X$. In this case, we obtain the allowed pink region in fig. 6.3.

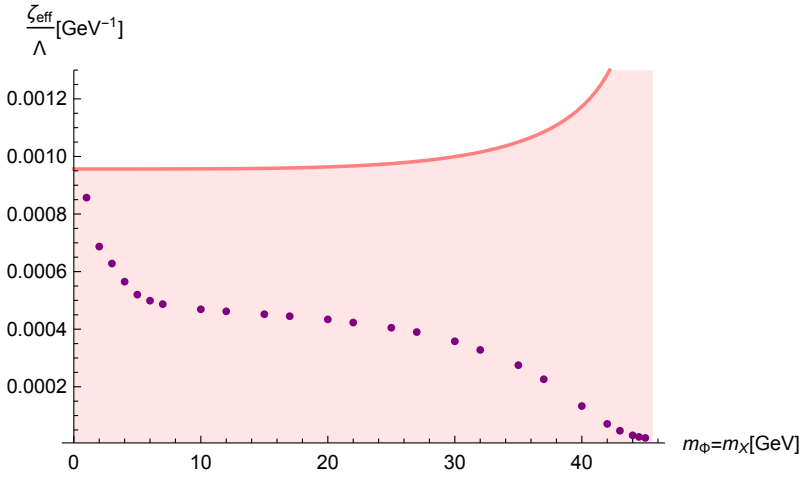

Figure 6.3: Effective coupling $\zeta_{\text{eff}}/\Lambda$ as a function of the dark particles mass, compatible with the invisible decay rate of the Z boson (pink area) and the observed relic density (violet dots)—see section 6.4 for further detail—.

6.4 Relic Density

MicrOMEGAs code [141] is used to calculate the relic abundance of dark matter, within our EFT. One operator at a time is used, and the coefficient [6] in the Lagrangian — in eqs. (6.4) and (6.5) — is obtained to reproduce the measured relic density [142]

$$\Omega_{\rm DM} h^2 = 0.1193 \pm 0.0009. \tag{6.17}$$

6.4.1 Dark fermions

Proceeding as described above, and considering only the dimension 5 operator $\propto \Upsilon_{\rm eff}$ in eq. (6.4), we get the dots in fig. 6.1. We can see that we have solutions compatible with both observations in all the mass range we are analyzing. If we now use the operator with two fermionic currents, $\mathcal{J}_{\rm SM}^{(\psi)\mu}\mathcal{J}_{\rm dark\ \mu}^{(L,R)}$ (category VII), we obtain the dots in fig. 6.4, where we assume $A_{\rm eff}^L = A_{\rm eff}^R$. Finally, the computation of the relic density considering the operator with derivative couplings $\propto \kappa_{\rm eff}^{L,R}$ in eq. (6.4) (category VIII) generates the dots in fig. 6.2, where we take $\kappa_{\rm eff}^L = \kappa_{\rm eff}^R$. In this case, we find solutions when $m_\Psi \gtrsim 20$ GeV. The case where we have both a dark scalar and a dark vector is discussed in the next subsection.

The couplings of the operators not contributing to the invisible decay of the Z can be estimated as in eq. (6.12)

	$g_{1,2} \sim e$, $\Lambda \sim 1$TeV	$g_{1,2} \sim 0.66$, $\Lambda \sim 230$GeV
$g_1 g_2/\Lambda^2\,({\rm GeV}^{-2})$	$\sim 1.1 \times 10^{-7}$	8.4×10^{-6}

(6.18)

The values $A_{\rm eff}^{L,R}$ consistent with the above estimates can be obtained from fig. 6.4, where the constant value showed by the blue line corresponds to the least restrictive condition in eq. (6.18) and we observe that there are acceptable solutions when the fermion mass $m_\Psi \gtrsim 4$ GeV; we note that this corresponds to a "small" scale Λ and/or "large" couplings $g_{1,2}$.

6.4.2 Dark Vector and Dark Scalar

Turning next to the effects of the category IV operator of dimension 5, $\propto \zeta_{\rm eff}$ in eq. (6.5), we obtain the dots in fig. 6.3 where we use $m_X = m_\Phi$; in this case we find suitable solutions for the full range of masses that we are considering. In contrast, when m_X and m_Φ differ

[6] The uncertainty in eq. (6.17) is small, so this restriction determines the operator coefficient for each choice of the DM candidate(s) mass(es).

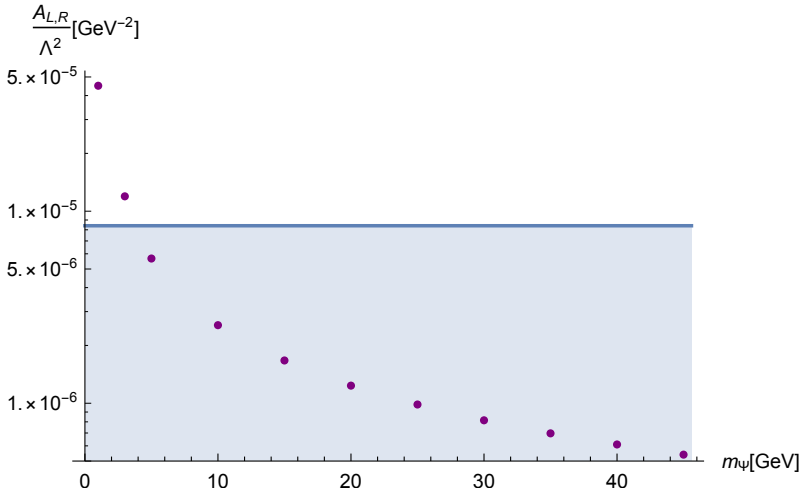

Figure 6.4: Effective coupling $\frac{A_{\rm eff}^{L,R}}{\Lambda^2}$ as a function of the dark fermion mass, compatible with the observed relic density (purple dots) and compared to a reference value, eq. (6.18), shown by the blue line.

by a few GeV or more, the model does not fit the constraints. This happens because, when $m_X \sim m_\Phi$, the dominant process regulating the relic abundance is $X\Phi \to \bar{f}f$ via an s-channel B exchange; the cross section and invisible width are then $\propto 1/\Lambda^4$. In contrast, when $m_X > m_\Phi$ ($m_\Phi > m_X$) the dominant process is $\Phi\Phi \to \gamma\gamma$ ($XX \to \gamma\gamma$) via a t-channel X (Φ) exchange, which is quadratic in the effective vertex, giving an annihilation cross section $\propto 1/\Lambda^8$ (the invisible width is still $\propto 1/\Lambda^4$), relic abundance constraint then requires a value of Λ too small to be consistent with the Z width.

6.4.3 Dark Scalar

In this case the relevant operator (proportional to $\epsilon_{\rm eff}$ in eq. (6.5)) is composed of a standard fermionic current and a dark scalar current. Using this we obtain the dots in fig. 6.5, where the horizontal line corresponds to the weaker estimate in eq. (6.18). Combining these results we find that only masses $m_\Phi \gtrsim 36$ GeV are consistent with the benchmark range in eq. (6.18) .

6.4.4 Other operators

The remaining operators generated by spin one mediators differ from the ones treated so far in the number of dark particles in the effective vertex. In category VIII we have $B^{\mu\nu}\Phi^\dagger X_{\mu\nu}\Phi$, which contains 3 dark particles. In this case the invisible Z width constraint is easily met because of the 3-body final state phase space suppression. The relic abundance (for $m_\Phi \sim m_X$) is controlled by processes such as $\Phi\Phi \to X\psi\bar{\psi}$ and $\Phi X \to \Phi\psi\bar{\psi}$

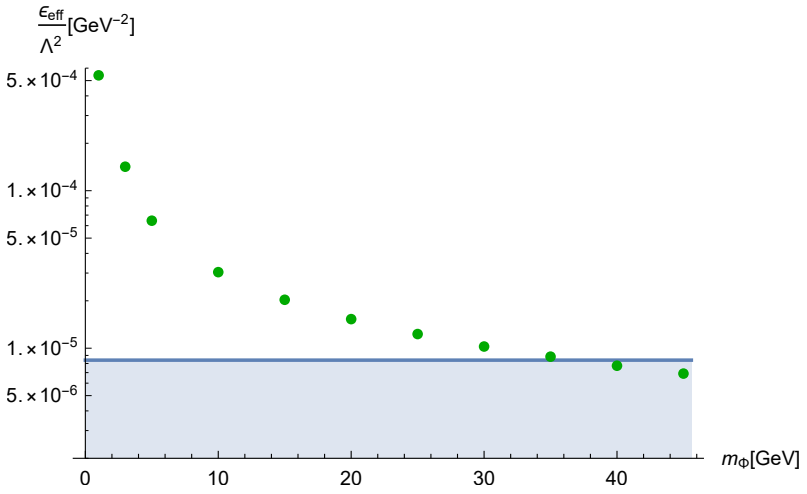

Figure 6.5: Effective coupling $\frac{\epsilon_{\text{eff}}}{\Lambda^2}$ as a function of the dark scalar mass, compatible with the observed relic density (green dots) and compared to the reference value eq. (6.18), shown by the blue line.

with a virtual B coupling to the standard fermions ψ; these rates are also phase-space suppressed requiring an unreasonable small Λ in order to meet the experimental observations. The same issue arises with operator $B^{\mu\nu}\Phi\bar{\Psi}\sigma_{\mu\nu}P_{L,R}\Psi$. This situation is not a problem because, given a specific choice of DM particle(s), these dimension 6 operators play a subdominant role (see the discussion at the end of subsection 6.3.1). Inspection of figs. 6.4 and 6.5 reveals that suitable solutions can only be obtained for the largest $\Lambda \sim 1$ TeV. Because of this, we will neglect these subleading operators in our subsequent analysis.[7]

6.5 Observational limits

In this section we discuss limits derived from several direct and indirect detection constraints; we will use the following notation:

$$\begin{aligned}
&\text{OP1} \equiv B_{\mu\nu}\bar{\Psi}\sigma^{\mu\nu}\Psi,\\
&\text{OP2} \equiv \bar{\psi}\gamma^{\mu}\psi\bar{\Psi}\gamma_{\mu}P_{L,R}\Psi,\\
&\text{OP3} \equiv B_{\mu\nu}\bar{\Psi}(\gamma^{\mu}\overleftrightarrow{\mathcal{D}}^{\nu} - \gamma^{\nu}\overleftrightarrow{\mathcal{D}}^{\mu})P_{L,R}\Psi,\\
&\text{OP4} \equiv B_{\mu\nu}X^{\mu\nu}\Phi,\\
&\text{OP5} \equiv \frac{1}{2i}\left(\bar{\psi}\gamma^{\mu}\psi\right)\left(\Phi^{\dagger}\overleftrightarrow{\partial}_{\mu}\Phi\right).
\end{aligned} \tag{6.19}$$

[7] Available freeware such as micrOMEGAs often assume a discrete symmetry within the dark sector to ensure DM stability. This excludes these dimension 6 operators, and makes it difficult to calculate their effects in detail.

In the calculations below we will use the effective couplings that correctly reproduce the relic density, eq. (6.17), as shown in the figures of sections 6.3 and 6.4. For the case of OP4 we only consider the scenario where $m_X = m_\Phi$, as discussed in subsection 6.4.2. We also consider the combined contributions from dimension 5 and 6 operators when they contain the same DM candidate; in such cases we adopt the following relationship between the scales Λ and operator coefficients C:

$$\Lambda_{\text{dim }6} = \Lambda_{\text{dim }5}\,, \qquad C_{\text{dim6}} = \pm C_{\text{dim5}}. \tag{6.20}$$

In these cases we find that the effects of the sign are negligible. We will again use the two previously estimated values for Λ, in eq. (6.13), as benchmark points. However, since the value of Λ has a greater impact in the subdominant operator, we find that its effects are also negligible.

6.5.1 Direct Detection Experiments

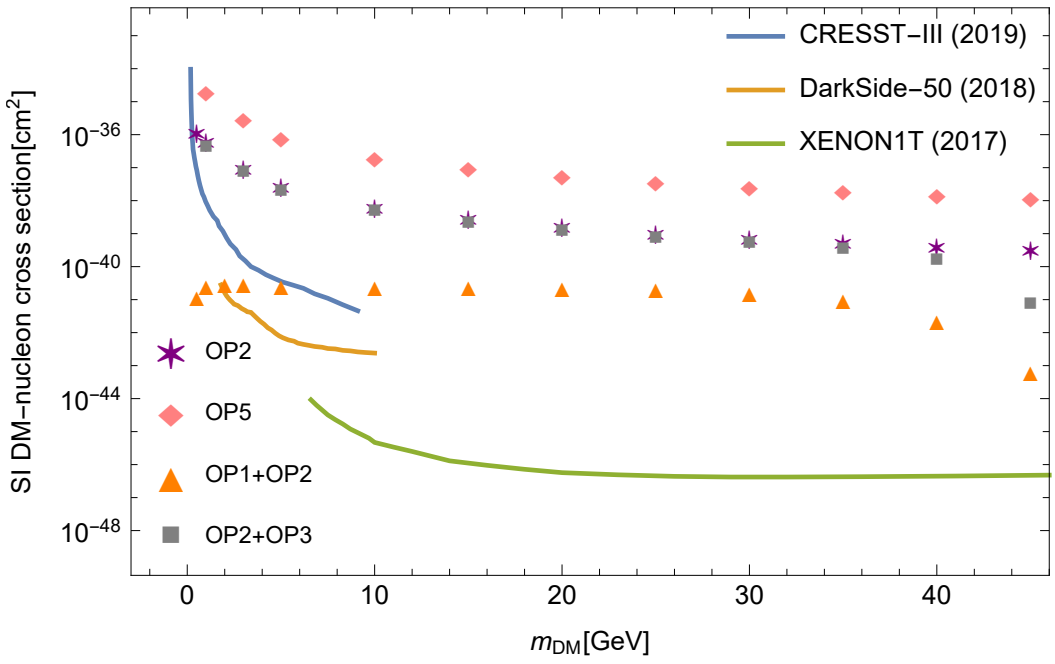

Figure 6.6: WIMP cross sections (normalized to a single nucleon) for spin-independent coupling versus mass. OP1, OP2, OP3 and OP5 are defined in eq. (6.19). When we combine operators, we use $\Lambda = 1$ TeV. Operators not shown here have cross sections many orders of magnitude below the current limits.

Currently the most stringent limit on spin-independent scattering cross sections of DM-nucleon particles come from the LUX-ZEPLIN, DarkSide-50 and CRESST-III experiments. In order to derive the implications for the effective theory under study we

obtained the DM-nucleon cross sections in the limit where the relative velocity goes to zero. We use micrOMEGAs [141] to compute it.

Fig. 6.6 shows the values for the DM-nucleon scattering cross sections already excluded by the DarkSide-50 [143], XENON1T [119] and CRESST-III [123] experiments [8], as well as the results that we obtained for different operators. The notation used in this figure is defined in eq. (6.19).

We can see that the operators included in fig. 6.6 are ruled out in the mass range we are considering, with the exception of a small region of very light masses. Operators not shown in fig. 6.6 – OP1, OP3, OP1+OP3 and OP4 – have DM-nucleon cross sections many orders of magnitude below the current limits from direct detection experiments. Therefore, in the following, we will only consider those operators not shown in fig. 6.6.

6.5.2 Dwarf spheroidal satellite galaxies

The dwarf spheroidal satellite galaxies (dSphs) of the Milky Way are some of the most DM dominated objects known. Due to their proximity, high DM content, and apparent absence of non-thermal processes, dSphs are excellent targets for the indirect detection of DM. Recently, eight new dSph candidates were discovered using the first year of data from the Dark Energy Survey (DES). Ref. [124] searched for gamma-ray emission coincident with the positions of these new objects in six years of Fermi Large Area Telescope data. No significant excesses of gamma-ray emission were found. Individual and combined limits on the velocity-averaged DM annihilation cross section for these new targets —assuming that the DES candidates are dSphs with DM halo properties similar to the known dSphs— were also computed, as we can see in fig. 6.7.

We computed the non-relativistic ($m_{\rm DM} \ll T$) thermally-averaged DM annihilation cross sections $\langle \sigma v \rangle$, using our effective operators OP1,3,4, and compared the results with the limits mentioned before. The results are presented in fig. 6.8, where we can see that DM masses in the intermediate region 10 GeV $\lesssim m_{\rm DM} \lesssim$ 45 GeV are allowed.

6.5.3 Limits from AMS-02 positron measurements

The AMS-02 Collaboration has presented high-quality measurements of positron fluxes as well as the positron fraction. Working under the well-motivated assumption that a background positron flux exists from spallations of cosmic rays with the interstellar medium and from astrophysical sources, ref. [125] used measurements of the positron flux

[8] The limits from LUX-ZEPLIN were published after our paper [144], for that reason in fig. 6.6, XENON1T data appeared instead of LUX-ZEPLIN. However the conclusions of our work do not change, since the operators shown in the figure were already excluded by the XENON1T data and the operators not shown in the figure have cross sections even smaller than the current limits from LUX-ZEPLIN.

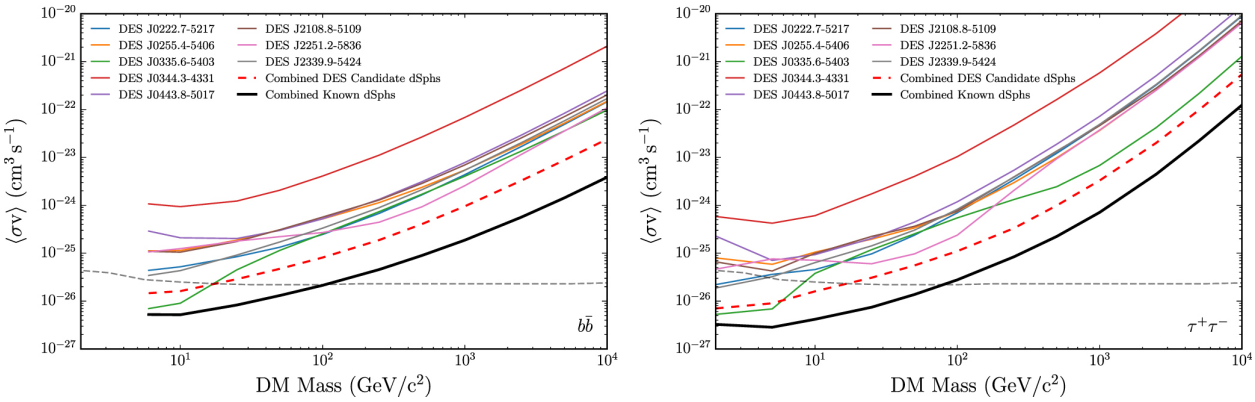

Figure 6.7: Upper limits on the velocity-averaged DM annihilation cross section at 95%CL for DM annihilation to $\bar{b}b$(left) and $\tau^+\tau^-$(right). The current best limits derived from a joint analysis of 15 previously known dSphs are also shown (black curve). For reference, we also display (dashed gray curve) the thermal relic cross section derived by Steigman et al. [145].

to derive limits on the dark matter annihilation cross section and lifetime for various final states (see also ref. [146]), and extracted strong limits on DM properties. Specifically, for DM particles annihilating only into e^+e^- or into $\mu^+\mu^-$, their bounds on the annihilation cross section are stronger than the thermal value when the dark mass is in the range that we are considering. These limits are shown in fig. 6.9, where the solid lines correspond to the best limits sampling over all energy windows, while those shown with dashed lines were derived selecting windows containing only energies larger than 10 GeV. The latter limits are only mildly affected by the modeling of the solar modulation and are therefore more robust, so we will use them in the calculations below.

The comparison of the limits derived using the annihilation cross sections into e^+e^- and $\mu^+\mu^-$ final states and those computed with our effective operators are shown in fig. 6.10. We see in fig. 6.10(b) that only DM masses in $\sim [33, 44]$ GeV remain as suitable solutions. Ref. [125] also derived limits for the final states $\tau^+\tau^-$, $\bar{b}b$, but these are weaker than those using the dSphs data.

6.6 Discussion and conclusions

From the various limits obtained in the sections above, we derive the following restrictions on the operators listed in eq. (6.19) (items 1-5 below refer to OP1-5, respectively). The discussion below refers only to values for the effective coupling coefficients that correctly reproduce the relic density in eq. (6.17). A summary of our results[9] is given in table 6.2.

1. We obtain a negligible direct detection cross sections when we use the operator

[9]DM masses below 2 GeV are allowed for OP1 and OP4 because the updated value of $\Gamma_Z^{\rm inv} - \Gamma_Z^{\bar{\nu}\nu}$ used in sect. 6.3. The previous result (footnote 3) excluded these regions of parameter space.

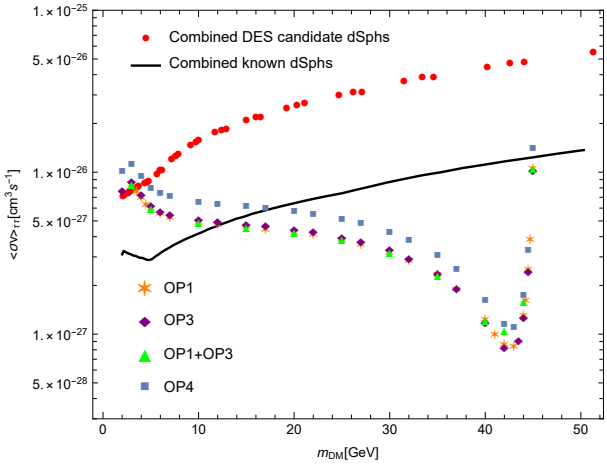

(a) Annihilation into $\tau^+\tau^-$

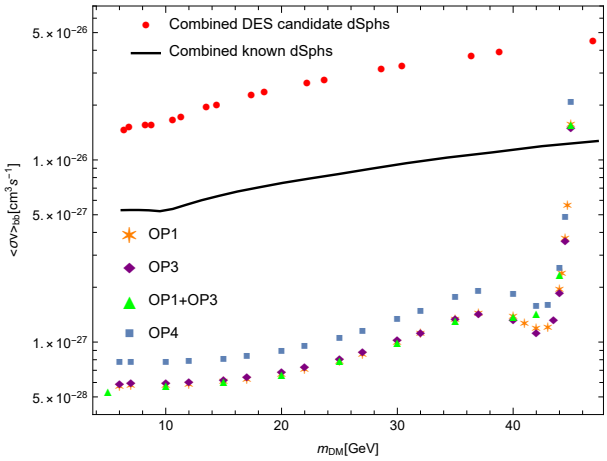

(b) Annihilation into $\bar{b}b$

Figure 6.8: Restrictions from dSphs on the DM annihilation cross sections into (a) $\tau^+\tau^-$ and (b) $\bar{b}b$ for the portals generated by several operators, defined in eq. (6.19).

$B_{\mu\nu}\bar{\Psi}\sigma^{\mu\nu}\Psi$ (OP1), many orders of magnitude below the bounds from current or future direct detection experiments. The strongest constraint on this operator comes from thermally-averaged DM annihilation cross section into e^+e^- (as we can see in fig. 6.10(b)) that only allows masses in the range $\approx 33 - 44.5$ GeV.

2. If we take the operator involving *fermionic* currents in both sectors in the operator $\mathcal{J}^{\mu}_{\rm SM}\mathcal{J}_{{\rm dark}\,\mu}$ (OP2), we get values for the DM-nucleon cross sections that are already excluded by direct detection experiments (*cf.* fig. 6.6). Therefore, we can rule out this operator for the mass range that we are considering.

3. When we use the operator $B_{\mu\nu}\bar{\Psi}(\gamma^{\mu}\overleftrightarrow{\mathcal{D}}^{\nu} - \gamma^{\nu}\overleftrightarrow{\mathcal{D}}^{\mu})P_{L,R}\Psi$ (OP3), we again get a negligible direct detection cross section. The thermally-averaged DM annihilation cross section into e^+e^- shown in fig. 6.10(b) excludes masses $\lesssim 33$ GeV and $\sim m_Z/2$.

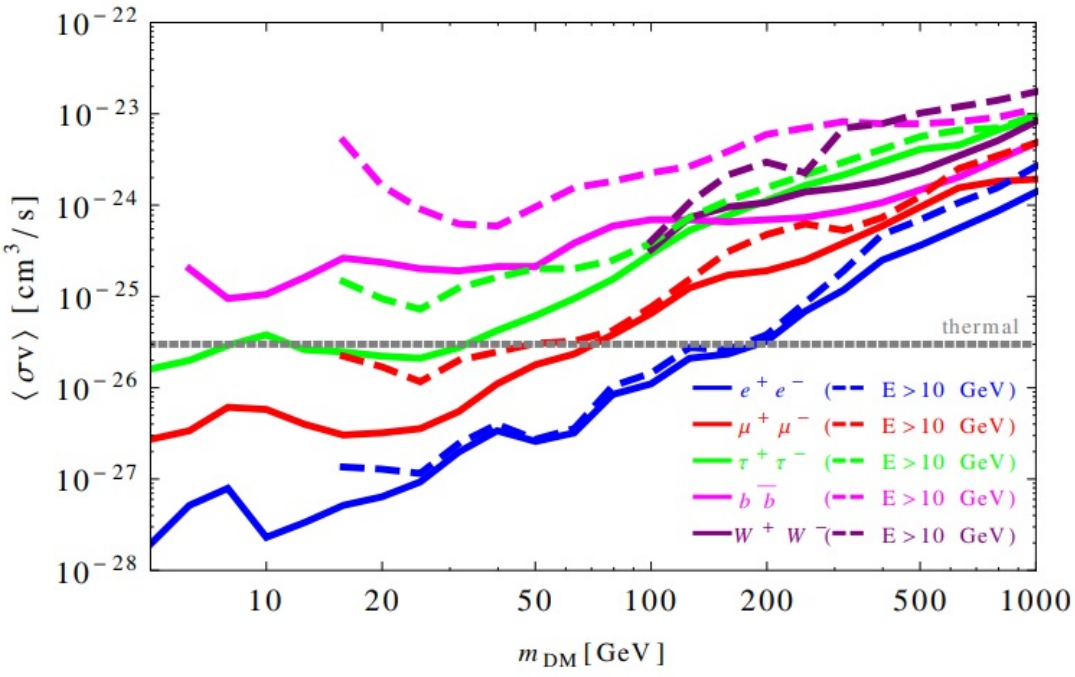

Figure 6.9: Limits on the annihilation cross section derived from the AMS-02 data on the positron fraction, assuming the MED propagation model [147]. The limits shown as solid lines were derived from sampling over various energy windows, while the dashed lines are from considering those windows including only data with energies above 10 GeV.

4. For the operator $B_{\mu\nu}X^{\mu\nu}\Phi$ (OP4), the case $m_X \nsim m_\Phi$ is excluded by the relic abundance constraint for all values in our mass range. When $m_\Phi \simeq m_X$ the limits from direct DM detection searches are again irrelevant, but the thermally-averaged DM annihilation cross section into e^+e^- excludes masses $\lesssim 36$ GeV and $\sim m_Z/2$ —fig. 6.10(b)—.

5. For the operator $\mathcal{J}^\mu_{\rm SM}\mathcal{J}_{{\rm dark}\,\mu}$, with scalar dark current and fermionic SM current, (OP5), the direct detection cross sections in the mass range we consider are excluded by the current data, as show in fig. 6.6.

6. When we include operators OP1 and OP2 simultaneously (using the prescription of eq. (6.20)), the limits from DarkSide and XENON1T exclude masses above ≈ 2 GeV [10].

7. Combining operators OP1 and OP3 (using eq. (6.20)), we get negligible DM-nucleon cross sections. The strongest bounds come from the thermally-averaged DM anni-

[10]The invisible Z decay width bound eq. (6.6) is respected for DM masses as low as ~ 2.5 MeV for the dimension five operator, and the value of the corresponding dimensionless effective coupling still satisfies eq. (6.18) and complies with the limits below ~ 0.2 GeV derived in ref. [148].

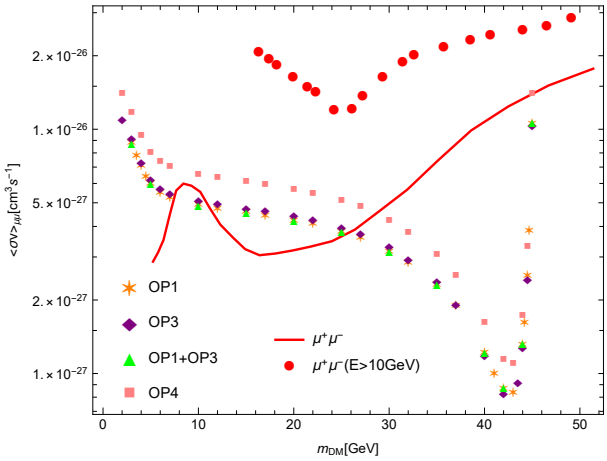

(a) Annihilation into e^+e^-

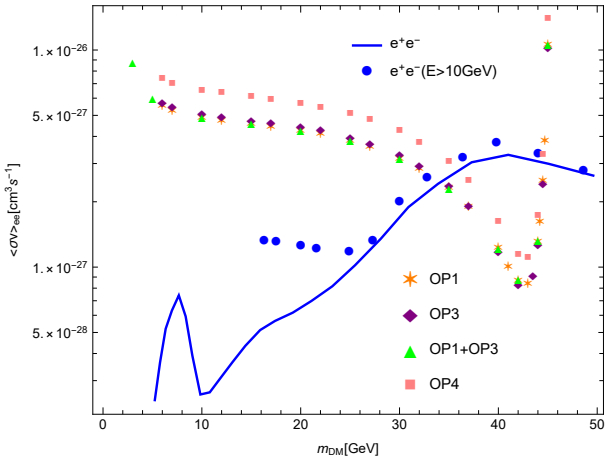

(b) Annihilation into $\mu^+\mu^-$

Figure 6.10: Restrictions from AMS-02 data on the DM annihilation cross sections into (a) e^+e^- and (b) $\mu^+\mu^-$ for the portals generated by several operators, defined in eq. (6.19).

hilation cross section into e^+e^- —fig 6.10(b)—, that excludes masses $\lesssim 33$ GeV and $\sim m_Z/2$.

8. Finally, we also explored the possibility of having operators OP2 and OP3. In that case, all parameter space is forbidden by the results from direct detection experiments.

There are stringent limits on light dark particles from the ATLAS experiment [149]; however, we did not use those results because they are highly model-dependent.

We see then that the combination of direct detection experiments and the constraints from relic density, rule out the operators of category VII in table 6.1. In contrast, we found that all dimension 5 operator portals in category IV are compatible with the experimental

Operator	**Dim.**	**DM candidate**	**Allowed mass (GeV)**
1.- $B_{\mu\nu}\bar{\Psi}\sigma^{\mu\nu}\Psi$	5	Ψ fermion	$\approx 0.0025-2, \approx 33-44.5$
2.- $\left(\bar{\psi}\gamma_\mu\psi\right)\left(\bar{\Psi}\gamma^\mu P_{L,R}\Psi\right)$	6	Ψ fermion	none
3.- $B_{\mu\nu}\bar{\Psi}(\gamma^\mu \overleftrightarrow{\mathcal{D}}^\nu - \gamma^\nu \overleftrightarrow{\mathcal{D}}^\mu)P_{L,R}\Psi$	6	Ψ fermion	$\approx 33-44.5$
4.- $B_{\mu\nu}X^{\mu\nu}\Phi$	5	vector X, scalar Φ	$\approx 0.11-2, \approx 36-44.5$
5.- $\left(\bar{\psi}\gamma_\mu\psi\right)\ \frac{1}{2i}\Phi^\dagger \overleftrightarrow{\mathcal{D}}^\mu\Phi$	6	scalar Φ	none
$1+2$	5+6	Ψ fermion	$\approx 0.0025-2$
$1+3$	5+6	Ψ fermion	$\approx 0.0025-2, \approx 33-44.5$
$2+3$	6	Ψ fermion	none

Table 6.2: Summary of results obtained considering the Z invisible decay width, relic density, direct detection experiments and indirect detection results from dSphs and positron flux measurements. It is very important to note that we are considering masses of the dark particles below the mass of the Z boson ($m_Z/2 \sim 45.5$ GeV, as they appear in charge conjugated pairs).

constraints —invisible decay width of the Z boson, DM relic density[11], direct detection experiments, and indirect limits coming from dSphs and positron flux measurements— for DM masses lighter than $m_Z/2$ and larger than ~ 33 GeV. For the allowed operator portals, the most stringent limits come from the thermally averaged DM annihilation cross section into e^+e^- as shown in fig. 6.10(b). Besides, we can see that these operators have an allowed region for masses between some MeV and 2 GeV, where the upper limit comes from the DM annihilation cross sections into $\tau^+\tau^-$ —*cf.* fig. 6.8(a)—, while the lower limits are due to the Z invisible decay width. As we mentioned before, when we combine OP1+OP2 and OP1+OP3, the value of Λ has a negligible effect, since OP1 completely dominates the interaction.

We also considered the combination of OP4 and OP5, as they share the dark scalar as DM candidate. Using again the relationships of eq. (6.20), we find, as in other scenarios, that the lower-dimension operator(OP4) dominates; accordingly, the constraints can be met only when $m_X \sim m_\Phi$, as discussed in subsection 6.4.2. In addition, the bound from the Z invisible width excludes masses below ~ 4 GeV and data from direct detection experiments exclude masses above ~ 3 GeV. We then find that this combination of OP4

[11]We recall the fact that we are considering the WIMP freeze-out scenario when computing the DM relic density.

and OP5 is disallowed in the mass range that we analyze. Other combinations of operators correspond to multi-component dark matter scenarios and involve a larger number of unknown parameters. We do not address these possibilities as they are difficult to discuss systematically and because the results depend strongly on any simplifying assumptions.

The results in table 6.2 look promising and warrant further exploration of the anti-symmetric tensor, spin-1 mediator portal with mass below m_Z that, together with the better-studied Higgs, fermion and vector portals may help unravel the DM puzzle, unsolved since 1933.

Chapter 7

Exploring a wider mass range for DM masses

7.1 Overview

In this chapter, based on ref. [150], we continue using the EFT framework of chapter 6 and we start by exploring a wider mass range, from 50 GeV up to 6.4 TeV. We use again bounds from different experiments: relic density, direct detection experiments and indirect detection limits from the search of gamma-ray emissions and positron fluxes. Besides, in this chapter we add collider constraints by the ATLAS detector [151] in monojet analysis. Moreover, here we tested our previous results in table 6.2 in the light of the aforementioned ATLAS data. The collider constraints turn out to be the most restrictive together with the bounds from direct detection experiments.

The chapter is organised as follows: In section 7.2 we analyze several observational limits: in subsection 7.2.1 we check that the observed relic abundance can be reproduced in the different cases, in subsection 7.2.2 we verify the direct detection bounds are respected; and in subsections 7.2.3 and 7.2.4 we consider the indirect bounds given by dwarf spheroidal satellite galaxies and the positron flux, respectively. After that, in section 7.3 we include the collider constraints by the ATLAS collaboration; finally the discussion and conclusions are presented in section 7.4.

7.2 Observational limits

7.2.1 Relic density

As we did before in section 6.4, we use micrOMEGAs code [141] to compute the relic abundance of dark matter with operators in the Lagrangian in eqs. (6.4) and (6.5). We

use the single operator hypothesis, and we obtain the effective coefficients that correctly reproduce the observed relic density [1] [152]

$$\Omega_{\rm DM}h^2 = 0.1200 \pm 0.0012\,. \tag{7.1}$$

We keep using the notation in eq. (6.19) for our operators.

In the calculations below, we will use the effective couplings that correctly reproduce the relic density, eq. (7.1). We again consider the combined contributions from dimension 5 and 6 operators when they contain the same DM candidate; in such cases we adopt the relationships in eq. (6.20) between the scales Λ and operator coefficients C.

In most combinations, the relative sign between coefficients is irrelevant, with the exception of the combination between OP1 and OP3, where the effective couplings are different depending on the sign between them.

We are using $\Lambda = 2\,m_{\rm DM}$ when combining operators of different dimensions [2] [3]. We consider that equality a safe limit for the convergence of the effective theory, as discussed in [134]. Also in [154], the authors use the same relationship for their calculations to be meaningful in the EFT framework. Depending on the UV completion of the theory, a possible s-channel process in the high-energy theory might break the EFT when the corresponding heavy mediator resonates. We have checked that our results change insignificantly moving slightly away from the previous equality ($\Lambda \gtrsim 2m_{\rm DM}$). Hereafter, we will be expressing constraints on ratios of effective couplings over $\Lambda^{(2)}$ as bounds on the couplings by using $\Lambda = 2\,m_{\rm DM}$, for given DM masses.
When combining operators, sticking to the case $\Lambda = 2m_{\rm DM}$ maximizes the impact of higher-dimensional operators, through their interference with the leading ones, while keeping the convergence of the EFT. Of course solutions can be found for $\Lambda > 2m_{\rm DM}$. Indeed, as $\Lambda/m_{\rm DM}$ increases, the subleading operators become eventually negligible and the results from the single operators of leading dimension are recovered.

[1] The number in (eq. (7.1)) is the updated value for the relic density in (eq. (6.17)). We include both numbers because we used them in different years during the development of this thesis.

[2] Although all operators that we consider in this work can, in principle, be generated at tree level by spin-one mediators neutral under both SM and DM gauge groups [153], a caveat is in order. If the dimension 5 operators are generated at loop level, the ratio $m_{\rm DM}/\Lambda$ could be a few orders of magnitude smaller. This would depend on the hierarchy between $m_{\rm DM}$ and $m_{\rm loop}$ (the mass of the inner particle in the loop, not necessarily the mediator or the DM particle), and that is completely model dependent.

[3] A comment on the operator coefficients is pertinent: depending on the working assumptions (neutral or charged mediators under SM and DM gauge groups, mediators' spin, etc.) a given operator can be generated at tree level or first appears at one loop (see section 2.1. of [153]). If the underlying physics is weakly coupled, the coefficient is suppressed by $\sim 1/(16\pi^2)$, which may require an unnaturally large dimensionless coupling value, that -on the contrary- would be expected if the underlying physics is strongly coupled.

7.2.2 Direct Detection Experiments

As we mentioned before, the most stringent limits on spin-independent scattering cross sections of DM-nucleon particles come from the LUX-ZEPLIN experiment [155]. However, we also include limits from the PANDA-4T [156] and XENON1T experiments. Again we use micrOMEGAs [141] to compute the DM-nucleon cross sections in our EFT in the limit where the relative velocity goes to zero. In fig. 7.1 we show the results that we obtained for several operators in our EFT and compare them with the limits from experiments. The notation used in this figure is defined in eq. (6.19). We can see that OP2, OP5 and the combination of OP4 and OP5 are completely ruled out by these experiments. Operators not shown in fig. 7.1 have DM-nucleon cross sections many orders of magnitude below the current experimental limits from direct detection experiments. Therefore, in the following we will only consider those operators not shown in fig. 7.1 —OP1, OP3, OP4 and OP1±OP3—.

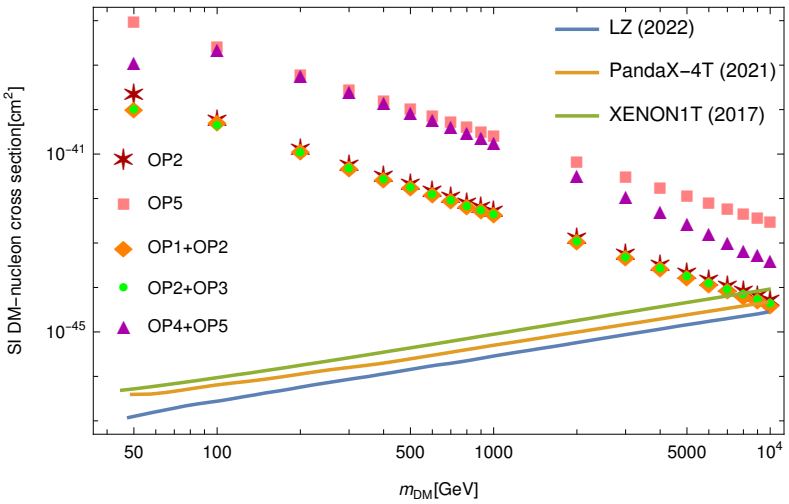

Figure 7.1: WIMP cross sections (normalized to a single nucleon) for spin-independent coupling versus mass. The notation in this figure is defined in eq. (6.19). When we combine operators, we use $\Lambda = 2m_{\rm DM}$. Operators not shown here have cross sections many orders of magnitude below the current limits.

7.2.3 Dwarf spheroidal satellite galaxies

For a description of the data we use from dwarf spheroidal satellite galaxies, see subsection 6.5.2. With micrOMEGAs we computed the non-relativistic ($m_{\rm DM} \ll T$) thermally-averaged DM annihilation cross sections $\langle \sigma v \rangle$, using our effective operators —those that are not ruled out by direct detection experiments, see fig. 7.1—, and compared the results with the limits shown in figure 6.7. The results are presented in figure 7.2, and we can see

that these limits do not help us to constrain our mass region. Note that the combination of operators OP1 and OP3 has a relative sign between its coefficients, the one with the same sign gives velocity-averaged cross sections even below those shown in this figure.

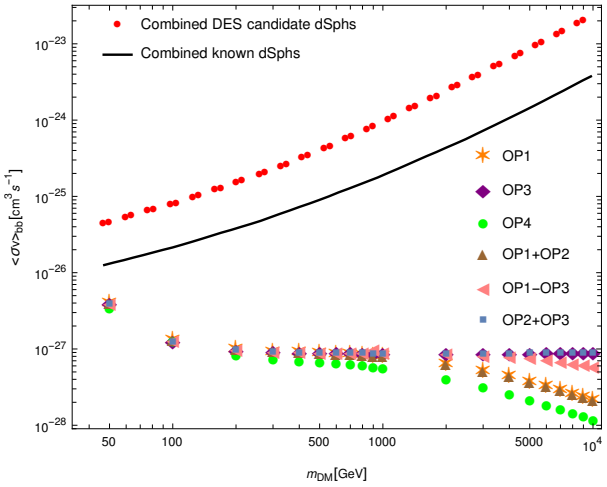

(a) Annihilation into $b\bar{b}$

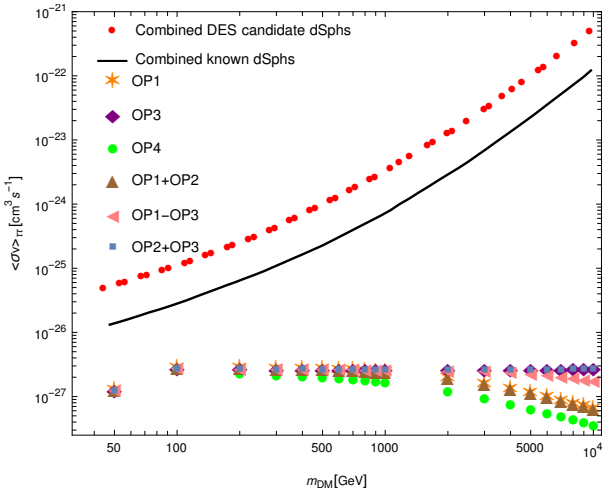

(b) Annihilation into $\tau^+\tau^-$

Figure 7.2: Restrictions from dSphs on the DM annihilation cross sections into (a) $b\bar{b}$, (b) $\tau^+\tau^-$ for the portals generated by several operators, defined in eq. (6.19). We see in both panels that the entire mass region is allowed by the data.

7.2.4 Limits from AMS-02 positron measurements

The description of the limits we use from the measurements of the AMS-02 Collaboration of the positron fluxes and the positron fraction is in subsection 6.5.3. We again computed the DM annihilation cross sections, now into e^+e^- and $\mu^+\mu^-$, using micrOMEGAs and compare them with the bounds derived in Ref. [125], shown in fig. 6.9. In figure 7.3 we

see that our results are below the experimental limits and we cannot rule out any mass region. Note that in this figures we again show the combinations of OP1 and OP3 with a relative sign between their coefficients, because their combination with the same sign gives even smaller values for the velocity-averaged cross sections.

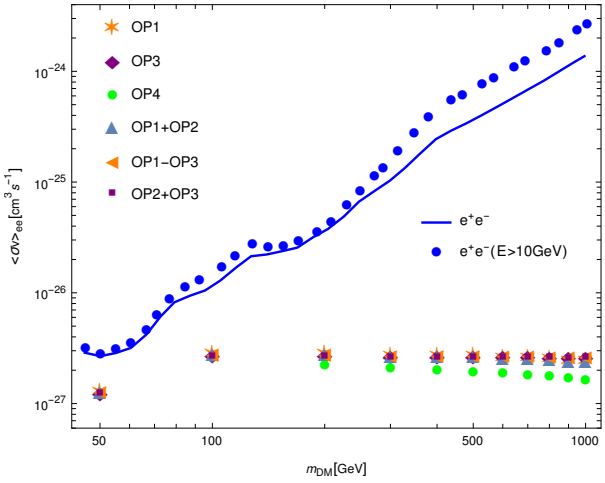

(a) Annihilation into e^+e^-

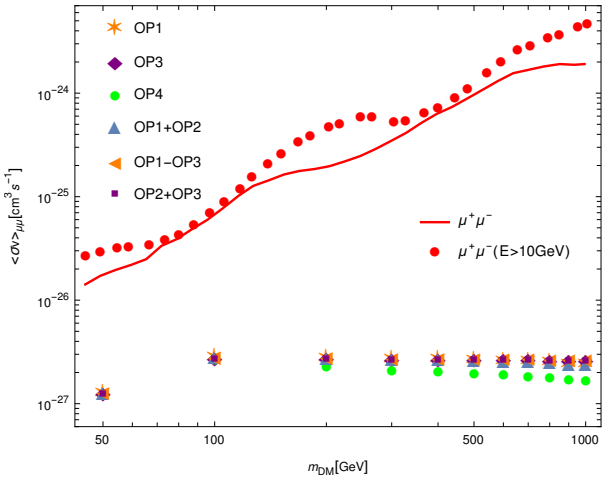

(b) Annihilation into $\mu^+\mu^-$

Figure 7.3: Restrictions from AMS-02 data on the DM annihilation cross sections into (a) e^+e^- and (b) $\mu^+\mu^-$ for the portals generated by several operators, defined in eq. (6.19). We see that the entire mass region is allowed by the data. The limits shown as solid lines were derived from sampling over various energy windows, while the dashed lines are from considering those windows including only data with energies above 10 GeV [125].

We refine our calculation of the DM annihilation cross sections done previously in subsection 6.5.3 (in ref. [144]) [4] and the region of masses allowed was slightly modified.

[4]Before, we used the first two terms of a series expansion of $\langle\sigma v\rangle$ as a function of $x = m/T$, where m stands for the DM mass and T is the temperature. In this complementary work we used micrOMEGAs to compute $\langle\sigma v\rangle$ more accurately (the updated values are shown in fig. 7.4). This change explains the

This change is only noteworthy in the case of the OP4, because the collider constraints exclude masses in the region $m_\psi < m_Z/2$ for OP1, OP3 and the combinations of OP1 & OP3, as we will see below. The data constraining DM annihilation into the final state e^+e^- is the most stringent, therefore is the one we present here, in fig. 7.4. We see that masses smaller than ~ 30 GeV are ruled out, while masses in the range $[30, 50]$ GeV are allowed.

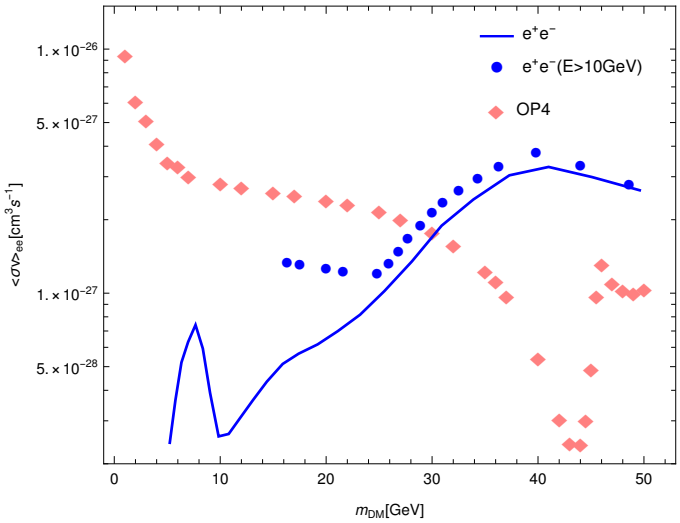

Figure 7.4: Restrictions from AMS-02 data on the DM annihilation cross sections into e^+e^- for the portal generated by OP4, defined in eq. (6.19). This plot tests the mass region $m_\psi < m_Z/2$, and we see that masses larger than ~ 30 GeV are allowed.

7.2.5 Is the EFT perturbative?

We want our EFT to be in the perturbative regime, which imposes an upper limit in the dimensionless effective couplings of eqs. (6.4) and (6.5). We set this limit using that the corresponding $\alpha = g^2/(4\pi)$, where g^2 stands for any coupling in eqs. (6.4) and (6.5), should be at most $\sim 1/2$ to keep perturbativity. As before, we took the effective couplings that correctly reproduce the relic abundance. The quantities that we obtain for all the operators that we are studying satisfy this criteria of perturbativity.

7.3 Collider constraints

The effective operators we are working with allow for the pair production of WIMPs in the proton–proton collisions at the LHC. If one of the incoming partons radiates a jet through initial state radiation (ISR), one can observe the process $pp \to \chi\chi j$ as a single jet

small difference in the low mass region of OP4, between the results summarized in tables 6.2 and 7.1.

associated with missing transverse energy ($\not{E}_T$). In this study, we include the ATLAS [151] monojet analysis based on 139 fb^{-1} of data from Run II. ATLAS has performed a number of further searches for other types of ISR, leading for example to mono-photon signatures (see figure 3.4), but these are known to give weaker bounds on DM EFTs than monojet searches [157–159].

Starting from UFO files generated using LanHEP v4.0.0 [160], we have then generated the process $pp \to \chi\chi j$ with MadGraph_aMC@NLO v3.4.0 [161] for the ATLAS analysis, interfaced to Pythia v8.3 [162] for parton showering and hadronization. The detector response is simulated using the ATLAS detector configuration [163] in FastJet v3.3.3 [164]. We apply the following kinematic cuts from Ref. [151]: $E_T^{\text{miss}} > 200$ GeV, a leading jet with $p_T > 150$ GeV and $|\eta| < 2.4$, and up to three additional jets with $p_T > 30$ GeV and $|\eta| < 2.8$.

We validated our analysis by reproducing the green dash-dotted line in figure 7.5, using a simplified DM model where Dirac fermion WIMPs (χ) are pair-produced from quarks via s-channel exchange of a spin-1 mediator particle (Z_A) with axial-vector couplings [151].

In this analysis we only include the operators (and combinations of them) that still had mass regions with suitable solutions, allowed even after all the constraints imposed by non-collider experiments we have considered. The results reported by ATLAS were obtained using proton-proton collision data at a center-of-mass energy of $\sqrt{s} = 13$ TeV. Events were required to have at least one jet with transverse momentum above 200 GeV and no reconstructed leptons or photons. Due to the $\sqrt{s} = 13$ TeV center-of-mass energy, the maximum mass we considered in our simulations was 6.4 TeV. We use the data points in fig. 7.5 of the measured distributions of p_T^{recoil}. We show below the results obtained by comparing the data from ATLAS [151] (see fig. 7.5) with the simulated results for each operator.

We also wanted to complement our previous results, shown in table 6.2, so we tested the mass region $m_{\text{DM}} < m_Z/2$, with suitable solutions according to the experimental data analyzed there. We show below the comparison of the simulated events, for masses previously allowed, with the ATLAS data.

7.4 Discussion and Conclusions

To make a brief summary of our previous results from non-collider constraints, we recall that operators OP2, OP5 and the combinations OP1+OP2, OP2+OP3, OP4+OP5 were already excluded in the range [50 GeV − 6.4 TeV] by direct detection experiments data.

- OP1. In fig. 7.6 we evaluated $m_\psi = 50$ GeV, 100 GeV, 200 GeV and 300 GeV and we observe that all these masses are allowed. In fig. 7.7 we use the benchmark points

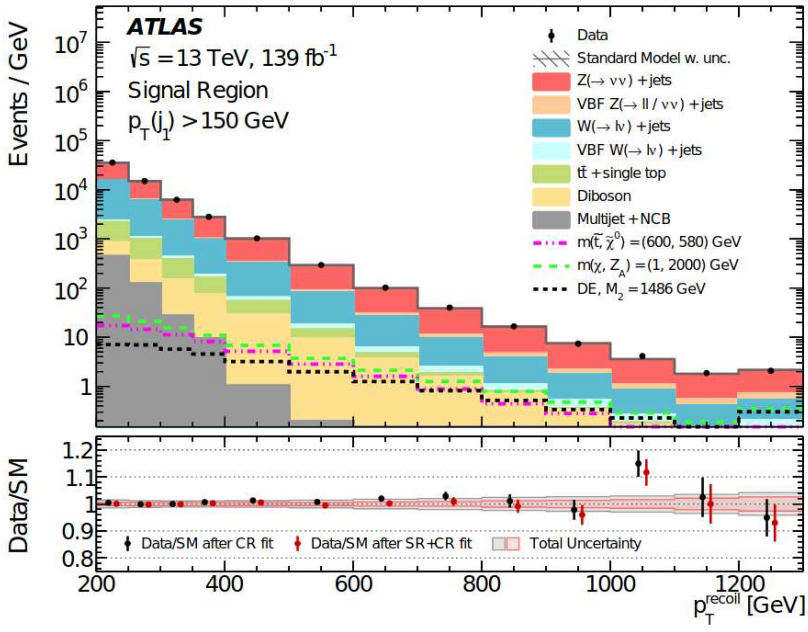

Figure 7.5: Measured distributions of p_T^{recoil} for $p_T^{\text{recoil}} > 200$ GeV selection [151] compared with the SM predictions in the signal region.

(a): 0.0025 GeV, 0.01 GeV, 0.1 GeV and 2 GeV, and (b) 41 GeV, 42 GeV , 43 GeV and 44.5 GeV. We see that masses smaller than 43 GeV are ruled out for this operator.

- OP3. We evaluated the masses: 175 GeV, 190 GeV and 225 GeV in fig. 7.8(a) and 35 GeV, 40 GeV and 44.5 GeV in fig. 7.8(b). We see in fig. 7.8(a) that masses larger than 190 GeV are allowed. For this operator the region $m_\psi < m_Z/2$ is now entirely excluded.

- OP4. In fig. 7.9 we use the benchmark points: (a) 50 GeV, 100 GeV, 150 GeV, 200 GeV and 300 GeV and (b) 100 GeV, 36 GeV, 40 GeV and 44.5 GeV. We see in both figures that all values are allowed by the data.

- OP1&OP2. We use benchmark points for 0.0025 GeV, 0.01 GeV, 0.1 GeV and 2 GeV in fig. 7.10. We see that all these masses are excluded by the data.

- OP1&OP3. We evaluated the masses: (a) 200 GeV, 300 GeV, 325 GeV and 350 GeV, and (b) 50 GeV, 100 GeV, 140 GeV, 150 GeV and 200 GeV. In fig. 7.11(a) we use the same sign for the effective couplings and in fig. 7.11(b) we use a relative sign between the operators. The masses allowed are (a) larger than 325 GeV and (b) larger than 140 GeV. Finally, for DM masses below $m_Z/2$, we tested the benchmark points: fig. 7.12(a) 0.0025 GeV, 0.01 GeV, 0.1 GeV and 2 GeV and fig. 7.12(b) 35

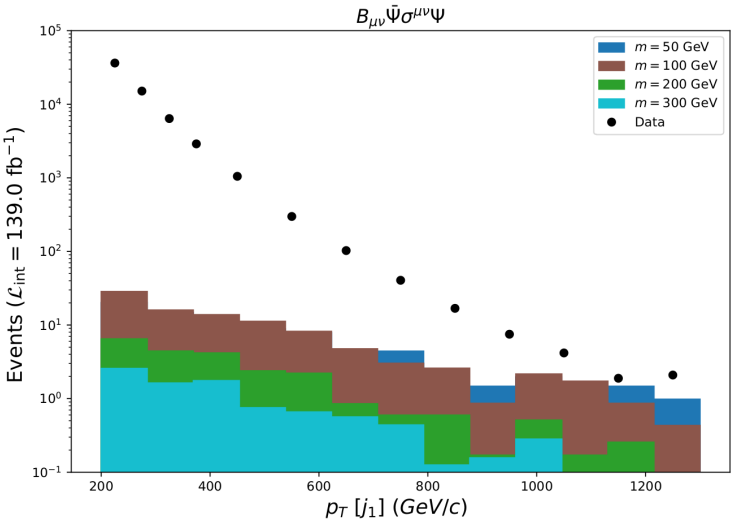

Figure 7.6: p_T distributions simulated using OP1 of eq. (6.19), vs ATLAS data (fig. 7.5). We use benchmark points for 50 GeV, 100 GeV, 200 GeV and 300 GeV. We see that all these masses are allowed.

GeV, 40 GeV, 44 GeV. We see that in both figures the whole mass range is ruled out by the data ($m_{\rm DM} \in [44\ {\rm GeV}, m_Z/2]$ was already excluded by analysis of positron measurements, see table 6.2).

We present a summary of our results in table 7.1.

Operator	**Dim.**	**DM candidate**	**Allowed DM mass**
1.- $B_{\mu\nu}\bar{\Psi}\sigma^{\mu\nu}\Psi$	5	Ψ fermion	$\gtrsim 43$ GeV *
2.- $\left(\bar{\psi}\gamma_\mu\psi\right)\left(\bar{\Psi}\gamma^\mu P_{L,R}\Psi\right)$	6	Ψ fermion	none
3.- $B_{\mu\nu}\bar{\Psi}(\gamma^\mu \overleftrightarrow{\mathcal{D}}^\nu - \gamma^\nu \overleftrightarrow{\mathcal{D}}^\mu)P_{L,R}\Psi$	6	Ψ fermion	$\gtrsim 190$ GeV
4.- $B_{\mu\nu}X^{\mu\nu}\Phi$	5	vector X, scalar Φ	$\gtrsim 30$ GeV *
5.- $\left(\bar{\psi}\gamma_\mu\psi\right)\ \frac{1}{2i}\Phi^\dagger \overleftrightarrow{\mathcal{D}}^\mu \Phi$	6	scalar Φ	none
1 ± 2	5+6	Ψ fermion	none
$1 + 3$	5+6	Ψ fermion	$\gtrsim 325$ GeV
$1 - 3$	5+6	Ψ fermion	$\gtrsim 140$ GeV
2 ± 3	6	Ψ fermion	none

Table 7.1: Summary of results obtained in this work, which supersede those in our previous paper [144]. In addition to the experimental constraints used therein, now we also considered the limits from ATLAS in ref. [151]. *We note that the region $(m_Z \pm \Gamma_Z)/2$ is excluded, see Table 6.2.

The constraining power of ATLAS results forbids mostly light DM particles with masses below $m_Z/2$. For OP1 and OP4, we still have solutions below $m_Z/2$, while for OP3 and the combination of OP1&OP3 we need larger masses to satisfy the ATLAS constraints. Future LHC analyses will set even tighter constraints on DM, particularly

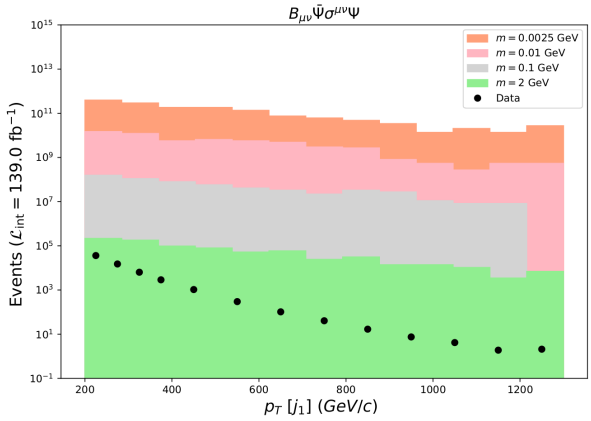

(a)

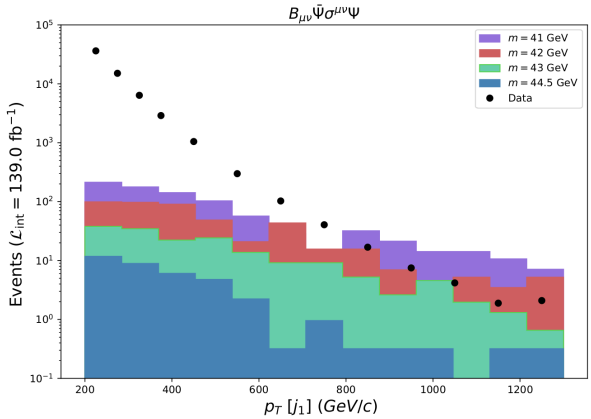

(b)

Figure 7.7: p_T distributions simulated using OP1 of eq. (6.19), vs ATLAS data (fig. 7.5). We use benchmark points for (a) 0.0025 GeV, 0.01 GeV, 0.1 GeV and 2 GeV, and (b) 41 GeV, 42 GeV, 43 GeV and 44.5 GeV. We see that masses smaller than 43 GeV are excluded by the data.

within our EFT and, specifically, for the subset of operators (those with spin-one mediators) considered in this work.

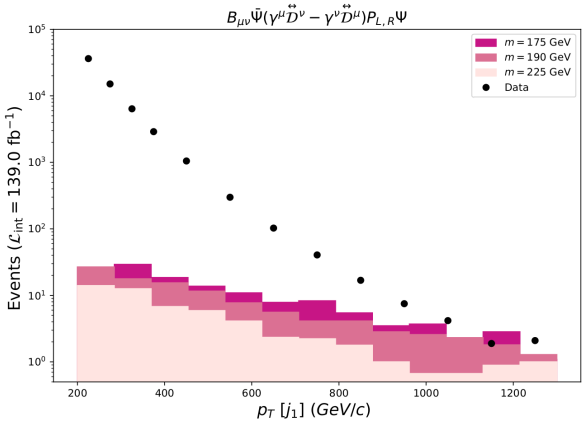

(a)

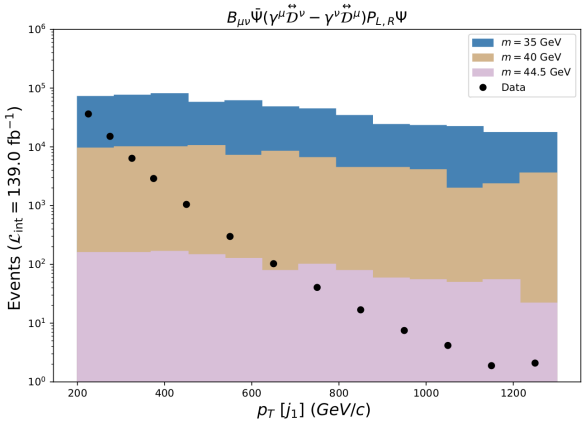

(b)

Figure 7.8: p_T distributions simulated using OP3 of eq. (6.19), vs ATLAS data (fig. 7.5). We use benchmark points for (a) 175 GeV, 190 GeV and 225 GeV and (b) 35 GeV, 40 GeV and 44.5 GeV. The plot in (a) shows that masses above 190 GeV are allowed, while in (b) we see that all the region is excluded.

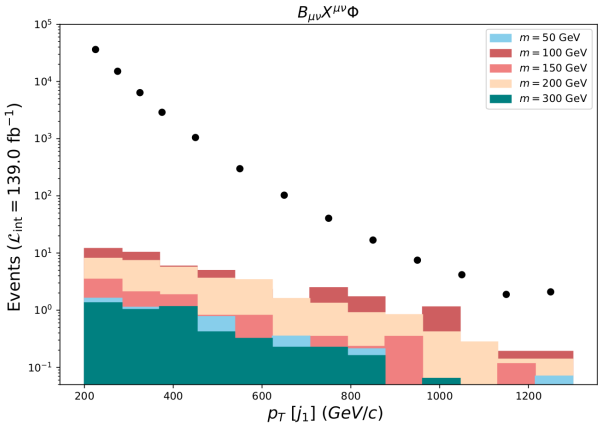

(a)

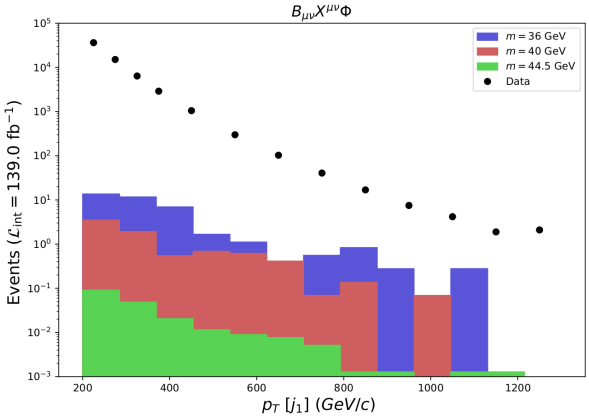

(b)

Figure 7.9: p_T distributions simulated using OP4 of eq. (6.19), vs ATLAS data (fig. 7.5). We use benchmark points for (a) 50 GeV, 100 GeV, 150 GeV, 200 GeV and 300 GeV and (b) 36 GeV, 40 GeV and 44.5 GeV. We see that all these masses are allowed.

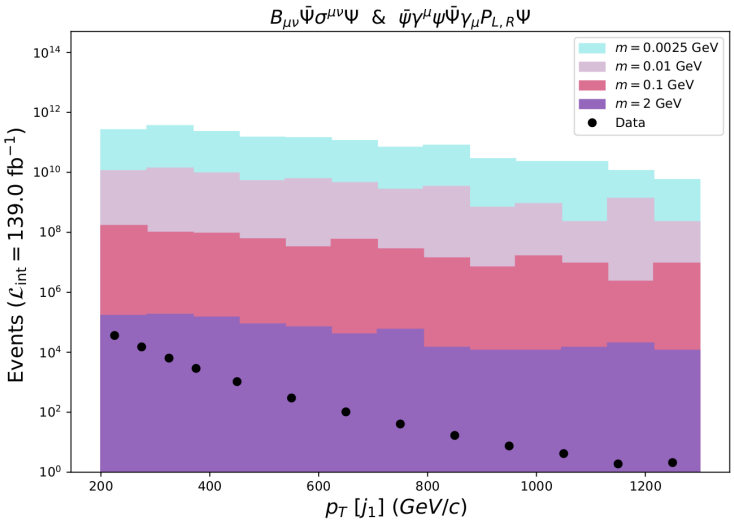

Figure 7.10: p_T distributions simulated using OP1&OP2 of eq. (6.19), vs ATLAS data (fig. 7.5). We use benchmark points for 0.0025 GeV, 0.01 GeV, 0.1 GeV and 2 GeV. We see that all these masses are ruled out.

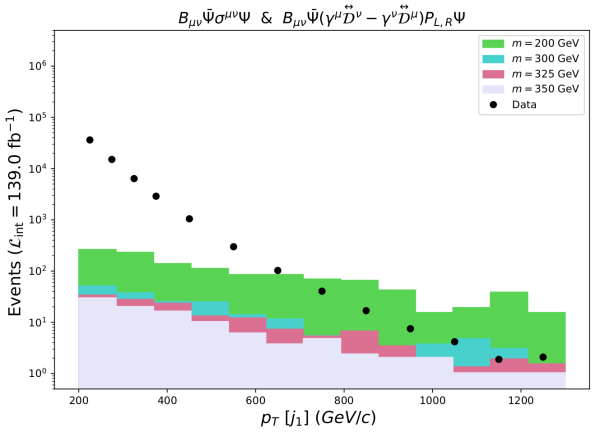

(a) OP1+OP3

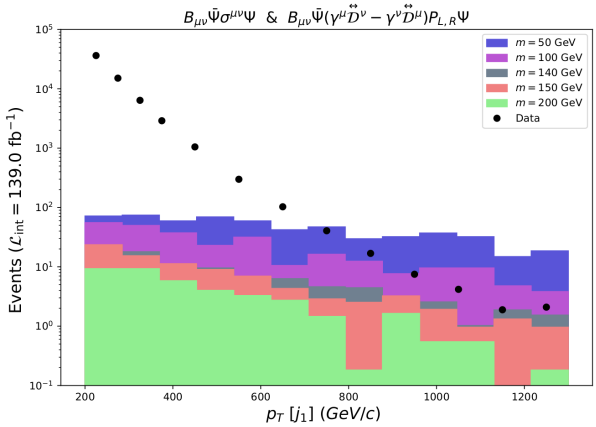

(b) OP1-OP3

Figure 7.11: p_T distributions simulated using (a) OP1+OP3 and (b) OP1-OP3 of eq. (6.19), vs ATLAS data (fig. 7.5). We use benchmark points for (a) 200 GeV, 300 GeV, 325 GeV and 350 GeV and (b) 50 GeV, 100 GeV, 140 GeV, 150 GeV and 200 GeV. The masses allowed are (a) above 325 GeV and (b) above 140 GeV.

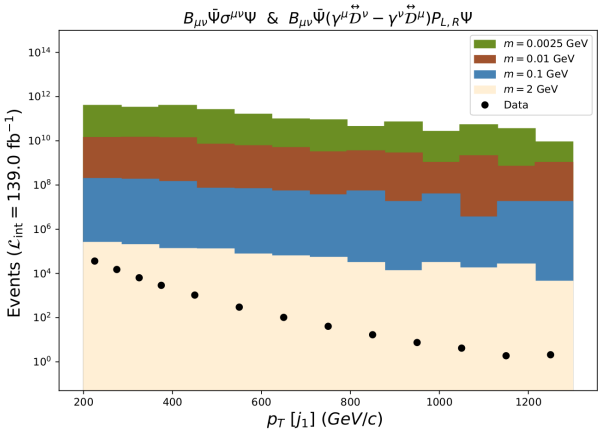

(a)

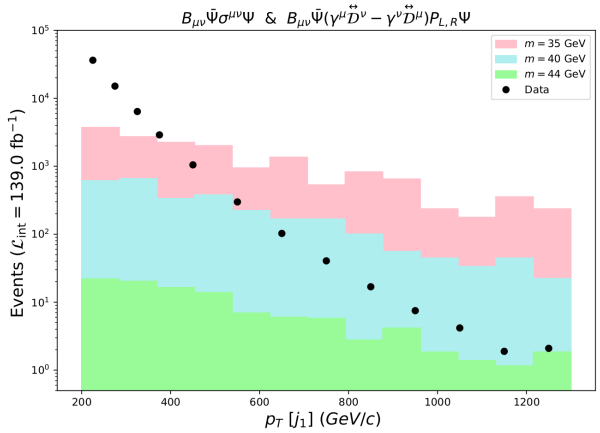

(b)

Figure 7.12: p_T distributions simulated using OP1 & OP3 of eq. (6.19), vs ATLAS data (fig. 7.5). We use benchmark points for (a) 0.0025 GeV, 0.01 GeV, 0.1 GeV and 2 GeV and (b) 35 GeV, 40 GeV and 44 GeV. In (a) all the masses are ruled out by the data, while in (b) masses larger than 44 GeV are allowed.

Chapter 8

Indirect limits on $\ell_i \to \ell_j\gamma\gamma$ from $\ell_i \to \ell_j\gamma$

8.1 Overview

Here we consider the cLFV decays of leptons to two photons, $\ell_i \to \ell_j\gamma\gamma$ [65,66,165], which have been explored in less detail than other cLFV processes such as the single photon process, $\ell_i \to \ell_j\gamma$, specially for the case of $\tau \to \ell\gamma\gamma$ [67, 166–169].

Experimentally, $\mu \to e\gamma\gamma$ was searched for by several experiments aiming also for $\mu \to e\gamma$. The latest of these experiments was the Crystal Box detector, whose result still provides the strongest bound for $\mu \to e\gamma\gamma$ [170]. This limit is however two orders of magnitude weaker than present $\mu \to e\gamma$ bounds, see Table 8.1, since the MEG experiment was optimized for back-to-back topologies and no new dedicated experiment for $\mu \to e\gamma\gamma$ has been carried out since Crystal Box. On the other hand, $\tau \to \ell\gamma\gamma$ has rarely been searched for. To the best of our knowledge, the only existing direct experimental search was performed by ATLAS, setting an upper limit of $\text{BR}(\tau \to \mu\gamma\gamma) < 1.5 \times 10^{-4}$ after the LHC run-I [171]. No direct experimental search exists for $\tau \to e\gamma\gamma$.

An alternative for exploring the $\ell_i \to \ell_j\gamma\gamma$ channels is to recast the searches for $\ell_i \to \ell_j\gamma$, as some of the events of the former would fall into the signal region defined for the latter [66]. This idea has been recently applied to recast the BABAR search for $\tau \to \ell\gamma$ [172], finding that at 90%CL $\text{BR}(\tau \to \mu\gamma\gamma) < 5.8 \times 10^{-4}$ and $\text{BR}(\tau \to e\gamma\gamma) < 2.5 \times 10^{-4}$ [67]. These limits are however several orders of magnitude weaker than the associated ones on $\tau \to \ell\gamma$ due to the low acceptance of these searches for $\tau \to \ell\gamma\gamma$ events.

In this chapter, we consider the theoretical correlation between the $\ell_i \to \ell_j\gamma\gamma$ and the $\ell_i \to \ell_j\gamma$ decays. Clearly, any scenario generating $\ell_i \to \ell_j\gamma$ would automatically generate a (model-independent) contribution to $\ell_i \to \ell_j\gamma\gamma$, from the radiation of an additional photon in the final state. Further, any scenario generating $\ell_i \to \ell_j\gamma\gamma$ will generate a

Decay Mode	Current upper limit on BR (90%CL)	
$\mu \to e\gamma$	4.2×10^{-13}	MEG (2016) [173]
$\mu \to e\gamma\gamma$	7.2×10^{-11}	Crystal Box (1986) [170]
$\tau \to e\gamma$	3.3×10^{-8}	BaBar (2010) [172]
$\tau \to \mu\gamma$	4.2×10^{-8}	Belle (2021) [174]
$\tau \to \mu\gamma\gamma$	1.5×10^{-4}	ATLAS (2017) [171]

Table 8.1: Experimental upper bounds on the rates of the $\ell_i \to \ell_j\gamma(\gamma)$ decays.

(model-dependent) contribution to $\ell_i \to \ell_j\gamma$ at the quantum level. Barring cancellations, the quantum-induced contribution should not exceed the experimental upper limits on $\ell_i \to \ell_j\gamma$, which in turn allows to set indirect limits on the rates of $\ell_i \to \ell_j\gamma\gamma$.

We will pursue an EFT approach to study these correlations, in order to ensure the generality of our conclusions. Notably, our indirect limits on the process $\ell_i \to \ell_j\gamma\gamma$ will turn out to be more stringent than the current direct bounds. Furthermore, these limits do not preclude the possibility of observing the rare decays $\tau \to \ell\gamma\gamma$ at Belle II or at a Super Tau Charm Factory, which then represents a competitive probe of cLFV along with the more studied channels $\tau \to \ell\gamma$ or $\tau \to \ell_j\ell_k\bar{\ell}_k$.

This chapter is organized as follows: in section 8.2 we introduce the Lagrangian that we will use [66]. Then, in section 8.3 we establish the relation between the tree level process $\ell_i \to \ell_j\gamma\gamma$ and the one loop generated process $\ell_i \to \ell_j\gamma$, and we show the indirect limits obtained through these expressions. After that, in section 8.4 we discuss possible scenarios where the dimension-5 operators could be suppressed with respect to the dimension-7 operators. Finally we present our conclusions in section 8.5.

8.2 Effective field theory

The effective interaction between two charged leptons of different flavor and two photons is given by [66]

$$
\begin{aligned}
\mathcal{L}_{\rm Int} = & \left(G_{SR}^{ij}\bar{\ell}_{L_i}\ell_{R_j} + G_{SL}^{ij}\bar{\ell}_{R_i}\ell_{L_j}\right) F_{\mu\nu}F^{\mu\nu} \\
& + \left(\tilde{G}_{SR}^{ij}\bar{\ell}_{L_i}\ell_{R_j} + \tilde{G}_{SL}^{ij}\bar{\ell}_{R_i}\ell_{L_j}\right) \tilde{F}_{\mu\nu}F^{\mu\nu} \\
& + \left(G_{VL}^{ij}\bar{\ell}_{L_i}\gamma^{\sigma}\ell_{L_j} + G_{VR}^{ij}\bar{\ell}_{R_i}\gamma^{\sigma}\ell_{R_j}\right) F^{\mu\nu}\partial_{\nu}F_{\mu\sigma} \\
& + \left(\tilde{G}_{VL}^{ij}\bar{\ell}_{L_i}\gamma^{\sigma}\ell_{L_j} + \tilde{G}_{VR}^{ij}\bar{\ell}_{R_i}\gamma^{\sigma}\ell_{R_j}\right) F^{\mu\nu}\partial_{\nu}\tilde{F}_{\mu\sigma} \\
& + h.c.\,, \qquad (8.1)
\end{aligned}
$$

where the subscripts $L(R)$ indicate the chirality of the lepton and i, j are generation indices, $\tilde{F}_{\mu\nu} = \frac{1}{2}\epsilon_{\mu\nu\sigma\lambda}F^{\sigma\lambda}$ is the dual tensor.

On the other hand, the effective interaction Lagrangian between two charged leptons of different flavor and one photon has dimension 5 and reads:

$$
\mathcal{L}_{\text{dim-5}} = D_R^{ij}\,\bar{\ell}_{L_i}\sigma_{\mu\nu}\ell_{R_j}F^{\mu\nu} + D_L^{ij}\,\bar{\ell}_{R_i}\sigma_{\mu\nu}\ell_{L_j}F^{\mu\nu} + h.c. \qquad (8.2)
$$

The effective Lagrangians in Eqs. (8.1) and (8.2) generate at tree level the decay $\ell_i \to \ell_j\gamma\gamma$, through the diagrams shown in the upper panel of Fig. 8.1. The expression for the differential decay rate is complicated and is given in Appendix A. For the specific case where the rate is dominated by the dimension-7 operators, the total decay rate is given by:

$$
\Gamma(\ell_i \to \ell_j\gamma\gamma) = \frac{|G_{ij}|^2}{3840\pi^3}\, m_i^7\,, \qquad (8.3)
$$

where we have neglected the mass of the final lepton, and

$$
|G_{ij}|^2 = \left|G_{SL}^{ij} + \frac{im_iG_{VR}^{ij}}{4}\right|^2 + \left|G_{SR}^{ij} + \frac{im_iG_{VL}^{ij}}{4}\right|^2 + \left|\tilde{G}_{SL}^{ij} + \frac{im_i\tilde{G}_{VR}^{ij}}{2}\right|^2 + \left|\tilde{G}_{SR}^{ij} + \frac{im_i\tilde{G}_{VL}^{ij}}{2}\right|^2 . \qquad (8.4)
$$

On the other hand, when it is dominated by the dimension-5 operators, we obtain

$$
\Gamma(\ell_i \to \ell_j\gamma\gamma) = \frac{\alpha\, m_i^3}{48\pi^2}\left(|D_R^{ij}|^2 + |D_L^{ij}|^2\right)\lambda\left(\tfrac{E_\gamma^{\rm cut}}{m_i}\right)\,, \qquad (8.5)
$$

with $E_\gamma^{\rm cut}$ an energy cut-off introduced to regularize the infrared and collinear divergences

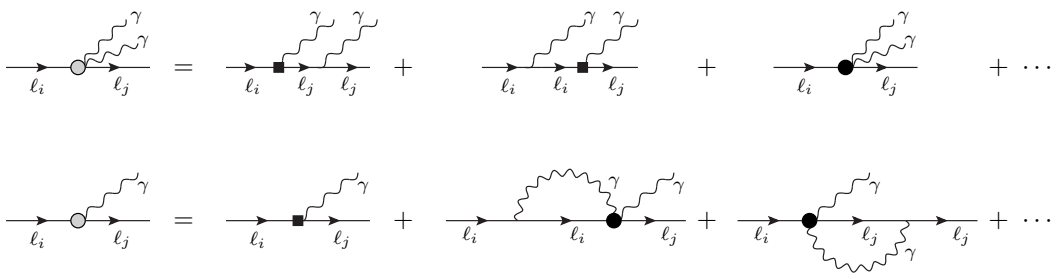

Figure 8.1: Feynman diagrams contributing to $\ell_i \to \ell_j\gamma\gamma$ (top panel) and $\ell_i \to \ell_j\gamma$ (bottom panel) in the effective field theory described by the Lagrangians in eq. (8.2) (black squares) and eq. (8.1) (black circles). The dots represent higher order contributions.

in the rate (see App. A), and

$$\begin{aligned}\lambda(x) \simeq\ & 6 + 2\pi^2 + 6\log^2 2 + 21\log(2x) + 6\log(x)\,\log(4x) \\ & + 18x\big(2\log(2x) + 1\big) + 6x^2\big(8\log(2x) - 29\big) \\ & + \mathcal{O}(x^3)\,. \end{aligned} \tag{8.6}$$

8.3 Correlating $\ell_i \to \ell_j\gamma\gamma$ and $\ell_i \to \ell_j\gamma$

Let us first consider scenarios where the dimension-5 operators are not suppressed, so the rate for $\ell_i \to \ell_j\gamma\gamma$ is approximately given by eq. (8.5). Clearly, the dimension-5 operators also induce the decay $\ell_i \to \ell_j\gamma$ (see lower panel of Fig. 8.1). The rate is given by

$$\Gamma(\ell_i \to \ell_j\gamma) = \frac{m_i^3}{4\pi}\left(\left|D_R^{ij}\right|^2 + \left|D_L^{ij}\right|^2\right)\,, \tag{8.7}$$

whence one obtains

$$\Gamma(\ell_i \to \ell_j\gamma\gamma) = \frac{\alpha}{12\pi}\,\lambda\left(\frac{E_\gamma^{\rm cut}}{m_i}\right)\,\Gamma(\ell_i \to \ell_j\gamma)\,. \tag{8.8}$$

Using the upper limits on the rates for $\ell_i \to \ell_j\gamma$ from Table 8.1 and imposing $E_\gamma^{\rm cut} = 7\,(50)$ MeV for $\mu\,(\tau)$ decays, one finds the indirect limits:

$$\begin{aligned} &{\rm BR}(\mu \to e\gamma\gamma) \lesssim 2\times 10^{-16}\,, \\ &{\rm BR}(\tau \to e\gamma\gamma) \lesssim 8\times 10^{-11}\,, \\ &{\rm BR}(\tau \to \mu\gamma\gamma) \lesssim 1\times 10^{-10}\,. \end{aligned} \tag{8.9}$$

The effect of the dimension-8 operators is not only suppressed by higher powers of the

cut-off scale of the EFT, but also by the mass of the decaying lepton, due to the helicity flip, therefore we will focus first in the analysis of the dimension-7 operators. Afterwards, we will present the results obtain with the dimension-8 operators to complement the work.

There could be scenarios where the dimension-5 operators are suppressed, while not the dimension-7 operators (see Section 8.4). In this case, the decay $\ell_i \to \ell_j \gamma$ is induced at the one loop-level (see lower panel of Fig. 8.1). In this case, and keeping only the leading terms, one finds:

$$\Gamma(\ell_i \to \ell_j \gamma) \sim \frac{\alpha\,|G_{ij}|^2}{256\,\pi^4}\, m_i^7\, \log^2\left(\frac{\Lambda^2}{m_i^2}\right)\,, \tag{8.10}$$

where Λ is the cut-off energy scale of the effective field theory. Using eq. (8.3) one obtains an approximate correlation between rates

$$\Gamma(\ell_i \to \ell_j \gamma) \sim \frac{15\alpha}{\pi}\, \log^2\left(\frac{\Lambda^2}{m_i^2}\right)\, \Gamma(\ell_i \to \ell_j \gamma\gamma)\,, \tag{8.11}$$

from where one can derive indirect upper limits for $\ell_i \to \ell_j\gamma\gamma$ from the upper limits on $\ell_i \to \ell_j\gamma$:

$$\begin{aligned}
\mathrm{BR}(\mu \to e\gamma\gamma) &\lesssim 6.4\times 10^{-14}\Big[1+0.15\log\tfrac{\Lambda}{100\,\mathrm{GeV}}\Big]^{-2},\\
\mathrm{BR}(\tau \to e\gamma\gamma) &\lesssim 1.5\times 10^{-8}\,\Big[1+0.25\log\tfrac{\Lambda}{100\,\mathrm{GeV}}\Big]^{-2},\\
\mathrm{BR}(\tau \to \mu\gamma\gamma) &\lesssim 1.9\times 10^{-8}\,\Big[1+0.25\log\tfrac{\Lambda}{100\,\mathrm{GeV}}\Big]^{-2},
\end{aligned} \tag{8.12}$$

which have a mild sensitivity to the cut-off scale.

Consider now a scenario where both the dimension-5 and dimension-7 operators are suppressed, while not the dimension-8 operators. Again the $\ell_i \to \ell_j\gamma$ decay is generated at one loop level (as in the lower panel of Fig. 8.1). In this scenario, keeping the leading terms, we obtain:

$$\Gamma(\ell_i \to \ell_j \gamma) \sim \frac{\alpha}{\pi^4}\, m_i^9\, \left(\frac{25|(|G_{VL}^{ij}|^2+|G_{VR}^{ij}|^2)}{36864} + \frac{|(|\tilde{G}_{VL}^{ij}|^2+|\tilde{G}_{VR}^{ij}|^2)}{9216}\right) \log^2\left(\frac{\Lambda^2}{m_i^2}\right)\,, \tag{8.13}$$

Including only the contribution of the dimension-8 operators without dual tensor (third row in eq. 8.1), we find the correlation

$$\Gamma(\ell_i \to \ell_j \gamma) \sim \frac{125\alpha}{12\pi}\, \log^2\left(\frac{\Lambda^2}{m_i^2}\right)\, \Gamma(\ell_i \to \ell_j \gamma\gamma)\,, \tag{8.14}$$

from where one can also derive indirect upper limits for $\ell_i \to \ell_j\gamma\gamma$:

$$\begin{aligned}
\mathrm{BR}(\mu \to e\gamma\gamma) &\lesssim 2.3 \times 10^{-14} \left[1 + 0.15 \log \tfrac{\Lambda}{100\,\mathrm{GeV}}\right]^{-2}, \\
\mathrm{BR}(\tau \to e\gamma\gamma) &\lesssim 5.2 \times 10^{-9} \left[1 + 0.25 \log \tfrac{\Lambda}{100\,\mathrm{GeV}}\right]^{-2}, \\
\mathrm{BR}(\tau \to \mu\gamma\gamma) &\lesssim 6.7 \times 10^{-9} \left[1 + 0.25 \log \tfrac{\Lambda}{100\,\mathrm{GeV}}\right]^{-2}.
\end{aligned} \tag{8.15}$$

Analogously, we can take only the contribution of the dimension-8 operators with the dual tensor (fourth row in eq. 8.1), and we obtain the correlation

$$\Gamma(\ell_i \to \ell_j \gamma) \sim \frac{5\alpha}{3\pi} \log^2\left(\frac{\Lambda^2}{m_i^2}\right) \Gamma(\ell_i \to \ell_j \gamma\gamma)\,, \tag{8.16}$$

from where we can derive the following indirect upper limits for $\ell_i \to \ell_j\gamma\gamma$:

$$\begin{aligned}
\mathrm{BR}(\mu \to e\gamma\gamma) &\lesssim 5.8 \times 10^{-13} \left[1 + 0.15 \log \tfrac{\Lambda}{100\,\mathrm{GeV}}\right]^{-2}, \\
\mathrm{BR}(\tau \to e\gamma\gamma) &\lesssim 1.3 \times 10^{-7} \left[1 + 0.25 \log \tfrac{\Lambda}{100\,\mathrm{GeV}}\right]^{-2}, \\
\mathrm{BR}(\tau \to \mu\gamma\gamma) &\lesssim 1.7 \times 10^{-7} \left[1 + 0.25 \log \tfrac{\Lambda}{100\,\mathrm{GeV}}\right]^{-2}.
\end{aligned} \tag{8.17}$$

Regardless of the underlying physics generating the process $\ell_i \to \ell_j\gamma\gamma$, our indirect limits are significantly more stringent than the current direct limits. Concretely, focusing on our limits from dimension-7 operators, the limit on $\mu \to e\gamma\gamma$ is about three orders of magnitude stronger than the direct search using the Crystal Box detector and the limit on $\tau \to \mu\gamma\gamma$ is about four orders of magnitude stronger than the direct search performed at ATLAS. Future foreseeable sensitivities of MEG II searching for $\mu \to e\gamma$ and of Belle II for $\tau \to \ell\gamma$ will improve our indirect limits by about one order of magnitude.

Furthermore, the results in Eqs. (8.12, 8.15, 8.17) motivate a dedicated experimental search for the $\tau \to \ell\gamma\gamma$ decays, since this decay might be at the reach of future experiments [175]. Let us consider the specific case of the Belle II experiment. Assuming that Belle II could achieve the same sensitivity for double than for single photon processes, as occurred in the Crystal Box Detector for muon decays [87], Belle II could probe the $\tau \to \ell\gamma\gamma$ decays with branching ratios as small as $\mathcal{O}(10^{-9})$ [175]. If this sensitivity is reached, Belle II will probe uncharted parameter space of the dimension-7 and dimension-8 operators, and possibly find evidence for cLFV by the observation of the decay $\tau \to \ell\gamma\gamma$.

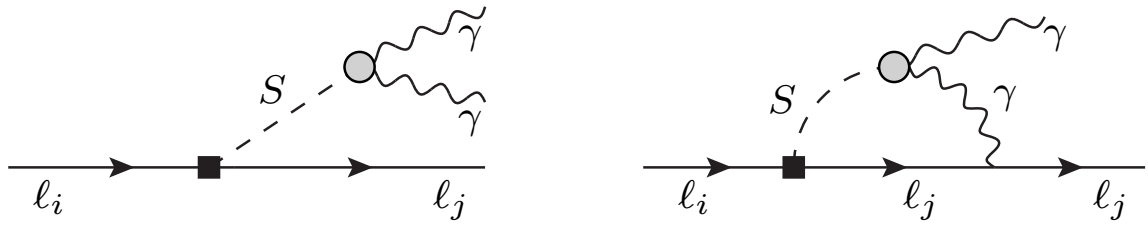

Figure 8.2: Example of diagrams generating $\ell_i \to \ell_j\gamma\gamma$ and $\ell_i \to \ell_j\gamma$ mediated by a scalar with off-diagonal Yukawa couplings and an effective vertex to two photons.

8.4 Models with enhanced $\ell_i \to \ell_j\gamma\gamma$

There are several scenarios where the dimension-5 operators could be suppressed with respect to the dimension-7 operators, thereby enhancing the rate of $\ell_i \to \ell_j\gamma\gamma$ compared to $\ell_i \to \ell_j\gamma$. For instance, it was argued in [66] that in models where cLFV was mediated by charged heavy leptons [176], the GIM suppression [60] could be stronger for $\ell_i \to \ell_j\gamma$ than for $\ell_i \to \ell_j\gamma\gamma$. Also, in Ref. [165] it was argued that in some new physics models the dimension-7 operators could actually arise at $\mathcal{O}(1/\Lambda^2)$, instead of the naive expectation of $\mathcal{O}(1/\Lambda^3)$, so their contributions would be less suppressed than expected.

Another interesting possibility arises in models where the cLFV is mediated by heavy scalars, such as a two Higgs doublet model (2HDM) with off-diagonal Yukawa interactions. In this scenario, $\ell_i \to \ell_j\gamma$ decays are induced at one-loop level, however they are suppressed by three chiral flips and therefore the two-loop (Barr-Zee diagrams) contributions are actually the dominant ones [177]. On the other hand, the $\ell_i \to \ell_j\gamma\gamma$ decays do not suffer from this chirality suppression, the dominant contributions are at the one-loop and, consequently, they can have ratios comparable to those of $\ell_i \to \ell_j\gamma$.

More concretely, one can consider a scenario containing a heavy scalar S with off-diagonal Yukawa couplings to leptons and an effective vertex to two photons (which matches to the framework in Ref. [177] when integrating out the top and W boson). The double and single photon decays are then generated by diagrams such as those in Fig. 8.2, which in the heavy scalar limit reduce to a local interaction and Fig. 8.1, respectively. We have explicitly checked that, in this heavy limit, we recover our EFT result of eq. (8.11) with $\Lambda = m_S$.

8.5 Conclusions

Pursuing an effective field theory approach, we have derived model-independent upper limits on the rates of $\ell_i \to \ell_j\gamma\gamma$ from the current experimental limits on $\ell_i \to \ell_j\gamma$. Our

indirect limits are, even under the most conservative assumptions, significantly more stringent than the current direct limits, concretely three orders of magnitude for $\mu \to e\gamma\gamma$ and four orders of magnitude for $\tau \to \mu\gamma\gamma$. When $\ell_i \to \ell_j\gamma\gamma$ is dominantly generated by the same dimension-5 operators generating $\ell_i \to \ell_j\gamma$, the stringent limits on the latter preclude the observation of the former in planned experiments. In contrast, in scenarios where the dimension-5 operators are suppressed compared to the dimension-7 or dimension-8 operators, the rare decays $\ell_i \to \ell_j\gamma\gamma$ can be enhanced compared to $\ell_i \to \ell_j\gamma$, which in our EFT approach is only generated at the one-loop level. In this class of scenarios, the rare decay $\tau \to \mu\gamma\gamma$ could be at the reach of the Belle II experiment or at a proposed Super Tau Charm Facility, and could constitute an stringent probe of lepton flavor violation. We also discussed some possible UV-complete scenarios where $\ell_i \to \ell_j\gamma\gamma$ is enhanced.

Chapter 9

$\ell_i \to \ell_j$ conversion in nuclei induced by effective $\ell_i \ell_j \gamma\gamma$ interactions

9.1 Overview

In the literature, we find plenty of models proposed to describe the cLFV interactions. If cLFV is discovered, experimental bounds on, or observations of, a multitude of independent processes would assist in discriminating among these models. Experimental searches for $\mu - e$ transitions date back to the late 1940's and to this day have set upper bounds for cLFV processes $\mathcal{O}(10^{-12})$ - $\mathcal{O}(10^{-13})$ [87, 178, 179]. In contrast to μ's decays, the cLFV processes involving τ's imply a greater experimental challenge. The best limits come from the B-flavour factories, which have explored LFV τ decays until $\mathcal{O}(10^{-7})$ - $\mathcal{O}(10^{-8})$ sensitivities [180].

The $\ell_i \to \ell_j$ conversion in nuclei is a well-motivated scenario to study cLFV interactions. It has already been pursued in the past to the $\mu \to e$ conversion in nuclei with the strongest limit set by Sindrum II [179]:

$$\mathcal{B}_{\mu e}^{Au} = \frac{\Gamma(\mu^- \mathrm{Au} \to e^- \mathrm{Au})}{\Gamma_{\mathrm{capture}}(\mu^- \mathrm{Au})} < 7 \times 10^{-13}, \qquad 90\%\mathrm{C.L.}$$

For nuclei transitions involving τ, there are still no experimental limits, however, the NA64 experiment at the CERN SPS [181] plans an experimental search for $e \to \tau$ and $\mu \to \tau$ conversion in nuclei.

In this chapter we continue exploring the rarely considered contact interactions involving two leptons of different flavor and two photons [66]. Such interactions could mediate various processes, such as $\ell_i \to \ell_j \gamma\gamma$ decays and $\ell_i \to \ell_j$ conversion in nuclei. S. Davidson *et al.* [165] have studied these interactions in muon transitions ($\mu \to e\gamma\gamma$ and $\mu \to e$ conversion in nuclei) and in chapter 8 (ref. [182]), we used the same effective operators to

perform an analysis to $\ell_i \to \ell_j\gamma\gamma$ decay, including the τ lepton. Particularly, we showed that the strong limits on $\ell_i \to \ell_j\gamma$ transitions allow to derive model-independent bounds on the $\ell_i \to \ell_j\gamma\gamma$ branching ratios which are three to four orders magnitude stronger that current direct experimental searches.

We first compute the $\ell \to \tau$ conversion in nuclei using the direct limits on the effective $\ell_i\ell_j\gamma\gamma$ interactions from the experimental constraints on the $\ell_i \to \ell_j\gamma\gamma$ processes. Then we proceed to use the aforementioned limits on effective $\ell_i\ell_j\gamma\gamma$ interactions from the stronger limits on $\ell_i \to \ell_j\gamma$ transitions. We obtained stringent limits on the $\ell_i \to \tau$ conversion in the presence of nuclei: $\mu^-(e^-) + \mathcal{N}(A,Z) \to \tau^- X$, *i.e.* with a fixed-target of atomic and mass numbers Z and A, respectively, that preclude soon observation of this processes according with the expected sensitivity of NA64 experiment [183]. Husek, Monsálvez-Pozo & Portolés [184] performed a model-independent analysis of LFV tau decays and $\ell_i \to \tau$ conversion in nuclei, using SMEFT [4, 5] operators up to dimension 6. Here we develop an effective analysis of $\ell_i \to \tau$ conversion in nuclei using operators of dimension 7 in the low-energy effective field theory. This process has received little attention due to the complexities of its experimental setting; see, however, the articles [185–190] and references therein. In addition to the NA64 experiment, future foreseen experiments such as the muon collider [191], the electron-ion collider (EIC) [192], the ILC [193] or circular colliders as LHeC [194] might search for this conversion.

This chapter [1] is organized as follows: in section 9.2 we present the effective operators that generate the cLFV. The $\ell_i \to \tau$ conversion process is described in section 9.3. We show the ratio between the conversion probability and the leading contribution to the inclusive deep inelastic lepton-nucleus scattering (the bremsstrahlung cross section, which acts as normalization channel) in section 9.4. We present our results using the best constraint for the $\bar{\tau}\ell\gamma\gamma$ interaction, as well as a brief discussion of the implications in $\mu \to e$ conversion in section 9.5. Finally, we conclude in section 9.6. Appendix B includes analytic results that were omitted in the main text.

9.2 Effective Lagrangian Setup

We present again the interaction between two charged leptons of different flavor and two photons. The low-energy effective Lagrangian up to energy dimension 7 is given by [66]

$$\begin{aligned}\mathcal{L}_{\text{Int}} = &\left(G_{SR}^{ij}\bar{\ell}_{L_i}\ell_{R_j} + G_{SL}^{ij}\bar{\ell}_{R_i}\ell_{L_j}\right) F_{\mu\nu}F^{\mu\nu} \\ &+ \left(\tilde{G}_{SR}^{ij}\bar{\ell}_{L_i}\ell_{R_j} + \tilde{G}_{SL}^{ij}\bar{\ell}_{R_i}\ell_{L_j}\right) \tilde{F}_{\mu\nu}F^{\mu\nu} + h.c.\,. \end{aligned} \tag{9.1}$$

[1] It is based on an ongoing work in collaboration with Xabier Marcano, Marcela Marín and Pablo Roig. To appear soon.

Using this Lagrangian we compute the total decay rate for the $\ell_i \to \ell_j \gamma\gamma$ channel

$$\Gamma(\ell_i \to \ell_j \gamma\gamma) = \frac{|G_{ij}|^2}{3840\pi^3}\, m_i^7\,, \tag{9.2}$$

where we have neglected the mass of the final lepton and $|G_{ij}|^2 = |G_{SL}^{ij}|^2 + |G_{SR}^{ij}|^2 + |\tilde{G}_{SL}^{ij}|^2 + |\tilde{G}_{SR}^{ij}|^2$.

We can constrain our G_{ij} couplings in eq. (9.2) by using the experimental constraint $\mathrm{BR}(\tau \to e\gamma\gamma) < 2.5 \times 10^{-4}$ [195] and the limits on $\mathrm{BR}(\tau \to \mu\gamma\gamma)$ and $\mathrm{BR}(\mu \to e\gamma\gamma)$ from table 8.1

$$\begin{aligned} |G_{\tau e}| &\leq 1.1 \times 10^{-6}\,\mathrm{GeV}^{-3}\,, \\ |G_{\tau\mu}| &\leq 8.5 \times 10^{-7}\,\mathrm{GeV}^{-3}\,, \\ |G_{\mu e}| &\leq 4.2 \times 10^{-9}\,\mathrm{GeV}^{-3}\,. \end{aligned} \tag{9.3}$$

On the other hand, from eq. (8.10) and the experimental upper limits shown in table 8.1, we calculate more stringent constraints for the effective couplings G_{ij}

$$\begin{aligned} |G_{\tau e}| &\leq 8.4 \times 10^{-9} \left[1 + 0.25 \log \frac{\Lambda}{100\ \mathrm{GeV}}\right]^{-1} \mathrm{GeV}^{-3}\,, \\ |G_{\tau\mu}| &\leq 9.5 \times 10^{-9} \left[1 + 0.25 \log \frac{\Lambda}{100\ \mathrm{GeV}}\right]^{-1} \mathrm{GeV}^{-3}\,, \\ |G_{\mu e}| &\leq 1.2 \times 10^{-10} \left[1 + 0.15 \log \frac{\Lambda}{100\ \mathrm{GeV}}\right]^{-1} \mathrm{GeV}^{-3}\,, \end{aligned} \tag{9.4}$$

which have a mild sensitivity to the cut-off scale Λ.

9.3 $\ell_i \to \tau$ conversion in nuclei

The $\mu \to e$ experiments, are typically low-energy processes where the muon becomes bounded before decaying in orbit or being captured by the nucleus [196]. By contrast, the $\ell_i \to \tau$ experiments are based on a fixed-target nucleus hit by an incoming electron or muon beam. The conversion is expected to occur by deep inelastic scattering (DIS) of the lepton off the nucleus [184]. If the energy of the lepton beam is high enough, they break the hadronic structure of the nucleons within the nucleus and interact with its partons, *i.e.* quarks and gluons [181]. We will focus here on inclusive processes whose products of interaction are a τ lepton plus any hadrons, *i.e.*, $\ell_i + \mathcal{N}(A,Z) \to \tau + X$, where we do not have any information about X.

The dynamics of the interacting parton living in the hadronic environment of the nucleus is influenced by low-energy non-perturbative QCD effects. The non-perturbative behavior is encoded by the so-called parton distribution functions (PDFs), which will be one of the most important pieces in our analysis. Using the QCD factorization theorems, we can obtain the total cross-section of the process by calculating the convolution of the perturbative cross-section ($\hat{\sigma}$) with the non-perturbative PDFs (f):

$$\sigma_{\ell\to\tau} = \hat{\sigma} \otimes f. \tag{9.5}$$

We will focus now on the computation of the total cross-section. Given that the perturbative cross-sections are calculated within the framework of perturbation theory, this calculation is correct up to a certain scale, the characteristic energy scale, Q^2. Both the PDFs and the perturbative cross-sections are functions of Q^2, defining $Q^2 = -q^2$, being q^2 the transferred momentum of the system. In addition, the PDFs are also characterized through the fraction of the nucleus momentum carried by the interacting parton, ξ. Therefore, we express the perturbative cross-section as well as the PDFs as a function of the two discussed invariant quantities:

$$\sigma_{\ell\to\tau} = \hat{\sigma}(\xi, Q^2) \otimes f(\xi, Q^2). \tag{9.6}$$

Once the PDFs are written as a function of ξ and Q^2, the data is used to obtain their dependence on the momentum fraction ξ and the DGLAP evolution equations to find their evolution in terms of Q^2 [197–199]. All non-perturbative effects relevant to describe the $\ell_i \to \tau$ conversion in nuclei are included in the nuclear parton distribution functions (nPDFs) that we use for this computation: the nCTEQ15-np fit of the nPDFs, provided by the group around the nCTEQ15 project [200], and incorporated within the ManeParse Mathematica package [201].

The contributions to the perturbative cross-sections come from the dimension seven operators in eq. (8.1). These bring about the following contributions:

1. the process $\ell_i q \to \tau q$ (see fig. 9.1) that involves a loop with a quark and two photons.

2. the same process as in (a), but with antiquarks: $\ell_i \bar{q} \to \tau \bar{q}$. The non-perturbative behavior of anti-quarks inside the nucleons is not the same as their opposite-charged partners, and also the perturbative cross sections of the process are different from those involving quarks.

The process $\ell_i g \to \tau g$ could also contribute to the perturbative cross-sections. By means of the operators in eq. (8.1), it would be generated at two loop level. The diagram for this contribution would be similar to the one in fig. 9.1, closing the line of quarks in a

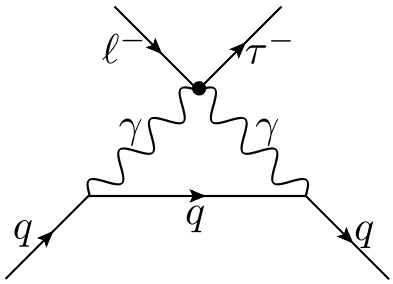

Figure 9.1: *One loop contribution to* $\ell_i q \to \tau q$*, with* $\ell_i = e, \mu$.

loop and adding the initial and final gluons coupled to the loop of quarks. Given that this process would have an additional loop suppression compared with the ones mentioned in (a) and (b), we do not include its contribution. Taking into account the contributions to the perturbative cross-section previously mentioned, we obtained the following expression of the unpolarized squared amplitude as a function of ξ and Q^2

$$\begin{aligned}\overline{|\mathcal{M}_{qq}(\xi,Q^2)|^2} = 2e^4\left(|G_{LR}^{\tau\ell}|^2+|G_{RL}^{\tau\ell}|^2\right)\left[(m_\ell^2+m_\tau^2+Q^2)\left((m_i+\xi M)^2+Q^2\right)\right]\Gamma_{qq}(\xi,Q^2)\\ +\frac{1}{2}e^4\left(|\tilde{G}_{LR}^{\tau\ell}|^2+|\tilde{G}_{RL}^{\tau\ell}|^2\right)\left[(m_\ell^2+m_\tau^2+Q^2)\left((m_i-\xi M)^2+Q^2\right)\right]\tilde{\Gamma}_{qq}(\xi,Q^2)\,,\end{aligned} \tag{9.7}$$

where $\Gamma(\xi,Q^2)$ and $\tilde{\Gamma}(\xi,Q^2)$ are the functions that result from the evaluation of the loops (see fig. 9.1), and are shown in appendix B. For the process with antiquarks, we obtain an identical expression as eq. (9.7) but with different "$\Gamma(\xi,Q^2)$" functions ($\Gamma_{\bar{q}\bar{q}}$ and $\tilde{\Gamma}_{\bar{q}\bar{q}}$). We neglect the interference term since it is always suppressed concerning the terms shown in eq. (9.7). We use Package-X [202] to analytically evaluate the loop integrals. CollierLink extends Package-X so that the Passarino-Veltman functions can be directly evaluated, using the COLLIER library [203]. Then we use CollierLink to numerically evaluate our expressions.

The perturbative unpolarized differential cross sections can be computed from the squared amplitude in eq. (9.7), leading to the result as a function of ξ and Q^2

$$\begin{aligned}\frac{d\hat{\sigma}(\ell\, q_i(\xi P)\to\tau\, q_i)}{d\xi dQ^2} &= \frac{1}{16\pi\lambda(s(\xi),m_\ell^2,m_i^2)}\overline{|\mathcal{M}_{qq}(\xi,Q^2)|^2}\,,\\ \frac{d\hat{\sigma}(\ell\,\bar{q}_i(\xi P)\to\tau\,\bar{q}_i)}{d\xi dQ^2} &= \frac{1}{16\pi\lambda(s(\xi),m_\ell^2,m_i^2)}\overline{|\mathcal{M}_{\bar{q}\bar{q}}(\xi,Q^2)|^2}\,;\end{aligned} \tag{9.8}$$

with $p_i = \xi P$ the momentum of the interacting parton and P the nucleus total momentum. We also defined $m_i^2 = \xi^2 M^2$ being M the nucleus mass. $\lambda(s(\xi),m_\ell^2,m_i^2)$ is the usual Källén function. Finally, using the leading order (LO) QCD formalism, the total cross-section

reads

$$\sigma(\ell N(P)\to\tau X)=\sum_i\int_{\xi_{\min}}^1\int_{Q^2_-(\xi)}^{Q^2_+(\xi)}d\xi dQ^2\left\{\frac{d\hat{\sigma}(\ell\, q_i(\xi P)\to\tau\, q_i)}{d\xi\, dQ^2}f_{q_i}(\xi,Q^2)\right.$$
$$\left.+\,\frac{d\hat{\sigma}(\ell\,\bar{q}_i(\xi P)\to\tau\,\bar{q}_i)}{d\xi dQ^2}f_{\bar{q}_i}(\xi,Q^2)\right\}, \tag{9.9}$$

being $f_{q_i}(\xi,Q^2)$ and $f_{\bar{q}_i}(\xi,Q^2)$ the quark and antiquark PDFs, respectively. The integration limits can be found in appendix E of ref. [184].

9.4 $\tau\to\ell\gamma\gamma$ bounds on $\ell\to\tau$ conversion

As shown in ref. [165], $\mu\to e$ conversion in nuclei binds the $\ell_i\ell_j\gamma\gamma$ effective interactions more stringently than the direct limits coming from $\ell_i\to\ell_j\gamma\gamma$ decays. In this section we will proceed analogously with the $\ell\to\tau$ conversions, looking for their potential reach in case of their discovery. We are thus interested in predicting bounds on the $\ell\to\tau$ ($\ell=e,\mu$) conversion processes and contrasting our results with the expected sensitivity of the NA64 experiment [181] and with the results in ref. [184]. Our quantity of interest will be the ratio between the conversion probabilities

$$\mathcal{R}_{\tau\ell}=\frac{\sigma(\ell\mathcal{N}\to\tau X)}{\sigma(\ell\mathcal{N}\to\ell X)}, \tag{9.10}$$

where the denominator is given by the dominant contribution to the inclusive $\ell+\mathcal{N}$ process as a result of the lepton bremsstrahlung on nuclei [181]. The most conservative expected sensitivity of the NA64 experiment is $\mathcal{R}_{\tau\ell}\sim[10^{-13},10^{-12}]$.

We defined $|G_{ij}|^2$ below eq. (9.2) as the sum of the squares of the effective couplings that appear in the Lagrangian (8.1). However, in the matrix element in eq. (9.7), we cannot factorize the effective couplings, then for the numerical analysis, we will set three benchmark scenarios:

$$\begin{aligned}
&(i)\ |G_{\tau\ell}|^2=|G^{\tau\ell}_{SR}|^2+|G^{\tau\ell}_{SL}|^2=|\tilde{G}^{\tau\ell}_{SR}|^2+|\tilde{G}^{\tau\ell}_{SL}|^2\,,\\
&(ii)\ |G_{\tau\ell}|^2=|G^{\tau\ell}_{SR}|^2+|G^{\tau\ell}_{SL}|^2;\ \tilde{G}^{\tau\ell}_{SR}=\tilde{G}^{\tau\ell}_{SL}=0\,,\\
&(iii)\ |G_{\tau\ell}|^2=|\tilde{G}^{\tau\ell}_{SR}|^2+|\tilde{G}^{\tau\ell}_{SL}|^2;\ G^{\tau\ell}_{SR}=G^{\tau\ell}_{SL}=0\,,
\end{aligned} \tag{9.11}$$

taking the upper limit on $|G_{\tau\ell}|^2$ from eqs. (9.3) [2].

[2]The running of these Wilson coefficients between the decaying lepton mass scale, that corresponds to their determination in eqs. (9.3), and the invariant mass of the nuclei conversions is neglected. Its effect will not change the conclusions of our analysis.

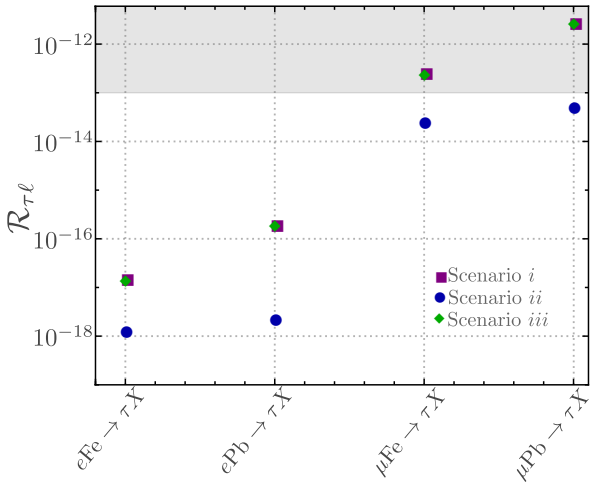

Figure 9.2: *Upper limits for the ratios* $\mathcal{R}_{\tau\ell} = \frac{\sigma(\ell\mathcal{N}\to\tau X)}{\sigma(\ell\mathcal{N}\to\ell X)}$*, obtained for* $\ell \to \tau$ *conversion in nuclei, compared to the NA64 expected sensitivity (gray band). The different scenarios are described in eq. (9.11).*

According to the prospects of the NA64 experiment [181], we use two specific nuclei in our analysis, Fe(56,26) and Pb(208,82), as well as $E_e = 100\,\mathrm{GeV}$ and $E_\mu = 150\,\mathrm{GeV}$ for the energies of the incident lepton beams [3]. To find the ratio in eq. (9.10), we need to evaluate the integral in eq. (9.9) in the three scenarios described above for $|G_{\tau\ell}|^2$. Figure 9.2 shows the ratio obtained, $\mathcal{R}_{\tau\ell}$, for the four channels explored: $e\mathrm{Fe}(56,26) \to \tau X$, $e\mathrm{Pb}(208,82) \to \tau\mathrm{X}$, $\mu\mathrm{Fe}(56,26) \to \tau X$ and $\mu\mathrm{Pb}(208,82) \to \tau\mathrm{X}$, the gray zone being the expected sensitivity of the NA64 experiment.

We calculated the integral (9.9) using light quarks only and also using light plus heavy quarks. The criterion to choose our results was the following: if the error of the calculation (due to the PDF uncertainties) using light quarks only, was larger than the contribution of the heavy quarks, then we neglected those heavy quark contributions. That is the case for scenarios (i) and (iii). Conversely, when the contribution of the heavy quarks was larger than the computation uncertainty, we included the heavy quark contributions, as in scenarios (ii). In figure 9.2, the uncertainties are not seen because they are very small and displayed on a logarithmic scale.

As we can see in figure 9.2, the $\mu \to \tau$ conversion in lead is the one most sensitive to new physics, and for the scenarios (i) and (iii) seems to be testable by the NA64 experiment. The limits coming from $e \to \tau$ conversion are much more suppressed than those from $\mu \to \tau$ conversion. We also point out that we obtain better limits for the $\mu \to \tau$ conversion in lead than in iron, in scenarios (i) and (iii). For scenario (ii), the results for both nuclei are pretty similar.

In ref. [184], Husek *et al.* also obtained more attractive results for $\mu \to \tau$ conversion

[3] The validity of our EFT in these processes is discussed in the next section.

than for the $e \to \tau$ transitions. As they nicely explain, this is due to the normalization channel in $\mathcal{R}_{\tau\ell}$ (the bremsstrahlung cross section), since it is much larger for electrons than for muons. However, the authors obtained better results for the $\mu \to \tau$ conversion in iron than in lead, while we found the opposite. In case of eventual observation, this is an interesting observation that could help elucidate the type of new physics originating these processes.

9.5 Improved limits using $\ell_i \to \ell_j \gamma$ constraints

We focus in this section on $\ell \to \tau$ transitions since S. Davison *et al.* [165] analyzed $\mu \to e$ conversions using the same operators. They computed the $\mu \to e\gamma\gamma$ decay and used the experimental limit on the BR($\mu \to e\gamma\gamma$) to constrain the Wilson coefficients of these operators. Then, they analyzed the $\mu \to e$ conversion in nuclei and found a constraint about one order of magnitude more stringent than with the bound on $\mu \to e\gamma\gamma$. However, in the previous chapter (ref. [182]), we showed that currently, the most stringent constraint on the coefficients of operators $\bar{e}\mu F_{\mu\nu}F^{\mu\nu}$ comes from the experimental bound on $\mu \to e\gamma$. Therefore, we will use this restriction to compute upper limits on the branching ratios of $\mu\text{Au} \to e\text{Au}$ and $\mu\text{Al} \to e\text{Al}$.

We consider the coherent $\mu \to e$ conversion described by the terms in the first row of eq. (8.1). The operators with $F_{\mu\nu}\tilde{F}^{\mu\nu}$ are proportional to $\vec{E} \cdot \vec{B}$, which is negligibly small in the nucleus, therefore we disregard them in the $\mu \to e$ conversion calculation. The computation of $\mu \to e$ conversion in nuclei is explained minutely in [165].

As recalled by their authors, there are two main contributions to the $\mu \to e$ conversion in nuclei. One is the interaction of the leptons with the classical electromagnetic field, and there is also a surprisingly large "short distance" loop interaction of two photons with individual protons. The first contribution arises for a contact $\mu e\gamma\gamma$ interaction at momentum transfers $\sim m_\mu$. There is another contribution stemming from the loop mixing of the $\bar{e}\mu F_{\mu\nu}F^{\mu\nu}$ operator into the scalar proton operator, $\mathcal{O}_{S,X} = (\bar{e}P_X\mu)(\bar{p}p)$ (X labeling the chirality). Overlap integrals, energy ratios, and numerical factors overcompensate for the naive expectation of a loop suppression [165].

Our results for $\bar{e}\mu F_{\mu\nu}F^{\mu\nu}$ can be included as

$$\begin{aligned}\mathrm{BR}(\mu A \to eA) = \frac{32 G_F^2 m_\mu^5}{\Gamma_{\rm cap}} \sum_{X\in\{L,R\}} \Bigg| & C_{D,X}\frac{D_A}{4} + (9.0\, C_{S,X}^{uu} + 8.2\, C_{S,X}^{dd} + 0.42\, C_{S,X}^{ss}) S_A^{(p)} \\ & + (8.1\, C_{S,X}^{uu} + 9.0\, C_{S,X}^{dd} + 0.42\, C_{S,X}^{ss}) S_A^{(n)} + \ldots \\ & - C_{GG,X}\frac{8\pi m_N}{9\alpha_s(2m_N)v}(0.90 S_A^{(p)} + 0.89 S_A^{(n)}) - G_{SX}^{\mu e} v^2 \left(m_\mu F_A + \frac{18\alpha m_p}{\pi} S_A^{(p)} \right) \Bigg|^2 \end{aligned} \tag{9.12}$$

in the ratio for spin-independent $\mu \to e$ nuclei conversion, where $\Gamma_{\rm cap}$ is the muon capture rate on nucleus A [204], D_A and $S_A^{(N)}$ are the overlap integrals inside the nucleus A, with respectively the electric field or the appropriate nucleon ($N \in \{n, p\}$) distribution, which can be found in [205]. v is the Higgs vacuum expectation value, with $2\sqrt{2}G_F = 1/v^2$. $C_{D,X}$ is the dipole coefficient, $C_{GG,X}$ is the gluon operator coefficient, $\{C_{S,X}^{qq}\}$ are the coefficients of $2\sqrt{2}G_F(\bar{e}P_X\mu)(\bar{q}q)$, and the "$+\ldots$" represents the contributions of vector operators involving a light quark bilinear. The last term in (9.12) gives the contribution of the operators $\bar{e}\mu F_{\mu\nu}F^{\mu\nu}$, at tree level via the overlap integral F_A (tabulated in Appendix B of [165]), and via one loop-mixing to the scalar proton density.

If we assume that only the $\bar{e}\mu F_{\mu\nu}F^{\mu\nu}$ operator coefficients are non-zero, this corresponds to

$$\mathrm{BR}(\mu A \to eA) = \frac{4m_\mu^5}{\Gamma_{\rm cap}}|G_{\mu e}|^2 \left(m_\mu F_A + \frac{18\alpha m_p}{\pi} S_A^{(p)} \right)^2 . \tag{9.13}$$

Using the upper limits on $|G_{\mu e}|$ from eq. (9.4) and assuming conservatively that $\Lambda = 100$ GeV, we find the upper limits on the BR(μA $\to$ eA), with A =Au(197 ,79), Al(27 ,13) are

$$\begin{aligned} \mathrm{BR}(\mu\mathrm{Au} \to \mathrm{eAu}) &\leq 2.7 \times 10^{-13}\,, \\ \mathrm{BR}(\mu\mathrm{Al} \to \mathrm{eAl}) &\leq 6.9 \times 10^{-13}\,. \end{aligned} \tag{9.14}$$

Comparing the values in eq. (9.14) with the upper limit on BR(μAu $\to$ eAu) from SINDRUM II experiment [179], we see that the new prediction sets a slightly stronger constraint. However, an improvement on $\mu \to e\gamma$, or $\mu \to e$ conversion in nuclei, will enhance the sensitivity to the effective coupling $G_{\mu e}$. We add our prediction for the μAl $\to$ eAl conversion process since the upcoming COMET [206] and Mu2e [207] experiments plan to start with an Aluminium target. The MEG II experiment will have a target sensitivity improved to $\mathcal{O}(10^{-14})$ [208], and in the long run, it is widely anticipated that $\mu \to e$ conversion in nuclei will provide the ultimate sensitivity to cLFV, with rates below $\mathcal{O}(10^{-18})$ [207,209,210] or lower. So that in the future, the best constraint on the operators

discussed, from $\mu \to e$ transitions, will come from the $\mu \to e$ conversion in nuclei.

Regarding $\ell \to \tau$ conversion, using the upper limits on $|G_{\tau\ell}|$ from eq. (9.4) and employing again $\Lambda = 100$ GeV, we evaluate the ratio $\mathcal{R}_{\tau\ell}$, for the same three scenarios described in eq. (9.11) and the same nuclei analyzed before, Fe(56,26) and Pb(208,82). We calculated the integral (9.9) as described previously and we used the same criteria to choose our results. In figure 9.3, we show the ratio obtained for the four channels explored [183], the gray zone being the expected sensitivity of the NA64.

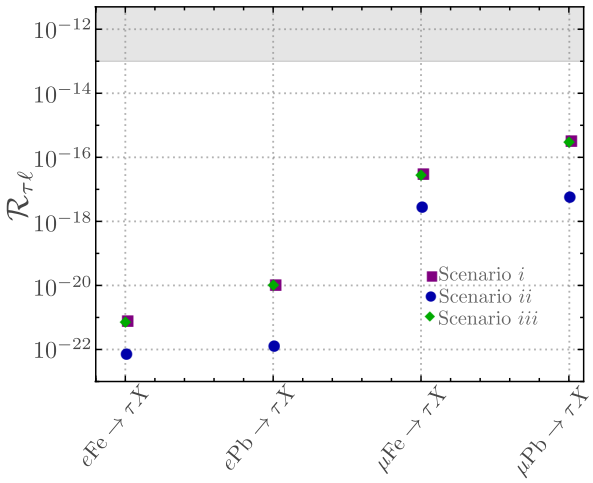

Figure 9.3: *Upper limits for the ratios* $\mathcal{R}_{\tau\ell} = \frac{\sigma(\ell 3\mathcal{N} \to \tau X)}{\sigma(\ell\mathcal{N} \to \ell X)}$. *The different scenarios are described in eq. (9.11) and the values of* $|G_{\tau\ell}|$ *come from the eqs. (9.4), assuming* $\Lambda = 100$ *GeV.*

Accordingly, in figure 9.3, the ratios have similar behavior to the ones shown in figure 9.2, being the $\mu \to \tau$ conversion in nuclei the one most sensitive to new physics. However, using the upper limits on $|G_{\tau\ell}|$ from $\tau \to \ell\gamma$, eqs. (9.4), instead of the upper bounds on $|G_{\tau\ell}|$ from $\tau \to \ell\gamma\gamma$, eqs. (9.3), our limits on $\mathcal{R}_{\tau\ell}$ are about four orders of magnitude stronger. Thus, the big improvement restricting the local interaction $\bar{\ell}_i \ell_j \gamma\gamma$, which comes from $\tau \to \ell\gamma$ [182], excludes the early observation of $\ell \to \tau$ conversions in nuclei generated by two-photon effective vertices by NA64.

Strictly speaking, one would need to study $\ell \to \tau$ conversions in nuclei using SMEFT and not our low-energy EFT. However, it is straightforward to see that:
- Our effective operators become $D = 8$ operators in the SMEFT (by inserting a Higgs doublet inside the lepton bilinear, that will now be composed of an $SU(2)_L$ doublet and a singlet), which are subleading with respect to those in ref. [184]. There will be other contributions at this order and the complete calculation is beyond our scope.
- These SMEFT operators will have additional contributions where one or both photons in the loop are replaced by a Z^0 boson. These are negligible with respect to the di-photon ones. Processes involving the Z or H bosons do not yield competitive constraints

to the $\ell_i \to \ell_j \gamma$ processes, obviously. In this way, the only remaining modification to our treatment for being in SMEFT would be the (soft) running of the Wilson coefficient from the ℓ_i to the $\sqrt{Q^2}$ scale, which will -by no means- alter our main results above (see footnote [2] in the previous section).

9.6 Conclusions

The effective operators used in this work generate charged lepton flavor violation by two-lepton two-photon vertices. We have studied their implications in $\ell \to \ell'$ conversions in nuclei, benefiting from our improved bounds on these interactions [182], coming from $\ell_i \to \ell_j \gamma$ decays. We use them to compute $\ell \to \tau$ conversion in iron and lead nuclei and find that —even in the best case (for $\mu \to \tau$ transitions in lead)— they lie three orders of magnitude below the NA64 sensitivity. For the $\mu \to e$ transitions we show that their observation in Gold within the approximate range $[3, 7] \times 10^{-13}$ would not correspond to the $\ell\ell'\gamma\gamma$ interactions studied here.

Chapter 10

Conclusions

As we have emphasized throughout this thesis, the EFT framework is a useful tool to study physics beyond the standard model. We have used EFTs to study dark matter-standard model interactions and lepton flavor violation in the charged sector. The main work in this thesis is contained in chapters 6-9.

In chapter 6 we first describe the assumptions made to derive the EFT [98] and show the Lagrangian that generates the interactions. Then we present a phenomenological analysis using observational/experimental constraints: relic density, Z invisible decay width and limits from direct and indirect detection. In this chapter we analyzed DM masses in the range from MeV to $m_Z/2$, and obtained mass intervals that comply with all the constraints. Then in chapter 7 we complement the previous work by extending the mass range analyzed and also adding collider constraints. Limits from ATLAS [151] ruled out mainly light dark matter masses, $\lesssim m_Z/2$. For several operators (and combinations of them) we found solutions that fulfill all constraints, we also ruled out some operators mainly by direct detection limits. If future experiments continue to impose increasingly restrictive limits we will be able to further restrict the parameter space in the EFT. In these chapters we assume that the total abundance of dark matter was reproduced, however we can always relax this assumption and then the parameter space allowed would be larger. Another idea that we would like to explore is the possibility of multi-component DM where the interaction with the SM is realized through only part of the dark sector, in this way we could reproduce the total dark matter relic density and still comply with the experimental constraints.

We analyzed lepton flavor violating decays in the charged sector in chapter 8 and conversion in nuclei in chapter 9. The EFT that we use consists of dimension 7 and dimension 8 operators that generate the effective $\ell_i - \ell_j\gamma\gamma$ interaction. By computing the $\ell_i \to \ell_j\gamma$ decays at one loop level, we derived indirect upper limits for the $\ell_i \to \ell_j\gamma\gamma$ decays. Our indirect limits are more restrictive than current experimental bounds. We

also discuss some possible UV-complete scenarios where the dimension-5 operators could be suppressed with respect to the dimension-7 operators, thereby enhancing the rate of $\ell_i \to \ell_j \gamma\gamma$ compared to $\ell_i \to \ell_j \gamma$. Our results motivate a dedicated experimental search for the $\tau \to \ell\gamma\gamma$ decays, since this decay might be at the reach of future experiments [175]. Finally, in chapter 9 we complement the previous chapter by computing the processes of conversion in nuclei. However we conclude that $\ell \to \tau$ conversion in nuclei is outside the scope of future foreseen experiments. Concerning $\mu \to e$ processes, currently the more stringent constraint on our dimension-7 operators comes from the experimental limit on the $\mu \to e\gamma$ decay, nevertheless an improvement on $\mu \to e$ conversion in nuclei will enhance the sensitivity in our effective coupling $G_{\mu e}$ [209].

Finally, appendix C outlines a work in progress. This work is motivated by the fact that gauge symmetry imposes tight constraints on the phenomenology of a spin-one boson χ which, by assumption, participates in LFV processes, represented by $\ell_i \to \ell_j \chi$. One immediate restriction is that the massless χ limit must be well-behaved, but there are others that depend slightly on the ultraviolet origin of the effective $\ell_i - \ell_j - \chi$ interactions. This motivates our exhaustive phenomenological analysis, which is work in progress.

Appendix A

Differential decay rates for $\ell_i \to \ell_j \gamma\gamma$

In this appendix, we present the double differential decay width for the $\ell_i \to \ell_j \gamma\gamma$ processes, including the contributions from effective operators up to dim-7. The differential rate can be cast as:

$$\frac{\mathrm{d}^2\Gamma(\ell_i \to \ell_j\gamma\gamma)}{\mathrm{d}E_\gamma \mathrm{d}E_{\gamma'}} = \frac{\mathrm{d}^2\Gamma(\ell_i \to \ell_j\gamma\gamma)}{\mathrm{d}E_\gamma \mathrm{d}E_{\gamma'}}\Big|_{\mathrm{dim}-5} + \frac{\mathrm{d}^2\Gamma(\ell_i \to \ell_j\gamma\gamma)}{\mathrm{d}E_\gamma \mathrm{d}E_{\gamma'}}\Big|_{\mathrm{dim}-7} + \frac{\mathrm{d}^2\Gamma(\ell_i \to \ell_j\gamma\gamma)}{\mathrm{d}E_\gamma \mathrm{d}E_{\gamma'}}\Big|_{\mathrm{int}}\,, \tag{A.1}$$

where in an obvious notation, dim-5 denotes the contribution from the Lagrangian eq. (8.2), dim-7 from the Lagrangian eq. (8.1), and int is the interference term. Explicitly, and neglecting the mass of the lepton in the final state, we obtain:

$$\frac{\mathrm{d}^2\Gamma(\ell_i \to \ell_j\gamma\gamma)}{\mathrm{d}E_\gamma \mathrm{d}E_{\gamma'}}\Big|_{\mathrm{dim}-7} = \frac{\left|G_{ij}\right|^2}{16\pi^3}\, m_i^2 \big(m_i - E_\gamma - E_{\gamma'}\big)\big(m_i - 2(E_\gamma + E_{\gamma'})\big)^2\,, \tag{A.2}$$

$$\begin{aligned}\frac{\mathrm{d}^2\Gamma(\ell_i \to \ell_j\gamma\gamma)}{\mathrm{d}E_\gamma \mathrm{d}E_{\gamma'}}\Big|_{\mathrm{dim}-5} &= \frac{\alpha\left(|D_R^{ij}|^2 + |D_L^{ij}|^2\right)}{4E_\gamma E_{\gamma'} + m_i^2 - 2m_i(E_\gamma + E_{\gamma'})}\frac{m_i - 2(E_\gamma + E_{\gamma'})}{4\pi^2 E_\gamma^2 E_{\gamma'}^2}\Big\{48E_\gamma^3 E_{\gamma'}^3 \\ &\quad - m_i^4\big(E_\gamma - E_{\gamma'}\big)^2 + 2E_\gamma E_{\gamma'} m_i^2\left(E_\gamma^2 + 6E_\gamma E_{\gamma'} + E_{\gamma'}^2\right) \\ &\quad - E_\gamma E_{\gamma'} m_i(E_\gamma + E_{\gamma'})\left(24E_\gamma E_{\gamma'} + m_i^2\right)\Big\}\,,\end{aligned} \tag{A.3}$$

$$\frac{\mathrm{d}^2\Gamma(\ell_i \to \ell_j\gamma\gamma)}{\mathrm{d}E_\gamma \mathrm{d}E_{\gamma'}}\Big|_{\mathrm{int}} = -\frac{e\, m_i\big(m_i - 2(E_\gamma + E_{\gamma'})\big)^2}{4\pi^3}\Re\Big\{D_L^{ij*}\left(G_{SL}^{ij} + i\tilde{G}_{SL}^{ij}\right) + D_R^{ij*}\left(G_{SR}^{ij} - i\tilde{G}_{SR}^{ij}\right)\Big\}\,, \tag{A.4}$$

with kinematical ranges for the photon energies $0 \le E_\gamma \le m_i/2$, $m_i/2 - E_\gamma \le E_{\gamma'} \le m_i/2$. Notice that the dimension-5 contribution suffers from both infrared and collinear singularities, which we can avoid by introducing a regulator such that $E_\gamma^{\mathrm{cut}} \le E_\gamma \le m_i/2 - E_\gamma^{\mathrm{cut}}$, $m/2 - E_\gamma \le E_{\gamma'} \le m_i/2 - E_\gamma^{\mathrm{cut}}$. Strictly, one should introduce different regulators, however we assume them to be the same for simplicity.

Appendix B

Functions from the evaluation of loops in $\ell \to \tau$ conversion in nuclei

We define

$$\begin{aligned}
\Gamma_{qq}(\xi, Q^2) &= \frac{1}{64\pi^4}|\mathrm{F1}(\xi, Q^2)|^2\,, \\
\tilde{\Gamma}_{qq}(\xi, Q^2) &= \frac{1}{64\pi^4}|\mathrm{F2}(\xi, Q^2)|^2\,, \\
\Gamma_{\bar{q}\bar{q}}(\xi, Q^2) &= \frac{1}{64\pi^4}|\mathrm{F3}(\xi, Q^2)|^2\,, \\
\tilde{\Gamma}_{\bar{q}\bar{q}}(\xi, Q^2) &= \frac{1}{64\pi^4}|\mathrm{F4}(\xi, Q^2)|^2\,,
\end{aligned} \tag{B.1}$$

with

$$\begin{aligned}
\mathrm{F1} = {} & 2\big[m(Q^2) + M\xi\big]\mathbf{B}_0(M^2\xi^2; m(Q^2), 0) + 2\big[m(Q^2) + m_i\big]\mathbf{B}_0(m_i^2; m(Q^2), 0) \\
& + 2\big[m(Q^2) - m_i\big]\mathbf{B}_0(-Q^2; 0, 0) + 2M\xi\,\mathbf{B}_1(M^2\xi^2; m(Q^2), 0) + 2\big[M\xi - m_i\big]\mathbf{B}_1(-Q^2; 0, 0) \\
& + 2m_i\,\mathbf{B}_1(m_i^2; m(Q^2), 0) + 2\big[m^3(Q^2) + Mm_i\,m(Q^2)\xi - M^2m_i\xi^2 + m(Q^2)Q^2 - Mm_i^2\xi\big] \\
& \mathbf{C}_0(m_i^2, -Q^2, M^2\xi^2; m(Q^2), 0, 0) + 2\big[m^2(Q^2) - m_i^2 + m_i m(Q^2) - m_i M\xi - M^2\xi^2 + Mm(Q^2)\xi\big] \\
& \big(M\xi\,\mathbf{C}_2(m_i^2, -Q^2, M^2\xi^2; m(Q^2), 0, 0) + m_i\,\mathbf{C}_1(m_i^2, -Q^2, M^2\xi^2; m(Q^2), 0, 0)\big) \\
& + m_i - 4m(Q^2) + M\xi\,.
\end{aligned} \tag{B.2}$$

$$\begin{aligned}
\mathrm{F2} = {} & -2i\Big(2\big[M\xi + m(Q^2)\big]\mathbf{B}_0(M^2\xi^2; m(Q^2), 0) + 2\big[m_i + m(Q^2)\big]\mathbf{B}_0(m_i^2; m(Q^2), 0) \\
& + 2\big[M\xi + m_i - 2m(Q^2)\big]\mathbf{B}_0(-Q^2; 0, 0) + 2M\xi\,\mathbf{B}_1(M^2\xi^2; m(Q^2), 0) + 2m_i\,\mathbf{B}_1(m_i^2; m(Q^2), 0) \\
& + 2\big[m_i m^2(Q^2) - 2m^3(Q^2) + Mm^2(Q^2)\xi - Mm_i^2\xi - M^2m_i\xi^2 + 2Mm_i m(Q^2) + m(Q^2)Q^2\big] \\
& \mathbf{C}_0(m_i^2, -Q^2, M^2\xi^2; m(Q^2), 0, 0) + 2\big[m_i^2 - 2m_i m(Q^2) - M^2\xi^2 + 2Mm(Q^2)\xi\big] \\
& \big(m_i\,\mathbf{C}_1(m_i^2, -Q^2, M^2\xi^2; m(Q^2), 0, 0) - M\xi\,\mathbf{C}_2(m_i^2, -Q^2, M^2\xi^2; m(Q^2), 0, 0)\big) \\
& - 3(m_i + M\xi)\Big).
\end{aligned} \tag{B.3}$$

$$
\begin{aligned}
\mathrm{F3} = {} & 2\big[m(Q^2) - M\xi\big]\mathbf{B}_0(M^2\xi^2; m(Q^2), 0) + 2\big[m(Q^2) - m_i\big]\mathbf{B}_0(m_i^2; m(Q^2), 0) \\
& + 2\big[m(Q^2) + m_i\big]\mathbf{B}_0(-Q^2; 0, 0) - 2M\xi\,\mathbf{B}_1(M^2\xi^2; m(Q^2), 0) - 2m_i\,\mathbf{B}_1(m_i^2; m(Q^2), 0) \\
& + 2\big[m_i - M\xi\big]\mathbf{B}_1(-Q^2; 0, 0) + 2\big[M^2\xi^2 + m_i\big(M\xi + m(Q^2)\big) + Mm(Q^2)\xi + m_i^2 - m^2(Q^2)\big] \\
& \big(M\xi\,\mathbf{C}_2(m_i^2, -Q^2, M^2\xi^2; m(Q^2), 0, 0) + m_i\,\mathbf{C}_1(m_i^2, -Q^2, M^2\xi^2; m(Q^2), 0, 0)\big) \\
& + 2\big[m^3(Q^2) + Mm_i m(Q^2)\xi + M^2 m_i\xi^2 + m(Q^2)Q^2 + Mm_i^2\xi\big]\mathbf{C}_0(m_i^2, -Q^2, M^2\xi^2; m(Q^2), 0, 0) \\
& - \big(m_i + 4m(Q^2) + M\xi\big).
\end{aligned}
\tag{B.4}
$$

$$
\begin{aligned}
\mathrm{F4} = {} & 2i\Big(2\big[M\xi - m(Q^2)\big]\mathbf{B}_0(M^2\xi^2; m(Q^2), 0) + 2\big[m_i - m(Q^2)\big]\mathbf{B}_0(m_i^2; m(Q^2), 0) \\
& + 2\big[m_i + 2m(Q^2) + M\xi\big]\mathbf{B}_0(-Q^2; 0, 0) + 2m_i\,\mathbf{B}_1(m_i^2; m(Q^2), 0) + 2M\xi\,\mathbf{B}_1(M^2\xi^2; m(Q^2), 0) \\
& + 2\big[2m^3(Q^2) + m_i m^2(Q^2) + M\xi m^2(Q^2) - M\xi m_i^2 - M^2\xi^2 m_i - 2M\xi m_i m(Q^2) - m(Q^2)Q^2\big] \\
& \mathbf{C}_0(m_i^2, -Q^2, M^2\xi^2; m(Q^2), 0, 0) + 2\big[2m_i m(Q^2) - M^2\xi^2 - 2M\xi\,m(Q^2) + m_i^2\big] \\
& \big(m_i\,\mathbf{C}_1(m_i^2, -Q^2, M^2\xi^2; m(Q^2), 0, 0) - M\xi\,\mathbf{C}_2(m_i^2, -Q^2, M^2\xi^2; m(Q^2), 0, 0)\big) \\
& - 3(m_i + M\xi)\Big).
\end{aligned}
\tag{B.5}
$$

The function $m(Q^2)$ represents the running of the quark mass in the loop (see fig. 9.1). For the computation of the quark masses at different energy scales, we use RunDec [211]. The notation employed for the Passarino-Veltman loop functions is standard.

Appendix C

Phenomenology of LFV decays including a spin-one boson

We will finish outlining a work in progress. It is based on the ideas developed in ref. [212], further extended in ref. [213] [1].

This work is motivated by the fact that gauge symmetry imposes tight constraints on the phenomenology of a spin-one boson χ which, by assumption, participates in LFV processes, represented by $\ell_i \to \ell_j \chi$. One immediate restriction is that the massless χ limit must be well-behaved, but there are others that depend slightly on the ultraviolet origin of the effective $\ell_i - \ell_j - \chi$ interactions.

In ref. [212] simple tree-level and one-loop realizations of these effective vertices were considered. In the first case only interactions of monopole type ($\propto \bar{\ell}_i \gamma^\mu (\gamma_5) \chi_\mu \ell_j$+h.c.) were found. The corresponding form factors showed the leading dependence $\propto \frac{m_\chi}{m_i}$ on particle masses. The one-loop case is richer as again monopole-type form factors are found (now scaling as $\frac{m_\chi^2}{\Lambda^2}$, with Λ the NP scale suppressing operators of dimension higher than four), but this time also dipole ones appear ($\propto \bar{\ell}_i \sigma^{\mu\nu} (\gamma_5) \chi_{\mu\nu} \ell_j$+h.c.), where now $\chi_{\mu\nu}$ is the Abelian field-strength tensor associated to the $U(1)$ gauge symmetry (with corresponding boson χ). The latter form factors exhibit the parametric dependence $\propto \frac{m_i^2}{\Lambda^2}$. We note that in this one-loop case the dependence on Λ contradicts naive dimensional analysis (both monopole and dipole operators are suppressed as Λ^{-2}). Indeed, given their dependence on light masses, the dipole operators will dominate for light χ.

In our work we consider first the processes with an on-shell χ, namely $\ell_i \to \ell_j \chi$; and

[1] See also Marcela Marín's talk at TAU2021, available at https://indico.cern.ch/event/848732/contributions/4524316 .

then those mediated by a virtual χ: $\ell_i \to \ell_j \ell_k \ell_k$ (where some final-state ℓ needs to be $\bar{\ell}$), $\ell_i \to \ell_j$ conversion in nuclei and muonium-antimuonium transitions, mainly. We will do this using the Lagrangian (M stands for monopole and D for dipole)

$$\mathcal{L} = f^M_{e\mu} \bar{e} \gamma^\alpha \chi_\alpha \mu + g^M_{e\mu} \bar{e} \gamma^\alpha \gamma_5 \chi_\alpha \mu + f^D_{e\mu} \bar{e} \sigma^{\alpha\beta} \chi_{\alpha\beta} \mu + g^D_{e\mu} \bar{e} \sigma^{\alpha\beta} \gamma_5 \chi_{\alpha\beta} \mu + h.c., \tag{C.1}$$

with trivial generalizations for the three-flavor case, and the form factors scaling as indicated previously. Our results will be presented elsewhere.

Bibliography

[1] S. L. Glashow, *Partial Symmetries of Weak Interactions*, *Nucl. Phys.* **22** (1961) 579–588.

[2] A. Salam, *Weak and Electromagnetic Interactions*, *Conf. Proc. C* **680519** (1968) 367–377.

[3] S. Weinberg, *A Model of Leptons*, *Phys. Rev. Lett.* **19** (1967) 1264–1266.

[4] W. Buchmuller and D. Wyler, *Effective Lagrangian Analysis of New Interactions and Flavor Conservation*, *Nucl. Phys. B* **268** (1986) 621–653.

[5] B. Grzadkowski, M. Iskrzynski, M. Misiak and J. Rosiek, *Dimension-Six Terms in the Standard Model Lagrangian*, *JHEP* **10** (2010) 085, [1008.4884].

[6] T. Appelquist and J. Carazzone, *Infrared Singularities and Massive Fields*, *Phys. Rev. D* **11** (1975) 2856.

[7] P. W. Higgs, *Broken Symmetries and the Masses of Gauge Bosons*, *Phys. Rev. Lett.* **13** (1964) 508–509.

[8] F. Englert and R. Brout, *Broken Symmetry and the Mass of Gauge Vector Mesons*, *Phys. Rev. Lett.* **13** (1964) 321–323.

[9] A. Pich, *The Standard Model of Electroweak Interactions*, in *2010 European School of High Energy Physics*, pp. 1–50, 1, 2012, 1201.0537.

[10] Y. Kuno and Y. Okada, *Muon decay and physics beyond the standard model*, *Rev. Mod. Phys.* **73** (2001) 151–202, [hep-ph/9909265].

[11] N. Cabibbo, *Unitary Symmetry and Leptonic Decays*, *Phys. Rev. Lett.* **10** (1963) 531–533.

[12] M. Kobayashi and T. Maskawa, *CP Violation in the Renormalizable Theory of Weak Interaction*, *Prog. Theor. Phys.* **49** (1973) 652–657.

[13] SNO collaboration, Q. R. Ahmad et al., *Direct evidence for neutrino flavor transformation from neutral current interactions in the Sudbury Neutrino Observatory*, *Phys. Rev. Lett.* **89** (2002) 011301, [nucl-ex/0204008].

[14] Super-Kamiokande collaboration, Y. Fukuda et al., *Evidence for oscillation of atmospheric neutrinos*, *Phys. Rev. Lett.* **81** (1998) 1562–1567, [hep-ex/9807003].

[15] KamLAND collaboration, K. Eguchi et al., *First results from KamLAND: Evidence for reactor anti-neutrino disappearance*, *Phys. Rev. Lett.* **90** (2003) 021802, [hep-ex/0212021].

[16] Borexino collaboration, C. Arpesella et al., *First real time detection of Be-7 solar neutrinos by Borexino*, *Phys. Lett. B* **658** (2008) 101–108, [0708.2251].

[17] MINOS collaboration, P. Adamson et al., *Measurement of Neutrino and Antineutrino Oscillations Using Beam and Atmospheric Data in MINOS*, *Phys. Rev. Lett.* **110** (2013) 251801, [1304.6335].

[18] Z. Maki, M. Nakagawa and S. Sakata, *Remarks on the unified model of elementary particles*, *Prog. Theor. Phys.* **28** (1962) 870–880.

[19] B. Pontecorvo, *Inverse beta processes and nonconservation of lepton charge*, *Zh. Eksp. Teor. Fiz.* **34** (1957) 247.

[20] P. F. de Salas, D. V. Forero, S. Gariazzo, P. Martínez-Miravé, O. Mena, C. A. Ternes et al., *2020 global reassessment of the neutrino oscillation picture*, *JHEP* **02** (2021) 071, [2006.11237].

[21] Particle Data Group collaboration, R. L. Workman and Others, *Review of Particle Physics*, *PTEP* **2022** (2022) 083C01.

[22] G. Bertone and D. Hooper, *History of dark matter*, *Rev. Mod. Phys.* **90** (2018) 045002, [1605.04909].

[23] F. Zwicky, *Die Rotverschiebung von extragalaktischen Nebeln*, *Helv. Phys. Acta* **6** (1933) 110–127.

[24] M. Schwarzschild, *Mass distribution and mass-luminosity ratio in galaxies*, **59** (Sept., 1954) 273.

[25] H. J. Rood, *The Dynamics of the Coma Cluster of Galaxies.*, Ph.D. thesis, University of Michigan, Jan., 1965.

[26] S. D. M. White, *Mass segregation and missing mass in the Coma cluster*, *Monthly Notices of the Royal Astronomical Society* **179** (06, 1977) 33–41.

[27] J. Meekins et al., *X-rays from the Coma Cluster of Galaxies*, *Nature* **231** (05, 1971) 107–108.

[28] F. D. Kahn and L. Woltjer, *Intergalactic Matter and the Galaxy.*, **130** (Nov., 1959) 705.

[29] V. C. Rubin and J. Ford, W. Kent, *Rotation of the Andromeda Nebula from a Spectroscopic Survey of Emission Regions*, **159** (Feb., 1970) 379.

[30] K. C. Freeman, *On the Disks of Spiral and S0 Galaxies*, **160** (June, 1970) 811.

[31] D. H. Rogstad and G. S. Shostak, *Gross Properties of Five Scd Galaxies as Determined from 21-CENTIMETER Observations*, **176** (Sept., 1972) 315.

[32] M. S. Roberts and A. H. Rots, *Comparison of Rotation Curves of Different Galaxy Types*, **26** (Aug., 1973) 483–485.

[33] V. C. Rubin, *A brief history of dark matter*, p. 1–13. Space Telescope Science Institute Symposium Series. Cambridge University Press, 2004. 10.1017/CBO9780511536298.003.

[34] A. Bosma, *The distribution and kinematics of neutral hydrogen in spiral galaxies of various morphological types*, Ph.D. thesis, University of Groningen, Netherlands, Mar., 1978.

[35] V. C. Rubin, J. Ford, W. K. and N. Thonnard, *Extended rotation curves of high-luminosity spiral galaxies. IV. Systematic dynamical properties, Sa -¿ Sc.*, **225** (Nov., 1978) L107–L111.

[36] S. M. Faber and J. S. Gallagher, *Masses and mass-to-light ratios of galaxies.*, **17** (Jan., 1979) 135–187.

[37] P. J. E. Peebles, *Primeval adiabatic perturbations - Effect of massive neutrinos*, **258** (July, 1982) 415–424.

[38] D. N. Schramm and G. Steigman, *Relic Neutrinos and the Density of the Universe*, **243** (Jan., 1981) 1.

[39] M. Davis, J. Huchra, D. W. Latham and J. Tonry, *A survey of galaxy redshifts. II. The large scale space distribution.*, **253** (Feb., 1982) 423–445.

[40] S. D. M. White, C. S. Frenk and M. Davis, *Clustering in a neutrino-dominated universe*, **274** (Nov., 1983) L1–L5.

[41] Planck collaboration, N. Aghanim et al., *Planck 2018 results. VI. Cosmological parameters*, *Astron. Astrophys.* **641** (2020) A6, [1807.06209].

[42] WMAP collaboration, G. Hinshaw et al., *Nine-Year Wilkinson Microwave Anisotropy Probe (WMAP) Observations: Cosmological Parameter Results*, *Astrophys. J. Suppl.* **208** (2013) 19, [1212.5226].

[43] A. Finzi and F. A. E. Pirani, *On the Validity of Newton's Law at a Long Distance*, *Monthly Notices of the Royal Astronomical Society* **127** (12, 1963) 21–30, [https://academic.oup.com/mnras/article-pdf/127/1/21/8078411/mnras127-0021.pdf].

[44] P. J. E. Peebles, *Large-scale background temperature and mass fluctuations due to scale-invariant primeval perturbations*, **263** (Dec., 1982) L1–L5.

[45] A. J. Benson, A. Farahi, S. Cole, L. A. Moustakas, A. Jenkins, M. Lovell et al., *Dark Matter Halo Merger Histories Beyond Cold Dark Matter: I - Methods and Application to Warm Dark Matter*, *Mon. Not. Roy. Astron. Soc.* **428** (2013) 1774, [1209.3018].

[46] M. R. Lovell, C. S. Frenk, V. R. Eke, A. Jenkins, L. Gao and T. Theuns, *The properties of warm dark matter haloes*, *Mon. Not. Roy. Astron. Soc.* **439** (2014) 300–317, [1308.1399].

[47] R. Kennedy, C. Frenk, S. Cole and A. Benson, *Constraining the warm dark matter particle mass with Milky Way satellites*, *Mon. Not. Roy. Astron. Soc.* **442** (2014) 2487–2495, [1310.7739].

[48] S. D. McDermott, H.-B. Yu and K. M. Zurek, *Turning off the Lights: How Dark is Dark Matter?*, *Phys. Rev. D* **83** (2011) 063509, [1011.2907].

[49] F. J. Sanchez-Salcedo, E. Martinez-Gomez and J. Magana, *On the fraction of dark matter in charged massive particles (CHAMPs)*, *JCAP* **02** (2010) 031, [1002.3145].

[50] D. Clowe, M. Bradac, A. H. Gonzalez, M. Markevitch, S. W. Randall, C. Jones et al., *A direct empirical proof of the existence of dark matter*, *Astrophys. J.* **648** (2006) L109–L113, [astro-ph/0608407].

[51] Fermi-LAT collaboration, M. Ackermann et al., *Searching for Dark Matter Annihilation from Milky Way Dwarf Spheroidal Galaxies with Six Years of Fermi Large Area Telescope Data*, *Phys. Rev. Lett.* **115** (2015) 231301, [1503.02641].

[52] Fermi-LAT collaboration, M. Ackermann et al., *The Fermi Galactic Center GeV Excess and Implications for Dark Matter*, *Astrophys. J.* **840** (2017) 43, [1704.03910].

[53] AMS collaboration, M. Aguilar et al., *The Alpha Magnetic Spectrometer (AMS) on the international space station: Part II — Results from the first seven years*, *Phys. Rept.* **894** (2021) 1–116.

[54] CTA Consortium collaboration, B. S. Acharya et al., *Science with the Cherenkov Telescope Array*. WSP, 11, 2018, 10.1142/10986.

[55] H.E.S.S. collaboration, H. Abdallah et al., *Search for dark matter annihilations towards the inner Galactic halo from 10 years of observations with H.E.S.S*, *Phys. Rev. Lett.* **117** (2016) 111301, [1607.08142].

[56] G. Arcadi, M. Dutra, P. Ghosh, M. Lindner, Y. Mambrini, M. Pierre et al., *The waning of the WIMP? A review of models, searches, and constraints*, *Eur. Phys. J. C* **78** (2018) 203, [1703.07364].

[57] M. Regis, *Particle Dark Matter: The State of the art*, 1008.0506.

[58] J. L. Feng, *The WIMP Paradigm: Theme and Variations*, in *Les Houches summer school on Dark Matter*, 12, 2022, 2212.02479.

[59] S. Bhattacharya and J. Wudka, *Effective theories with dark matter applications*, *Int. J. Mod. Phys. D* **30** (2021) 2130004, [2104.01788].

[60] S. L. Glashow, J. Iliopoulos and L. Maiani, *Weak Interactions with Lepton-Hadron Symmetry*, *Phys. Rev. D* **2** (1970) 1285–1292.

[61] L. Calibbi and G. Signorelli, *Charged Lepton Flavour Violation: An Experimental and Theoretical Introduction*, *Riv. Nuovo Cim.* **41** (2018) 71–174, [1709.00294].

[62] A. Blondel et al., *Research Proposal for an Experiment to Search for the Decay $\mu \to eee$*, 1301.6113.

[63] MEG II collaboration, A. M. Baldini et al., *The design of the MEG II experiment*, *Eur. Phys. J. C* **78** (2018) 380, [1801.04688].

[64] Belle-II collaboration, W. Altmannshofer et al., *The Belle II Physics Book*, *PTEP* **2019** (2019) 123C01, [1808.10567].

[65] J. Dreitlein and H. Primakoff, *Possible neutrinoless decay modes of the muon*, *Phys. Rev.* **126** (Apr, 1962) 375–378.

[66] J. D. Bowman, T. P. Cheng, L.-F. Li and H. S. Matis, *New Upper Limit for mu –> e gamma gamma*, *Phys. Rev. Lett.* **41** (1978) 442–445.

[67] D. A. Bryman, S. Ito and R. Shrock, *Upper limits on branching ratios of the lepton-flavor-violating decays $\tau \to \ell\gamma\gamma$ and $\tau \to \ell X$*, *Phys. Rev. D* **104** (2021) 075032, [2106.02451].

[68] T. P. Cheng and L. F. Li, *Gauge theory of elementary particle physics*. Oxford University Press, Oxford, UK, 1984.

[69] S. T. Petcov, *The Processes $\mu \to e + \gamma, \mu \to e + \overline{e}, \nu' \to \nu + \gamma$ in the Weinberg-Salam Model with Neutrino Mixing*, *Sov. J. Nucl. Phys.* **25** (1977) 340.

[70] S. M. Bilenky, S. T. Petcov and B. Pontecorvo, *Lepton Mixing, mu –> e + gamma Decay and Neutrino Oscillations*, *Phys. Lett. B* **67** (1977) 309.

[71] T. P. Cheng and L.-F. Li, *Neutrino Masses, Mixings and Oscillations in SU(2) x U(1) Models of Electroweak Interactions*, *Phys. Rev. D* **22** (1980) 2860.

[72] J. I. Illana and T. Riemann, *Charged lepton flavor violation from massive neutrinos in Z decays*, *Phys. Rev. D* **63** (2001) 053004, [hep-ph/0010193].

[73] E. Arganda, A. M. Curiel, M. J. Herrero and D. Temes, *Lepton flavor violating Higgs boson decays from massive seesaw neutrinos*, *Phys. Rev. D* **71** (2005) 035011, [hep-ph/0407302].

[74] G. Hernández-Tomé, G. López Castro and P. Roig, *Flavor violating leptonic decays of τ and μ leptons in the Standard Model with massive neutrinos*, *Eur. Phys. J. C* **79** (2019) 84, [1807.06050].

[75] P. Blackstone, M. Fael and E. Passemar, *$\tau \to \mu\mu\mu$ at a rate of one out of 10^{14} tau decays?*, *Eur. Phys. J. C* **80** (2020) 506, [1912.09862].

[76] P. Minkowski, *$\mu \to e\gamma$ at a Rate of One Out of 10^9 Muon Decays?*, *Phys. Lett. B* **67** (1977) 421–428.

[77] M. Gell-Mann, P. Ramond and R. Slansky, *Complex Spinors and Unified Theories*, *Conf. Proc. C* **790927** (1979) 315–321, [1306.4669].

[78] R. N. Mohapatra and G. Senjanovic, *Neutrino Mass and Spontaneous Parity Nonconservation*, *Phys. Rev. Lett.* **44** (1980) 912.

[79] R. N. Mohapatra and J. W. F. Valle, *Neutrino Mass and Baryon Number Nonconservation in Superstring Models*, *Phys. Rev. D* **34** (1986) 1642.

[80] J. Bernabeu, A. Santamaria, J. Vidal, A. Mendez and J. W. F. Valle, *Lepton Flavor Nonconservation at High-Energies in a Superstring Inspired Standard Model*, *Phys. Lett. B* **187** (1987) 303–308.

[81] M. Malinsky, J. C. Romao and J. W. F. Valle, *Novel supersymmetric SO(10) seesaw mechanism*, *Phys. Rev. Lett.* **95** (2005) 161801, [hep-ph/0506296].

[82] G. Hernández-Tomé, J. I. Illana, M. Masip, G. López Castro and P. Roig, *Effects of heavy Majorana neutrinos on lepton flavor violating processes*, *Phys. Rev. D* **101** (2020) 075020, [1912.13327].

[83] I. Pacheco and P. Roig, *Lepton flavor violation in the Littlest Higgs Model with T parity realizing an inverse seesaw*, *JHEP* **02** (2022) 054, [2110.03711].

[84] I. Pacheco and P. Roig, *Lepton flavour violation in hadron decays of the tau lepton within the littlest Higgs model with T-parity*, *JHEP* **09** (2022) 144, [2207.04085].

[85] E. P. Hincks and B. Pontecorvo, *Search for gamma-radiation in the 2.2-microsecond meson decay process*, *Phys. Rev.* **73** (1948) 257–258.

[86] T. Prokscha, E. Morenzoni, K. Deiters, F. Foroughi, D. George, R. Kobler et al., *The new muE4 beam at PSI: A hybrid-type large acceptance channel for the generation of a high intensity surface-muon beam*, *Nucl. Instrum. Meth. A* **595** (2008) 317–331.

[87] R. D. Bolton et al., *Search for Rare Muon Decays with the Crystal Box Detector*, *Phys. Rev. D* **38** (1988) 2077.

[88] MEGA collaboration, M. L. Brooks et al., *New limit for the family number nonconserving decay mu+ —> e+ gamma*, *Phys. Rev. Lett.* **83** (1999) 1521–1524, [hep-ex/9905013].

[89] MEG collaboration, A. M. Baldini et al., *Search for the lepton flavour violating decay $\mu^+ \to e^+\gamma$ with the full dataset of the MEG experiment*, *Eur. Phys. J. C* **76** (2016) 434, [1605.05081].

[90] M. Ardu and G. Pezzullo, *Introduction to Charged Lepton Flavor Violation*, *Universe* **8** (2022) 299, [2204.08220].

[91] S. Weinberg, *Phenomenological Lagrangians*, *Physica A* **96** (1979) 327–340.

[92] A. Pich, *Effective field theory: Course*, in *Les Houches Summer School in Theoretical Physics, Session 68: Probing the Standard Model of Particle Interactions*, pp. 949–1049, 6, 1998, hep-ph/9806303.

[93] G. Belanger, F. Boudjema, A. Pukhov and A. Semenov, *Dark matter direct detection rate in a generic model with micrOMEGAs 2.2*, *Comput. Phys. Commun.* **180** (2009) 747–767, [0803.2360].

[94] J. Goodman, M. Ibe, A. Rajaraman, W. Shepherd, T. M. P. Tait and H.-B. Yu, *Constraints on Dark Matter from Colliders*, *Phys. Rev.* **D82** (2010) 116010, [1008.1783].

[95] A. Crivellin and U. Haisch, *Dark matter direct detection constraints from gauge bosons loops*, *Phys. Rev.* **D90** (2014) 115011, [1408.5046].

[96] A. Crivellin, F. D'Eramo and M. Procura, *New Constraints on Dark Matter Effective Theories from Standard Model Loops*, *Phys. Rev. Lett.* **112** (2014) 191304, [1402.1173].

[97] M. Duch, B. Grzadkowski and J. Wudka, *Classification of effective operators for interactions between the Standard Model and dark matter*, *JHEP* **05** (2015) 116, [1412.0520].

[98] V. Macías-González and J. Wudka, *Effective theories for dark matter interactions and the neutrino portal paradigm*, *Journal of High Energy Physics* (07, 2015) .

[99] G. Arcadi, Y. Mambrini and F. Richard, *Z-portal dark matter*, *JCAP* **03** (2015) 018, [1411.2985].

[100] G. Arcadi, A. Djouadi and M. Raidal, *Dark Matter through the Higgs portal*, 1903.03616.

[101] N. Cosme, L. Lopez Honorez and M. H. G. Tytgat, *Leptogenesis and dark matter related?*, *Phys. Rev.* **D72** (2005) 043505, [hep-ph/0506320].

[102] H. An, S.-L. Chen, R. N. Mohapatra and Y. Zhang, *Leptogenesis as a Common Origin for Matter and Dark Matter*, *JHEP* **03** (2010) 124, [0911.4463].

[103] A. Falkowski, J. Juknevich and J. Shelton, *Dark Matter Through the Neutrino Portal*, 0908.1790.

[104] M. Lindner, A. Merle and V. Niro, *Enhancing Dark Matter Annihilation into Neutrinos*, *Phys. Rev.* **D82** (2010) 123529, [1005.3116].

[105] Y. Farzan, *Flavoring Monochromatic Neutrino Flux from Dark Matter Annihilation*, *JHEP* **02** (2012) 091, [1111.1063].

[106] A. Falkowski, J. T. Ruderman and T. Volansky, *Asymmetric Dark Matter from Leptogenesis*, *JHEP* **05** (2011) 106, [1101.4936].

[107] J. Heeck and H. Zhang, *Exotic Charges, Multicomponent Dark Matter and Light Sterile Neutrinos*, *JHEP* **05** (2013) 164, [1211.0538].

[108] S. Baek, P. Ko and W.-I. Park, *Singlet Portal Extensions of the Standard Seesaw Models to a Dark Sector with Local Dark Symmetry*, *JHEP* **07** (2013) 013, [1303.4280].

[109] I. Baldes, N. F. Bell, A. J. Millar and R. R. Volkas, *Asymmetric Dark Matter and CP Violating Scatterings in a UV Complete Model*, *JCAP* **1510** (2015) 048, [1506.07521].

[110] V. González-Macías, J. I. Illana and J. Wudka, *A realistic model for Dark Matter interactions in the neutrino portal paradigm*, *JHEP* **05** (2016) 171, [1601.05051].

[111] B. Batell, T. Han and B. Shams Es Haghi, *Indirect Detection of Neutrino Portal Dark Matter*, *Phys. Rev.* **D97** (2018) 095020, [1704.08708].

[112] S. HajiSadeghi, S. Smolenski and J. Wudka, *Asymmetric dark matter with a possible Bose-Einstein condensate*, *Phys. Rev.* **D99** (2019) 023514, [1709.00436].

[113] P. Bandyopadhyay, E. J. Chun, R. Mandal and F. S. Queiroz, *Scrutinizing Right-Handed Neutrino Portal Dark Matter With Yukawa Effect*, *Phys. Lett.* **B788** (2019) 530–534, [1807.05122].

[114] A. Berlin and N. Blinov, *Thermal neutrino portal to sub-MeV dark matter*, *Phys. Rev.* **D99** (2019) 095030, [1807.04282].

[115] M. Blennow, E. Fernandez-Martinez, A. Olivares-Del Campo, S. Pascoli, S. Rosauro-Alcaraz and A. V. Titov, *Neutrino Portals to Dark Matter*, *Eur. Phys. J.* **C79** (2019) 555, [1903.00006].

[116] E. Hall, T. Konstandin, R. McGehee and H. Murayama, *Asymmetric Matters from a Dark First-Order Phase Transition*, 1911.12342.

[117] E. Hall, T. Konstandin, R. McGehee, H. Murayama and G. Servant, *Baryogenesis From a Dark First-Order Phase Transition*, *JHEP* **04** (2020) 042, [1910.08068].

[118] M. T. et al. (Particle Data Group)*Phys. Rev. D* **98** (2018) .

[119] XENON collaboration, E. Aprile et al., *Dark Matter Search Results from a One Ton-Year Exposure of XENON1T*, *Phys. Rev. Lett.* **121** (2018) 111302, [1805.12562].

[120] PandaX-II collaboration, X. Ren et al., *Constraining Dark Matter Models with a Light Mediator at the PandaX-II Experiment*, *Phys. Rev. Lett.* **121** (2018) 021304, [1802.06912].

[121] LUX collaboration, D. S. Akerib et al., *Results of a Search for Sub-GeV Dark Matter Using 2013 LUX Data*, *Phys. Rev. Lett.* **122** (2019) 131301, [1811.11241].

[122] DarkSide collaboration, P. Agnes et al., *Constraints on Sub-GeV Dark-Matter–Electron Scattering from the DarkSide-50 Experiment*, *Phys. Rev. Lett.* **121** (2018) 111303, [1802.06998].

[123] CRESST collaboration, A. H. Abdelhameed et al., *First results from the CRESST-III low-mass dark matter program*, *Phys. Rev.* **D100** (2019) 102002, [1904.00498].

[124] Fermi-LAT, DES collaboration, A. Drlica-Wagner et al., *Search for Gamma-Ray Emission from DES Dwarf Spheroidal Galaxy Candidates with Fermi-LAT Data*, *Astrophys. J.* **809** (2015) L4, [1503.02632].

[125] A. Ibarra, A. S. Lamperstorfer and J. Silk, *Dark matter annihilations and decays after the AMS-02 positron measurements*, *Phys. Rev.* **D89** (2014) 063539, [1309.2570].

[126] AMS collaboration, L. Accardo et al., *High Statistics Measurement of the Positron Fraction in Primary Cosmic Rays of 0.5–500 GeV with the Alpha Magnetic Spectrometer on the International Space Station*, *Phys. Rev. Lett.* **113** (2014) 121101.

[127] D. H. Gianfranco Bertone and J. Silk, *Particle dark matter: evidence, candidates and constrains*, *Physics Reports* **405** (Jan., 2005) 279–390.

[128] J. L. Feng, *Dark Matter Candidates from Particle Physics and Methods of Detection*, *Ann. Rev. Astron. Astrophys.* **48** (2010) 495–545, [1003.0904].

[129] D. Racco, A. Wulzer and F. Zwirner, *Robust collider limits on heavy-mediator Dark Matter*, *JHEP* **05** (2015) 009, [1502.04701].

[130] N. F. Bell, Y. Cai, J. B. Dent, R. K. Leane and T. J. Weiler, *Dark matter at the LHC: Effective field theories and gauge invariance*, *Phys. Rev.* **D92** (2015) 053008, [1503.07874].

[131] A. De Simone and T. Jacques, *Simplified models vs. effective field theory approaches in dark matter searches*, *Eur. Phys. J.* **C76** (2016) 367, [1603.08002].

[132] Q.-H. Cao, C.-R. Chen, C. S. Li and H. Zhang, *Effective Dark Matter Model: Relic density, CDMS II, Fermi LAT and LHC*, *JHEP* **08** (2011) 018, [0912.4511].

[133] K. Cheung, P.-Y. Tseng, Y.-L. S. Tsai and T.-C. Yuan, *Global Constraints on Effective Dark Matter Interactions: Relic Density, Direct Detection, Indirect Detection, and Collider*, *JCAP* **1205** (2012) 001, [1201.3402].

[134] G. Busoni, A. De Simone, E. Morgante and A. Riotto, *On the Validity of the Effective Field Theory for Dark Matter Searches at the LHC*, *Phys. Lett.* **B728** (2014) 412–421, [1307.2253].

[135] O. Buchmueller, M. J. Dolan, S. A. Malik and C. McCabe, *Characterising dark matter searches at colliders and direct detection experiments: Vector mediators*, *JHEP* **01** (2015) 037, [1407.8257].

[136] B. Patt and F. Wilczek, *Higgs-field portal into hidden sectors*, hep-ph/0605188.

[137] J. M. Lamprea, E. Peinado, S. Smolenski and J. Wudka, *Strongly Interacting Neutrino Portal Dark Matter*, 1906.02340.

[138] L. Okun, *LIMITS OF ELECTRODYNAMICS: PARAPHOTONS?*, *Sov. Phys. JETP* **56** (1982) 502.

[139] B. Holdom, *Two U(1)'s and Epsilon Charge Shifts*, *Phys. Lett. B* **166** (1986) 196–198.

[140] P. Janot and S. Jadach, *Improved Bhabha cross section at LEP and the number of light neutrino species*, *Phys. Lett. B* **803** (2020) 135319, [1912.02067].

[141] G. Bélanger, F. Boudjema, A. Pukhov and A. Semenov, *micrOMEGAs4.1: two dark matter candidates*, *Comput. Phys. Commun.* **192** (2015) 322–329, [1407.6129].

[142] M. T. et al. (Particle Data Group)*Phys. Rev. D* **98** (2019) .

[143] DarkSide collaboration, P. Agnes et al., *Low-Mass Dark Matter Search with the DarkSide-50 Experiment*, *Phys. Rev. Lett.* **121** (2018) 081307, [1802.06994].

[144] F. Fortuna, P. Roig and J. Wudka, *Effective field theory analysis of dark matter-standard model interactions with spin one mediators*, *JHEP* **02** (2021) 223, [2008.10609].

[145] G. Steigman, B. Dasgupta and J. F. Beacom, *Precise relic wimp abundance and its impact on searches for dark matter annihilation*, *Phys. Rev. D* **86** (Jul, 2012) 023506.

[146] L. Bergstrom, T. Bringmann, I. Cholis, D. Hooper and C. Weniger, *New Limits on Dark Matter Annihilation from AMS Cosmic Ray Positron Data*, *Phys. Rev. Lett.* **111** (2013) 171101, [1306.3983].

[147] F. Donato, N. Fornengo, D. Maurin and P. Salati, *Antiprotons in cosmic rays from neutralino annihilation*, *Phys. Rev.* **D69** (2004) 063501, [astro-ph/0306207].

[148] T. Bringmann and M. Pospelov, *Novel direct detection constraints on light dark matter*, *Phys. Rev. Lett.* **122** (2019) 171801, [1810.10543].

[149] ATLAS collaboration, M. Aaboud et al., *Constraints on mediator-based dark matter and scalar dark energy models using $\sqrt{s} = 13$ TeV pp collision data collected by the ATLAS detector*, *JHEP* **05** (2019) 142, [1903.01400].

[150] F. Fortuna and P. Roig, *Impact of ATLAS constraints on effective dark matter-standard model interactions with spin-one mediators*, *Phys. Rev. D* **107** (2023) 075003, [2208.12330].

[151] ATLAS collaboration, G. Aad et al., *Search for new phenomena in events with an energetic jet and missing transverse momentum in pp collisions at $\sqrt{s}$ =13 TeV with the ATLAS detector*, *Phys. Rev. D* **103** (2021) 112006, [2102.10874].

[152] Particle Data Group collaboration, P. Zyla et al., *Review of Particle Physics*, *PTEP* **2020** (2020) 083C01.

[153] V. Gonzalez Macias and J. Wudka, *Effective theories for Dark Matter interactions and the neutrino portal paradigm*, *JHEP* **07** (2015) 161, [1506.03825].

[154] GAMBIT collaboration, P. Athron et al., *Thermal WIMPs and the scale of new physics: global fits of Dirac dark matter effective field theories*, *Eur. Phys. J. C* **81** (2021) 992, [2106.02056].

[155] LZ collaboration, J. Aalbers et al., *First Dark Matter Search Results from the LUX-ZEPLIN (LZ) Experiment*, 2207.03764.

[156] PandaX-4T collaboration, Y. Meng et al., *Dark Matter Search Results from the PandaX-4T Commissioning Run*, *Phys. Rev. Lett.* **127** (2021) 261802, [2107.13438].

[157] N. Zhou, D. Berge and D. Whiteson, *Mono-everything: combined limits on dark matter production at colliders from multiple final states*, *Phys. Rev. D* **87** (2013) 095013, [1302.3619].

[158] A. J. Brennan, M. F. McDonald, J. Gramling and T. D. Jacques, *Collide and Conquer: Constraints on Simplified Dark Matter Models using Mono-X Collider Searches*, *JHEP* **05** (2016) 112, [1603.01366].

[159] M. Bauer, M. Klassen and V. Tenorth, *Universal properties of pseudoscalar mediators in dark matter extensions of 2HDMs*, *JHEP* **07** (2018) 107, [1712.06597].

[160] A. Semenov, *LanHEP — A package for automatic generation of Feynman rules from the Lagrangian. Version 3.2*, *Comput. Phys. Commun.* **201** (2016) 167–170, [1412.5016].

[161] J. Alwall, R. Frederix, S. Frixione, V. Hirschi, F. Maltoni, O. Mattelaer et al., *The automated computation of tree-level and next-to-leading order differential cross sections, and their matching to parton shower simulations*, *JHEP* **07** (2014) 079, [1405.0301].

[162] C. Bierlich et al., *A comprehensive guide to the physics and usage of PYTHIA 8.3*, 2203.11601.

[163] J. Y. Araz, B. Fuks and G. Polykratis, *Simplified fast detector simulation in MADANALYSIS 5*, *Eur. Phys. J. C* **81** (2021) 329, [2006.09387].

[164] M. Cacciari, G. P. Salam and G. Soyez, *FastJet User Manual*, *Eur. Phys. J. C* **72** (2012) 1896, [1111.6097].

[165] S. Davidson, Y. Kuno, Y. Uesaka and M. Yamanaka, *Probing $\mu e\gamma\gamma$ contact interactions with $\mu \to e$ conversion*, *Phys. Rev. D* **102** (2020) 115043, [2007.09612].

[166] A. Gemintern, S. Bar-Shalom, G. Eilam and F. Krauss, *Lepton flavor violating decays L —> l gamma gamma as a new probe of supersymmetry with broken R parity*, *Phys. Rev. D* **67** (2003) 115012, [hep-ph/0302186].

[167] A. Cordero-Cid, G. Tavares-Velasco and J. J. Toscano, *Implications of a very light pseudoscalar boson on lepton flavor violation*, *Phys. Rev. D* **72** (2005) 117701, [hep-ph/0511331].

[168] J. I. Aranda, F. Ramirez-Zavaleta, J. J. Toscano and E. S. Tututi, *Higgs mediated lepton flavor violating tau decays tau —> mu gamma and tau —> mu gamma gamma in effective theories*, *Phys. Rev. D* **78** (2008) 017302, [0804.2652].

[169] J. I. Aranda, A. Flores-Tlalpa, F. Ramirez-Zavaleta, F. J. Tlachino, J. J. Toscano and E. S. Tututi, *Effective Lagrangian description of Higgs mediated flavor violating electromagnetic transitions: Implications on lepton flavor violation*, *Phys. Rev. D* **79** (2009) 093009, [0905.4767].

[170] D. Grosnick et al., *Search for the Rare Decay $\mu^+ \to e^+\gamma\gamma$*, *Phys. Rev. Lett.* **57** (1986) 3241.

[171] I. Angelozzi, *In pursuit of lepton flavour violation : A search for the $\tau \to \mu\gamma\gamma$ decay with ATLAS at $\sqrt{s}$ =8 TeV*, Ph.D. thesis, U. Amsterdam, IHEF, 2017.

[172] BaBar collaboration, B. Aubert et al., *Searches for Lepton Flavor Violation in the Decays $\tau^\pm \to e^\pm\gamma$ and $\tau^\pm \to \mu^\pm\gamma$*, *Phys. Rev. Lett.* **104** (2010) 021802, [0908.2381].

[173] MEG collaboration, A. Baldini et al., *Search for the lepton flavour violating decay $\mu^+ \to e^+\gamma$ with the full dataset of the MEG experiment*, *Eur. Phys. J. C* **76** (2016) 434, [1605.05081].

[174] Belle collaboration, A. Abdesselam et al., *Search for lepton-flavor-violating tau-lepton decays to $\ell\gamma$ at Belle*, *JHEP* **10** (2021) 19, [2103.12994].

[175] S. Banerjee et al., *Snowmass 2021 White Paper: Charged lepton flavor violation in the tau sector*, 2203.14919.

[176] F. Wilczek and A. Zee, *Rare Muon Decays, Natural Lepton Models, and Doubly Charged Leptons*, *Phys. Rev. Lett.* **38** (1977) 531.

[177] J. Hisano, S. Sugiyama, M. Yamanaka and M. J. S. Yang, *Reevaluation of Higgs-Mediated $\mu - e$ Transition in the MSSM*, *Phys. Lett. B* **694** (2011) 380–385, [1005.3648].

[178] SINDRUM collaboration, U. Bellgardt et al., *Search for the Decay $\mu^+ \to e^+e^+e^-$*, *Nucl. Phys. B* **299** (1988) 1–6.

[179] SINDRUM II collaboration, W. H. Bertl et al., *A Search for muon to electron conversion in muonic gold*, *Eur. Phys. J. C* **47** (2006) 337–346.

[180] HFLAV collaboration, Y. S. Amhis et al., *Averages of b-hadron, c-hadron, and τ-lepton properties as of 2018*, *Eur. Phys. J. C* **81** (2021) 226, [1909.12524].

[181] S. Gninenko, S. Kovalenko, S. Kuleshov, V. E. Lyubovitskij and A. S. Zhevlakov, *Deep inelastic $e - \tau$ and $\mu - \tau$ conversion in the NA64 experiment at the CERN SPS*, *Phys. Rev. D* **98** (2018) 015007, [1804.05550].

[182] F. Fortuna, A. Ibarra, X. Marcano, M. Marín and P. Roig, *Indirect upper limits on $\ell_i \to \ell_j\gamma\gamma$ from $\ell_i \to \ell_j\gamma$*, *Phys. Rev. D* **107** (2023) 015027, [2210.05703].

[183] F. Fortuna, X. Marcano, M. Marín and P. Roig, *Lepton Flavor Violation from diphoton effective interactions*, 2305.04974.

[184] T. Husek, K. Monsalvez-Pozo and J. Portoles, *Lepton-flavour violation in hadronic tau decays and $\mu - \tau$ conversion in nuclei*, *JHEP* **01** (2021) 059, [2009.10428].

[185] S. Gninenko, M. Kirsanov, N. Krasnikov and V. Matveev, *Probing lepton flavor violation in $\nu_\mu + N \to \tau + ...$ scattering and $\mu \to \tau$ conversion on nucleons*, *Mod. Phys. Lett. A* **17** (2002) 1407, [hep-ph/0106302].

[186] M. Sher and I. Turan, *$\mu + N \to \tau + N$ at a muon or neutrino factory*, *Phys. Rev. D* **69** (2004) 017302, [hep-ph/0309183].

[187] S. Kanemura, Y. Kuno, M. Kuze and T. Ota, *A Study of lepton flavor violating $\mu N(eN) \to \tau X$ reactions in supersymmetric models*, *Phys. Lett. B* **607** (2005) 165–171, [hep-ph/0410044].

[188] A. Abada, V. De Romeri, J. Orloff and A. Teixeira, *In-flight cLFV conversion: $e - \mu$, $e - \tau$ and $\mu - \tau$ in minimal extensions of the standard model with sterile fermions*, *Eur. Phys. J. C* **77** (2017) 304, [1612.05548].

[189] M. Takeuchi, Y. Uesaka and M. Yamanaka, *Higgs mediated CLFV processes $\mu N(eN) \to \tau X$ via gluon operators*, *Phys. Lett. B* **772** (2017) 279–282, [1705.01059].

[190] E. Ramirez and P. Roig, *Lepton flavor violation within the simplest little Higgs model*, *Phys. Rev. D* **106** (2022) 056018, [2205.10420].

[191] J.-P. Delahaye et al., *Enabling Intensity and Energy Frontier Science with a Muon Accelerator Facility in the U.S.: A White Paper Submitted to the 2013 U.S. Community Summer Study of the Division of Particles and Fields of the American Physical Society*, in *Community Summer Study 2013: Snowmass on the Mississippi*, 8, 2013, 1308.0494.

[192] EIC collaboration, A. Deshpande, *Physics of an Electron Ion Collider*, *Nucl. Phys. A* **904-905** (2013) 302c–309c.

[193] *The International Linear Collider Technical Design Report - Volume 2: Physics*, 1306.6352.

[194] Y. Acar, A. Akay, S. Beser, A. Canbay, H. Karadeniz, U. Kaya et al., *Future circular collider based lepton–hadron and photon–hadron colliders: Luminosity and physics*, *Nucl. Instrum. Meth. A* **871** (2017) 47–53, [1608.02190].

[195] D. A. Bryman, S. Ito and R. Shrock, *Upper limits on branching ratios of the lepton-flavor-violating decays $\tau \to \ell\gamma\gamma$ and $\tau \to \ell X$*, *Phys. Rev. D* **104** (2021) 075032, [2106.02451].

[196] D. K. Papoulias and T. S. Kosmas, *Nuclear aspects of neutral current non-standard ν-nucleus reactions and the role of the exotic $\mu^- \to e^-$ transitions experimental limits*, *Phys. Lett. B* **728** (2014) 482–488, [1312.2460].

[197] V. N. Gribov and L. N. Lipatov, *Deep inelastic e p scattering in perturbation theory*, *Sov. J. Nucl. Phys.* **15** (1972) 438–450.

[198] Y. L. Dokshitzer, *Calculation of the Structure Functions for Deep Inelastic Scattering and e+ e- Annihilation by Perturbation Theory in Quantum Chromodynamics.*, *Sov. Phys. JETP* **46** (1977) 641–653.

[199] G. Altarelli and G. Parisi, *Asymptotic Freedom in Parton Language*, *Nucl. Phys. B* **126** (1977) 298–318.

[200] K. Kovarik et al., *nCTEQ15 - Global analysis of nuclear parton distributions with uncertainties in the CTEQ framework*, *Phys. Rev. D* **93** (2016) 085037, [1509.00792].

[201] D. B. Clark, E. Godat and F. I. Olness, *ManeParse : A Mathematica reader for Parton Distribution Functions*, *Comput. Phys. Commun.* **216** (2017) 126–137, [1605.08012].

[202] H. H. Patel, *Package-X: A Mathematica package for the analytic calculation of one-loop integrals*, *Comput. Phys. Commun.* **197** (2015) 276–290, [1503.01469].

[203] A. Denner, S. Dittmaier and L. Hofer, *Collier: a fortran-based Complex One-Loop LIbrary in Extended Regularizations*, *Comput. Phys. Commun.* **212** (2017) 220–238, [1604.06792].

[204] T. Suzuki, D. F. Measday and J. P. Roalsvig, *Total Nuclear Capture Rates for Negative Muons*, *Phys. Rev. C* **35** (1987) 2212.

[205] R. Kitano, M. Koike and Y. Okada, *Detailed calculation of lepton flavor violating muon electron conversion rate for various nuclei*, *Phys. Rev. D* **66** (2002) 096002, [hep-ph/0203110].

[206] COMET collaboration, R. Abramishvili et al., *COMET Phase-I Technical Design Report*, *PTEP* **2020** (2020) 033C01, [1812.09018].

[207] Mu2e collaboration, L. Bartoszek et al., *Mu2e Technical Design Report*, 1501.05241.

[208] MEG II, MU3E collaboration, P. W. Cattaneo and A. Schöning, *MEG II and Mu3e status and plan*, *EPJ Web Conf.* **212** (2019) 01004.

[209] PRISM collaboration collaboration, Y. Kuno et al., "An Experimental Search for a $\mu^- - e^-$ Conversion at Sensitivity of the Order of 10^{-18} with a Highly Intense Muon Source: PRISM." 2006.

[210] COMET collaboration, M. Moritsu, *Search for Muon-to-Electron Conversion with the COMET Experiment †*, *Universe* **8** (2022) 196, [2203.06365].

[211] K. G. Chetyrkin, J. H. Kuhn and M. Steinhauser, *RunDec: A Mathematica package for running and decoupling of the strong coupling and quark masses*, *Comput. Phys. Commun.* **133** (2000) 43–65, [hep-ph/0004189].

[212] A. Ibarra, M. Marín and P. Roig, *Flavor violating muon decay into an electron and a light gauge boson*, *Phys. Lett. B* **827** (2022) 136933, [2110.03737].

[213] M. Marín, *Effective field theories in lepton flavor violating processes*, Ph.D. thesis, Cinvestav, 5, 2022.